C00-1248-55

MASTER

PROGRESS REPORT

ERDA CONTRACT EY-76-S-02-1248
"Electrical Charging of Small Particles at Low Pressures"

AERODYNAMIC
PARTICLE SIZE MEASUREMENT
BY
LASER-DOPPLER VELOCIMETRY

By
James Charles Wilson

Submitted by

Benjamin Y.H. Liu and K.T. Whitby

Particle Technology Laboratory
Mechanical Engineering Department
University of Minnesota
Minneapolis, Minnesota

to

Energy Research and Development Administration

April, 1978

Particle Technology Laboratory Publication Number 343

DISTRIBUTION OF THIS DOCUMENT IS UNLIMITED

DISCLAIMER

COO-1248-55

PROGRESS REPORT

ERDA CONTRACT EY-76-S-02-1248
"Electrical Charging of Small
Particles at Low Pressures"

AERODYNAMIC PARTICLE SIZE MEASUREMENT BY LASER-DOPPLER VELOCIMETRY

by

James Charles Wilson

Submitted by

Benjamin Y. H. Liu and K. T. Whitby

Particle Technology Laboratory
Mechanical Engineering Department
University of Minnesota
Minneapolis, Minnesota

to

Energy Research and Development Administration

April, 1978

Particle Technology Laboratory Publication Number 343

DISTRIBUTION OF THIS DOCUMENT IS UNLIMITED

EKB

AERODYNAMIC PARTICLE SIZE MEASUREMENT
BY LASER-DOPPLER VELOCIMETRY

A THESIS
SUBMITTED TO THE FACULTY OF THE GRADUATE SCHOOL
OF THE UNIVERSITY OF MINNESOTA

by

James Charles Wilson

IN PARTIAL FULFILLMENT OF THE REQUIREMENTS
FOR THE DEGREE OF
DOCTOR OF PHILOSOPHY

December, 1977

ABSTRACT

A method of measuring the aerodynamic diameter of aerosol particles was investigated. The method consists of accelerating particles in a converging nozzle and measuring their velocities near the exit of the nozzle with a laser-Doppler velocimeter. This study involved theoretical and experimental studies of particle velocity near the exit of converging nozzles. The results were applied to the problem of sizing atmospheric aerosols in the diameter range from .5 to 10 μm.

The experimental studies utilized a test nozzle with a converging angle of approximately 15° and an exit diameter of about .1 cm. Particles of known diameter in the range from 0.5 to 11.3 μm were accelerated under various flow conditions, and their velocities were measured approximately 145 μm downstream from the nozzle exit. The pressure drop across the nozzle was varied from 2.54 to 276 cm of H_2O, and particle velocity was observed to vary from approximately .5 times the gas velocity at the exit of the nozzle to 1 times this velocity.

A theoretical analysis utilized boundary layer theory to predict the velocity of the gas in the nozzle, and then the equations of particle motion were integrated to give the theoretical particle velocities. These values agreed with the experimental values to within a few percent. One-dimensional, ideal flow calculations successfully predicted the gas velocities along the center streamline of the nozzle, and since the particles were confined near to this streamline, this simplified flow model was used for the additional theoretical studies.

The effects of nozzle geometry, flow rate, particle density and particle size were studied using the results of calculations made with dimensionless equations. The velocity of a particle in a given nozzle and flow depends upon the aerodynamic diameter of the particle and the particle density. The geometry and flow can be chosen to minimize the effect of particle density. This was done in the case of a nozzle proposed for measurements of atmospheric aerosol. This nozzle converges with an angle of 45°, has an exit diameter of .1 cm and a proposed operating pressure drop of 54.6 cm of H_2O. Assuming that the density of particles in the atmosphere ranges from 1 g/cm^3 to 3 g/cm^3, the aerodynamic diameter of particles can be measured with an uncertainty of ±10% in the size range from .5 μm to 10 μm.

Acknowledgements

Dr. B. Y. H. Liu suggested the topic of this research and remained a source of excellent advice throughout the project. Dr. Liu is particularly gifted in the art of constructing learning situations which fit the needs of the individual student. I am grateful for the time I have spent working with and for him; it has been very rewarding.

Dr. S. V. Patankar and Mr. B. R. Baliga spent considerable time and effort explaining their computer program to me. Without their generous contribution, I could not have made use of the boundary layer approximation. All responsibility for misinterpretation, in this thesis, of the program or its results, rests with me.

The preparation of the early drafts was greatly aided by Ms. J. Boers and Mrs. M. P. Aanenson. The perseverance and competence of Ms. B. R. Wells-Howe were essential in the production of the final draft. The drafting skill of Mr. R. C. Moy is evident in the drawings and is greatly appreciated.

The help of friends and colleagues is doubly appreciated: once, for the material aid, and again, because it represents friendship. The people in the Particle Technology Laboratory are thanked for creating a stimulating and supportive atmosphere in which to work. Special thanks go to Dr. D. Y. H. Pui and Mr. A. Kapadia for their help with numerous details.

Thermo-Systems, Inc., St. Paul, Minn., made the laser-Doppler velocimeter available to me for a period of two years. Their essential contribution is gratefully acknowledged.

This thesis was supported financially by the U. S. Energy Research and Development Administration under Contract No. EY-76-S-1248.

TABLE OF CONTENTS

LIST OF TABLE CAPTIONS

No. Title Page

LIST OF FIGURE CAPTIONS

NOMENCLATURE

A_E	exit area, cm^2
A_I	inlet area, cm^2
C_n	channel number
C	slip correction
C_D	drag coefficient
D_p	particle diameter, cm or μm
F	force, dyne
F_D	drag force, dyne
N	particle concentration, cm^{-3}
N_i	number of counts in i^{th} channel
P	pressure, $dyne/cm^2$, cm of H_2O, cm of Hg
P^*	dimensionless pressure
Q	volumetric flow, ml/s, lpm
R	radius, cm
R_i	radius at a point i, cm
Re	Reynolds number based on D_p
Re_f	flow Reynolds number
Re_p	particle Reynolds number
St	Stokes number
S_p	probability of finding p
U_e	centerline gas velocity at the nozzle exit, cm/s, m/s
U_g	centerline gas velocity, cm/s, m/s
U_g^*	dimensionless centerline gas velocity
U_p	particle velocity, cm/s, m/s

$\overline{U}_p$	geometric mean particle velocity, cm/s, m/s
U_p^*	dimensionless particle velocity
V	measuring volume, cm^3
V_c	voltage, volts
a	radius of the nozzle at the exit, cm
a	mass flux term (Appendix A)
b	mass flux term (Appendix A)
a_i, b_i, c_i, d_i, and e_i	coefficients
c	volumetric concentration
d	source term (Appendix A)
d_f	fringe spacing, μm or cm
e	transport coefficient term (Appendix A)
f_c	calibrating frequency, Hz
f_D	Doppler frequency, Hz
f_g	frequency of vibration, Hz
$\overline{f}_g$	geometric mean of Doppler frequencies, Hz
n	integer exponent, frequency range on counter
r	radial coordinate, cm
r_i	radius of i^{th} node, cm
u	axial velocity, cm/s
u_i	axial velocity at i^{th} node, cm/s
u^*	dimensionless axial velocity
v	radial velocity
x	axial coordinate, cm

x^*	dimensionless axial coordinate
x_i	indexed axial coordinate, cm
Φ	variable in conservation equation (Appendix A)
Ψ	stream function
Ψ_E	stream function at exterior boundary
Ψ_I	stream function at interior boundary
α	half-angle of conical nozzle, deg
λ	wavelength, cm, nm
μ	viscosity of fluid, poise
ρ	density
ρ'	particle density
σ	standard deviation
σ_g	geometric standard deviation
σ_m	standard deviation of the mean
$(\sigma_{rs})_a$	actual relative standard deviation of size distribution
$(\sigma_{rs})_m$	indicated relative standard deviation of size distribution
σ_{rv}	relative standard deviation of a velocity distribution
ϕ	angle between the laser beams, deg
ω	dimensionless stream function
ω_i	value of ω at i^{th} node

CHAPTER 1

INTRODUCTION

1.1 Introduction

Concern has grown in recent years over the effects of particles suspended in air. Questions have arisen concerning the role of fine particles in causing or contributing to respiratory ailments, degrading visibility in the atmosphere, or altering the climate. These have prompted considerable research into the characterization and measurement of aerosols. Since the particle diameters of interest in these studies range from a few thousandths of a micron to tens of microns, many different instruments operating on different principles have been developed to size and characterize aerosols. Instruments which classify particles according to aerodynamic diameter are of particular interest in the study of health effects, since the aerodynamic diameter is the primary characteristic of a particle which determines if and where it settles or impacts in the respiratory system. The present study concerns the development of an instrument to make rapid, in situ measurements of aerodynamic size in the range from .5 μm to 10 μm.

1.2 Object of the Study

The principal aim of this work is to study a method for measuring the aerodynamic diameter of particles in the diameter range from .5 μm to 10 μm. The method involves passing particles through a converging nozzle and measuring their velocity with a laser-Doppler velocimeter (LDV) as they exit the nozzle.

The particles lag behind the rapidly accelerated flow, and the amount of this lag depends upon their size, density and the flow conditions in the nozzle.

In order to use particle velocity as a measure of particle size, it is necessary to know how this velocity is affected by nozzle geometry, the flow in the nozzle, particle diameter, and particle density. These questions are pursued here in experimental and theoretical studies. These studies cover a broad range of operating conditions and are intended to be sufficiently general so that they can be used for actual instrument design or for assessing the feasibility of the technique for various applications.

The results are applied to the problem of sizing atmospheric aerosols in order to demonstrate that an appropriate nozzle and flow can be chosen for the rapid, in situ measurement of aerodynamic size distributions.

Thus, the objectives are to study the method, to explore one of its possible applications, and to present sufficient information so that it is accessible to others.

The remainder of this chapter contains the definition of aerodynamic diameter and a discussion of its importance, a brief review of optical methods widely used to size particles in the .5 μm to 10 μm size range, and a review of other velocimetric methods used in the measurement of particle size in the diameter range of interest. The final section introduces and outlines the present study.

1.3 Aerodynamic Diameter

The aerodynamic diameter, D_a, combines factors of shape, size and density into one parameter and provides a convenient means of characterizing a particle when its motion in a flow is the principal consideration. Knowing the aerodynamic diameter of a particle is sufficient to allow prediction of its motion in a known flow if the particle Reynolds number is small and the only forces acting on the particle are drag forces and body forces proportional to particle mass. Thus, impactors (Marple and Liu, 1974), centripteres (Stöber, 1976), and acoustic fields (Kirsch and Mazumder, 1975) have been used to classify particles according to D_a. At small particle Reynolds numbers, deposition by impaction and settling is determined by aerodynamic diameter, and therefore, the Task Group on Lung Dynamics of the International Commission on Radiological Protection (1966) suggested that the particles used in aerosol inhalation studies be characterized in terms of the "diameter of a unity density sphere with the same settling velocity as the particle in question." This definition is consistent with that of D_a given in Equation (1.2) below.

The generality of D_a can be understood by considering Equation (1.1), which describes the motion of a particle moving at small Reynolds numbers (Fuchs, 1964, p. 27 and 107):

$$\frac{\pi}{6} D_p^3 \rho' \frac{d\vec{U}_p}{dt} = \frac{3\pi\mu D_p}{C} (\vec{U}_g - \vec{U}_p) + \vec{F} \qquad (1.1)$$

where D_p is the particle diameter; ρ' is the particle density and C is the slip correction [see Equation (3.16)]; μ is the gas viscosity; $\vec{U}_g$ is the gas velocity; $\vec{U}_p$ is the particle velocity and $\vec{F}$ is any body force acting on the particle. In the case of an irregular particle, D_p is replaced by the diameter of a sphere having the same mass and density as the particle, and the first term on the right-hand side of the equation, the Stokes drag term, is divided by the dynamic shape factor (Fuchs, p. 37 ff.). This modification accounts for the dependence of drag on orientation and shape while reflecting the fact that the drag on a non-spherical particle is still proportional to $(\vec{U}_g - \vec{U}_p)$ at small particle Reynolds numbers.

In the cases mentioned above, F is either zero (for example, in impaction) or proportional to particle mass (for example, in settling or circular motion). Thus, all the terms involving ρ', C and D_p can be grouped into a single term, $CD_p^2\rho'$, and particles having the same value of $CD_p^2\rho'$ will have the same trajectories. This suggests a definition of aerodynamic diameter (Raabe, 1976):

$$\sqrt{C(D_a)}\, D_a = D_p \sqrt{\rho' C(D_p)} \tag{1.2}$$

where D_a is the aerodynamic diameter of a particle having a diameter D_p. $C(D_a)$ and $C(D_p)$ are the slip corrections applying to D_a and D_p. Irregular particles are again treated by the introduction of the diameter of the mass-equivalent sphere, and by dividing that diameter by the square root of the dynamic shape factor. Thus, Equation (1.1) predicts the same motion for all particles having the same value of D_a as long as $\vec{F}$ is zero or proportional to mass.

At larger Reynolds numbers, another term is added to Equation (1.1). In such cases, aerodynamic diameter is no longer sufficient to characterize the particle. This is discussed in Chapter 4. D_a does not provide sufficient information to permit calculation of particle mass or shape. It says nothing about chemical composition, optical properties, or any of the dozens of other things researchers want to know from time to time about aerosol particles.

1.4 Optical Particle Counters

Optical particle counters (OPCs) are very frequently used to size aerosols in the diameter range from .5 μm to 10 μm and beyond. They will be discussed briefly to indicate what they measure and how it relates to the concerns of the present study. These instruments come in a variety of configurations. Most operate by measuring a portion of the light scattered by individual particles as they pass through a light beam. While it is generally true that large particles scatter more light and small ones scatter less, it must be remembered that scattered light is the detected variable. And so, the optical properties of the particles influence the output of the OPC. When measuring spheres of known refractive index, the output of an OPC can be related with considerable accuracy and resolution to the diameter of the sphere. When measuring spheres of unknown refractive index, the output of the OPC is given in terms of equivalent light-scattering diameter. If the range of the refractive index present in the aerosol is known, the equivalent light-scattering diameter can be related to particle diameter with an uncertainty depending on this range. Irregular shape further complicates the problem and reduces the resolution and accuracy of the measurements. In the best situation, an OPC gives the geometrical size or projected area of the particle.

Gebhart et al. (1976) reviewed laser and white light-scattering instruments. They note that lasers are particularly useful for particle sizes below the wavelength of light where the scattered intensity of monochromatic radiation is a monotonic function of particle size. Particles larger than the wavelength of light produce intensities which oscillate with particle size. The oscillations can be smoothed over by using white light for these larger particle sizes. They report an instrument using white light and collecting forward-scattered light from 2.5° to 5.5°. This instrument is quite insensitive to refractive index and shape, and has an output relating principally to the projected area of the particle.

Willeke and Liu (1976) and Whitby and Willeke (1976) reviewed commercially available OPCs using white light to size particles in the range of interest in this study. While such instruments provide valuable information, the uncertainties due to unknown refractive index and shape can be significant. As in the case reported by Gebhart, these problems vary in importance with the optical configuration. Whitby remarks that the uncertainties involved in sizing atmospheric aerosols with OPCs can be reduced to an acceptable level by careful choice of instruments and modifications such as sheath air. Questions of viewing volume size and sample rate take precedence over considerations of the effects of refractive index when sizing atmospheric aerosols which, at the lower end of the OPC range, are predominately spherical, wet particles.

Knollenberg and Luehr (1976) report an instrument in which particles pass through a laser cavity and interact with the resonating radiation. Scattered radiation is measured from particles ranging in size from .05 μm to about 10 μm. Calibration curves show that uncertainties due to refractive index and oscillating intensity with D_p are of the order of uncertainties encountered in white light OPCs.

For studies of optical properties of aerosols, OPCs are certainly the instrument of choice. However, for sizing respirable coal dust, for example, they have serious shortcomings. To overcome these problems, Marple and Rubow (1976) have calibrated OPCs with impactor-classified coal dust to allow use of the OPC to gain aerodynamic size information. Liu et al. (1974) preclassified coal aerosol up to 2.4 μm in size using an electrical mobility analyzer, and then fed the dust to two OPCs. Since single-charged particles dominated, these particles were monodisperse in Stokes-drag diameter. However, the OPC indicated distributions with geometric standard deviations of 1.6 to 2.0. And so, at least it must be said that the resolution of an OPC calibrated by pre-classified irregular dust is not very good.

1.5 Previous Work

This discussion is limited to methods in which size is determined by velocity measurements.

Yanta (1973) has reported results of LDV measurements of the velocity of particles on the centerline of a supersonic nozzle and downstream of a normal shock. The first flow is rapidly accelerating and the second, rapidly deaccelerating. In both cases, particle velocity differs from the gas velocity by an amount depending on particle diameter and density. Yanta presents the results of calculations of velocity lag for spheres in a Mach 3 nozzle and behind a normal shock. The calculations show that particle velocity depends on D_p and the position of measurement. The density of the particles is not given. He then shows particle velocity histograms measured for atmospheric aerosols and an oil droplet aerosol at various positions downstream of the shock and at the point of maximum resolution in the Mach 3 nozzle. These velocity distributions are converted to size distributions using the theoretical curves. The size distribution for the oil aerosol agrees reasonably well with one obtained using an optical particle counter. This method was intended for the measurement of particle size by researchers using the LDV to study supersonic flows. The problem faced by these researchers is to quantify the velocity lag of the particles so that they can determine the actual fluid velocity.

A device described by Dahneke (1972, 1973, 1974) also utilizes a jet to accelerate particles. However, in this case, the jet expands into a vacuum where the particles are separated from the gaseous component of the aerosol (Figure 1.1). Dahneke calls the result an aerosol beam which, similar to a molecular beam, can be treated in various ways. The initial step of the process is to confine the aerosol to the center streamline of the flow into a converging nozzle by the use of clean sheath air. This focusing of the aerosol minimizes the spreading of aerosol beam as it expands into the vacuum on the downstream size of the nozzle. The gas is pumped away, but the particles, due to their large mass, continue on a straight path in the vacuum chamber. At this point, the velocity of the particles can be measured using, for example, a two-beam, time-of-flight measurement. Dahneke shows the results of measurements on PSL aerosols. The theoretical analysis of this method is presented by Schwartz and Andres (1976), in which terminal velocity is shown to depend on the product of particle density and diameter for a given nozzle. The method has been demonstrated for particles from .3 μm to several tens of μm in diameter.

Dahneke also proposed deflecting the aerosol beam with a perpendicular jet of air. Large particles would be deflected less and small ones, more. The deflected particles could be collected or counted at different positions, each position corresponding to a different size.

Chabay and Bright (1977) describe a chamber in which particles settle and their settling velocity is measuring using laser-Doppler velocimetry. In this case, the reference beam

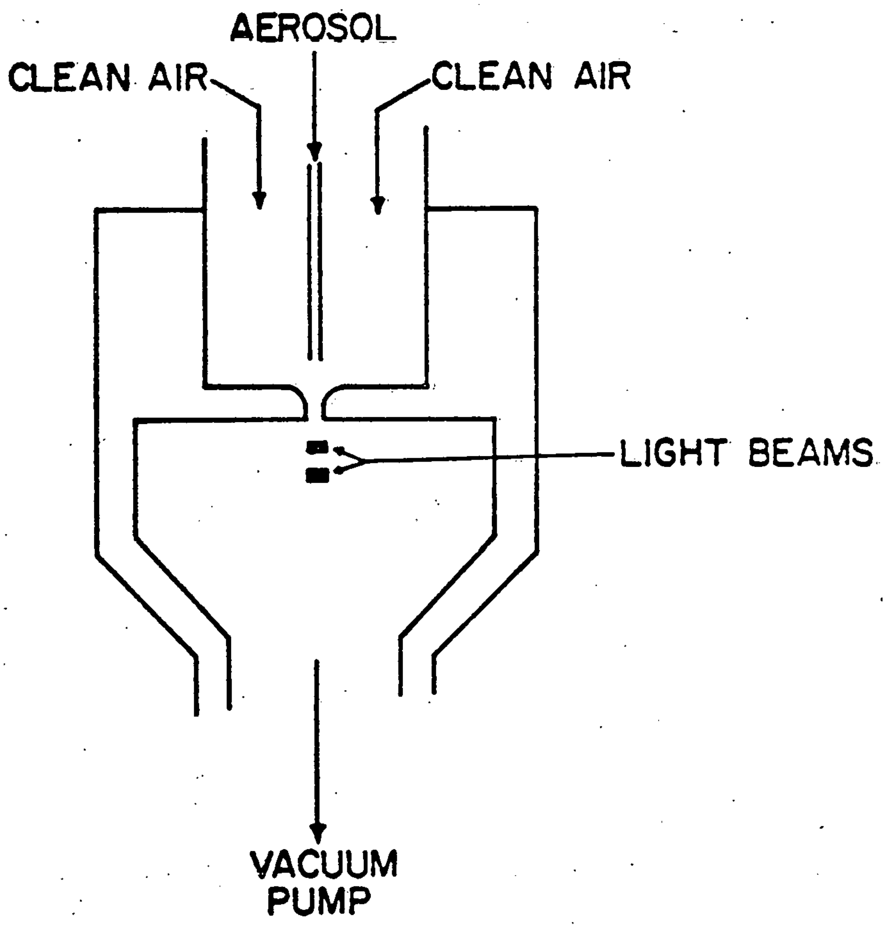

Figure 1.1 Aerosol beam apparatus reported by Dahneke (1974).

configuration is used, and the light scattered from several particles is simultaneously measured. The resulting signal is analyzed for beat frequency and amplitude. The analysis assumes that the aerosol is made up of spherical particles all of the same density and refractive index, and that both are known. Each Fourier component of the signal corresponds to a particular particle size. Knowing the refractive index allows computation of the amount of light arriving at the detector from one particle of a given size. Dividing this number into the amplitude of the corresponding Fourier component produces the number of particles contributing to that Fourier component. So the signal from the photodetector is Fourier-transformed, and the frequency spectrum is scaled by the relative Mie scattering amplitudes point-by-point. The result is a size distribution. This method was applied to the study of water droplet growth where the assumptions of homogeneity of shape, density and refractive index are valid (Gollub et al., 1974). The method has also been used to analyze test aerosols in the .5 μm to 50 μm range.

A method for obtaining aerodynamic size is reported by Kirsch and Mazumder (1975). In this method, particles are set into motion in an acoustic field, and their velocity is measured using a frequency-biased differential LDV. For this measurement, it is necessary to measure velocities near zero and to distinguish the direction of the motion. This is accomplished by shifting the frequency of the laser beams relative to each other so that a stationary particle scatters light with non-zero beat frequency.

In the present case, the beam is passed through a rotating diffraction grating, with the result that the two beams in the dual-beam method differ in frequency by 2.5 MHz. Thus, the zero velocity point corresponds to 2.5 MHz; negative velocities have lower frequencies and positive velocities have higher frequencies. The amplitude of the sinusoidal particle velocity divided by the amplitude of the gas velocity is shown to depend on aerodynamic diameter, and the system has been used to measure size distributions in the .1 μm to 10 μm diameter range.

Agarwal (1975) performed studies on micron-sized particles emerging from a thin-walled orifice. Using an LDV, he found the velocity of the particles to depend on particle size. The orifice was operated at sonic conditions, and tests were run for particle diameters ranging from nearly 3 μm to 9 μm.

1.6 Present Study

In the present study, the velocity of particles emerging from a converging nozzle was studied experimentally and theoretically. The experimental studies involved measuring the velocity of spherical particles of known diameter and density as they emerged from a test nozzle. Particles ranging in diameter from .5 μm to 11.3 μm were measured in various flows. The pressure drop across the nozzle was varied from 2.54 cm of H_2O to 691 cm of H_2O. The measurements were made with an LDV. The results of these measurements are presented in Chapter 2.

The theoretical study began with an analysis of the experimental results. First, the shape of the test nozzle was determined. The flow in the nozzle was then calculated using boundary layer theory for several values of pressure drop across the nozzle observed in the experiment. The flow was also calculated using one-dimensional ideal flow, and these predictions of centerline gas velocity agreed well with those of the boundary layer theory. Then, particle velocities for particles moving in the flows were calculated from the equations of particle motion. The agreement between theory and experiment, presented in Chapter 3, justifies the use of the theory in other circumstances.

The second part of the theoretical study involved applying the theory, validated in Chapter 3, to nozzles of different geometry and particles of different properties. Dimensional analysis shows that the dimensionless particle velocity depends upon nozzle shape, dimensionless distance from the nozzle exit, Stokes number, and a particle Reynolds number. Thus, calculations were made for three nozzle shapes, four dimensionless distances from the nozzle exit, and a range of Stokes and Reynolds numbers based on particle diameter. The aerodynamic diameter can be determined from Stokes number. So, if the dependence of dimensionless velocity on the Reynolds number can be minimized, then aerodynamic diameter can be determined from the velocity. The discussion of this task and the results of the calculations are presented in Chapter 4. The results should be general enough to permit nozzles to be designed and flow rates chosen for a wide variety of applications.

One possible application of this system is discussed in Chapter 5. There, the choice of nozzle and flow parameters to be used in measuring aerodynamic size distributions in atmospheric aerosols is explored.

Conclusions concerning this work are presented in Chapter 6.

CHAPTER 2

EXPERIMENTAL

2.1 Introduction

The first objective of the experimental investigation was to determine the effect of particle size on the velocity of particles as they emerge from a test nozzle in a variety of flow conditions. The second objective was to make the measurements with sufficient precision and resolution to demonstrate the feasibility of determining particle size from particle velocity. These velocity measurements were made with a laser-Doppler velocimeter (LDV).

It is shown in subsequent chapters that it is possible, within certain limits, to determine the aerodynamic diameter of a particle by measuring its velocity as it emerges from a nozzle. This conclusion results from a theoretical extension of the experimental results presented in this chapter. Thus, the experimental investigations provide insight into the functioning of the system and the data base for validating the theory, which in turn allows a more general treatment of the problem.

The objectives required standard aerosols and careful control of the flow system. In addition, they required that the LDV be aligned and positioned correctly, and that it be accurate. The subsequent theoretical analysis demanded that the flows be characterized in such a way as to allow the determination of the velocity field in the nozzle. And finally, it was necessary to know the distance from the nozzle exit to the point where the velocity measurement is made.

In this chapter, the procedure used to complete each of these tasks is discussed and the results of the experimental investigations are reported. First, however, the system as a whole will be briefly described so that the relationship between the various parts may be understood. Figure 2.1 is a schematic of the experimental apparatus.

A monodisperse aerosol of known size was generated and fed to the flow system. The flow system provided clean sheath air around the aerosol flow. The flows were adjusted so that sheath air accounted for 90% of the total flow, and thus the aerosol stream was focused and remained confined near the center streamline as it passed through the nozzle. The flow profile was sufficiently flat in the center portion of the flow so that all particles experienced essentially the same flow conditions and emerged with essentially the same velocity. The flow meters used to monitor the flows are shown on Figure 2.1. The flow system also allowed careful control of the pressures upstream and downstream of the nozzle, so that the flow conditions were known and reproducible.

The velocities of the particles emerging from the nozzle were measured at a known point using an LDV. The laser, beam splitter, lenses and photomultiplier (PM) are shown. The frequency output by the PM when a single particle passes through the crossed laser beams is proportional to the particle velocity. This velocity is counted in a signal processor, and the results are analyzed and stored in an MCA.

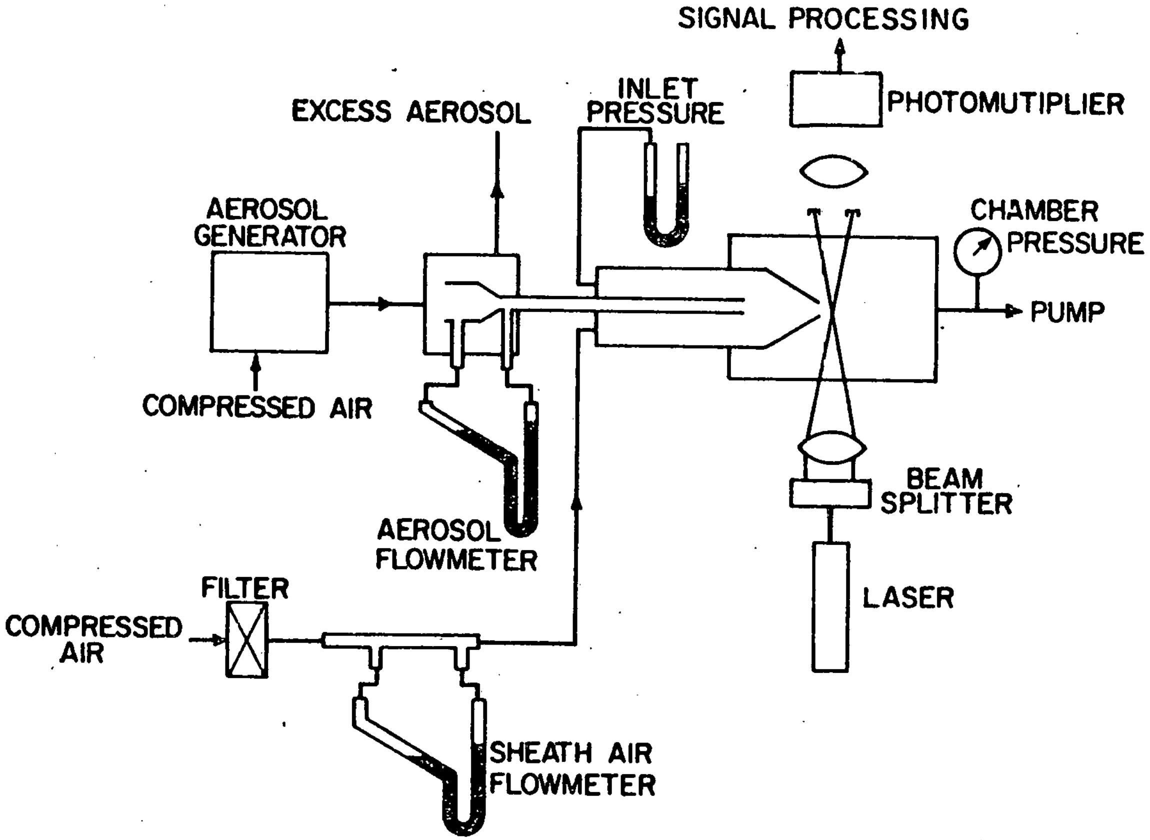

Figure 2.1 Schematic of experimental apparatus.

2.2 Generation of the Test Aerosol

Droplets of oleic acid and polystyrene latex (PSL) spheres were used as the test aerosols. The oleic acid particles were generated using a vibrating orifice aerosol generator (VOAG). This method has been reported in the literature (Berglund and Liu, 1973), and is based on the fact that a liquid jet can be broken into a stream of uniform droplets when disturbed with a periodic vibration. In the present case, a filtered solution of oleic acid dissolved in isopropyl alcohol is pumped by a syringe pump through an orifice approximately 10 μm in diameter. A piezoelectric crystal driven by an oscillator provides the mechanical excitation to break the liquid jet up into a stream of droplets. A turbulent jet of dispersion air is provided around the stream of droplets to insure that they do not coalesce at a high rate. This dispersed aerosol stream then merges with a flow of dilution air, which then passes through a Kr-85 neutralizer to neutralize the electrical charge which was generated as the liquid stream passed through the orifice. The aerosol is then transported to a small chamber from which samples are drawn into the nozzle. During the transport of the aerosol, the alcohol evaporates, leaving the oleic acid to form spherical particles. A diagram of the VOAG apparatus is given in Figure 2.2 (Liu, 1976).

The diameter D_p of the particles produced by the VOAG is given by:

$$D_p = \left(\frac{6Qc}{\pi f_g}\right)^{1/3} \qquad (2.1)$$

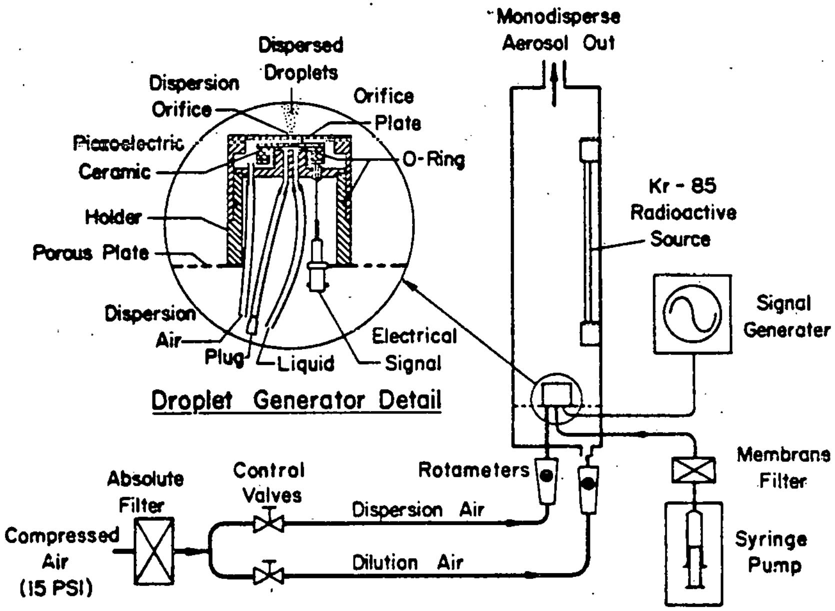

Figure 2.2 Schematic of VOAG apparatus.

where Q is the volumetric flow of solution through the orifice and f_g is the frequency of vibration. The volumetric concentration of the oleic acid in the solution is given by c. Under conditions of proper operation, a certain fraction of the droplets will collide with each other to form doublets. The resulting particles have twice the volume of the primary particles and are also quite useful since there is usually no difficulty in distinguishing between the doublets and primary particles. Berglund and Liu report that the accuracy of Equation (2.1) in predicting particle diameter is 2% or better in routine operations. They also report the average geometric standard deviation of DOP aerosols generated by the VOAG to be 1.014 as determined by the electrical mobility method.

In the present study, $Q = 1.50 \times 10^{-3}$ ml/s and $f_g = 200$ KHz were used. The dispersion air was set to around 1 lpm and the dilution air was set to about 15 lpm. Table 2.1 shows the values of c and the corresponding primary and doublet particle diameters. The density of the oleic acid used in this experiment was measured by Westphal balance and found to be .886 g/cm^3.

Table 2.1 Volumetric concentration of oleic acid and resulting particle diameters

c	Primary D_p, μm	Doublet D_p, μm
.00507	9.0	11.3
.00156	6.1	7.7
.00195	3.04	3.8

Uniform polystyrene latex spheres in suspension were purchased from Dow Chemical Co. (P. O. Box 68511, Indianapolis, IN 46268). The suspension was diluted in distilled water and placed in an ultrasonic bath to insure good dispersion. The PSL aerosol was generated by nebulizing the suspension in a RETEC X-70/N nebulizer (Retec Development Lab, 9730 S.W. Scholls Ferry Road, Portland, OR 97223). The resulting aerosol was mixed with dry, filtered air and passed through a diffusion drier. The dried PSL particles were then transported to a small tank from which aerosol was drawn into the nozzle.

The diffusion drier consists of coaxial cylinders, the outer one of plastic and the inner one of wire mesh. The space between the cylinders is filled with silica gel, and the aerosol passes down the axis of the inner cylinder which offers no obstruction to the flow. The moisture diffuses to the silica gel. The overall length of the drier is about 30 cm with the outer cylinder being nearly 6 cm in diameter and the inner one, 1.5 cm in diameter.

The nebulizer flow was set at about 2 lpm, and the drying air, at about 15 lpm. Table 2.2 gives the particle size and standard deviation reported by Dow and lot numbers of the suspensions used. The density of PSL is 1.05 g/cm^3.

In order to insure that the initial dilution was adequate, the diluted suspension was rediluted by 10 parts water to 1 part suspension. The velocity of the resulting aerosol particles emerging from the nozzle was compared to the velocity of

Table 2.2 PSL particle diameters and standard deviations

D_p, μm	Standard Deviation, μm	Lot Number
.500	.0027	2F7X
.794	.00400	3E6B
1.101	.0055	2G3P
2.02	.0135	4K2J

the particles resulting from the initial dilution. These two velocities were found to be the same, which indicates that single PSL particles were aerosolized using both dilutions. Had the first dilution produced groups of PSL particles, then the increased dilution would have produced smaller groups of PSL particles with different velocity characteristics.

2.3 The Flow System

The flow system provided a reproducible flow by allowing careful control of the pressure at the inlet to the nozzle and in the test chamber. It also provided adequate flow to transport aerosol to the nozzle and a means to restrict the aerosol to the center 10% of the nozzle flow. Two flow systems were used, one for flows for which the pressure drop across the nozzle exceeded 5 cm of Hg, and the other for flows having smaller values of pressure drop.

The nozzle and chamber were common to the two systems and will be discussed first. Figure 2.3 shows a cross-section from the front of the nozzle and chamber and a cross-section from the size of the chamber. "O"-rings provided a seal around the windows and nozzle. For most measurements, a tube was connected from

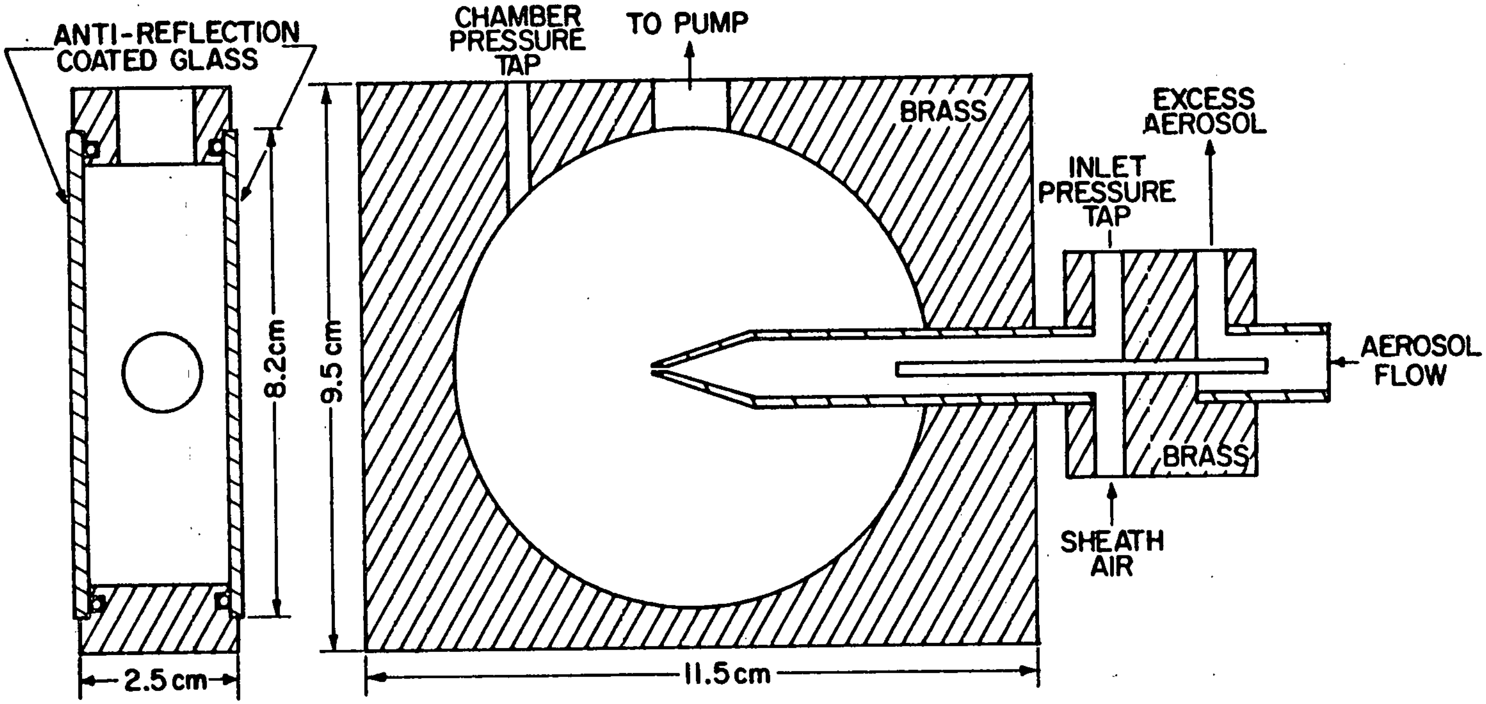

Figure 2.3 Diagram of test nozzle and chamber.

the outlet of the chamber to an aerosol trap positioned opposite the nozzle. The presence of the trap did not affect the measured particle velocities, but reduced the amount of aerosol circulating in the chamber and helped keep the windows clean. Thus, the aerosol trap reduced the noise generated by the LDV.

The inlet pressure tap was connected to a differential manometer which was open on the other side to the atmosphere. The chamber pressure and atmospheric pressure were measured with absolute pressure gauges having a resolution of .13 cm of Hg (Model FAXA 129113, Wallace and Tiernan, 25 Main St., Belleville, NJ 07109). In the cases of small flows, the pressure drop across the nozzle was measured directly with a manometer. The total flow through the nozzle was controlled by setting the inlet pressure and the chamber pressure or the inlet pressure and the pressure drop across the nozzle. The division of the flow between aerosol flow and sheath air flow is described below. The excess aerosol flow was monitored with a rotameter, and it was thus possible to provide near-isokinetic conditions at the inlet to the nozzle when necessary. The pressure in the inlet pressure tap was 76.2 cm of Hg (1036 cm H_2O) for all trials, and the aerosol flow was set to approximately 10% of the total flow through the nozzle. All volumetric flows are calculated and presented for a pressure of 76.2 cm of Hg.

The shape of the nozzle is treated in detail in Chapter 3. Briefly, it can be described as a conical nozzle with a short throat near the exit. The nozzle converges with a conical half-angle of approximately 15°. The radius at the exit is about .05 cm, and the throat section is approximately .1 cm in length. The radius of the entrance to the nozzle is about .5 cm, and the overall length is 1.77 cm.

Figure 2.4 is a photograph of the chamber and nozzle, showing the nozzle painted black to minimize stray reflected light. Positioning screws allow movement of the chamber parallel and perpendicular to the axis of the nozzle. Leveling screws allow control of the inclination of the nozzle axis with respect to the plane of the laser beams.

2.3.1 Flow System for Large Values of Pressure Drop

Figure 2.5 is a diagram of the flow system utilized for flows having pressure differences across the nozzle greater than 5 cm of Hg. The sheath air flow was measured by a glass capillary tube flow meter approximately 20 cm in length and .3 cm in diameter. The aerosol flow nozzle was made from a #15 hypodermic syringe needle. The radius of the flow nozzle is about .4 cm at the upstream pressure tap and .14 cm at the downstream tap. Both flow meters were calibrated at pressures near those encountered in normal operation.

In order to establish the desired flow conditions, valve A was set to give the proper chamber pressure, valve B was set to give the proper aerosol flow, valve D was set to give the proper inlet pressure, and valve C was set to give nearly isokinetic sampling conditions at the inlet of the aerosol flow nozzle. The last adjustment was unnecessary for smaller particles.

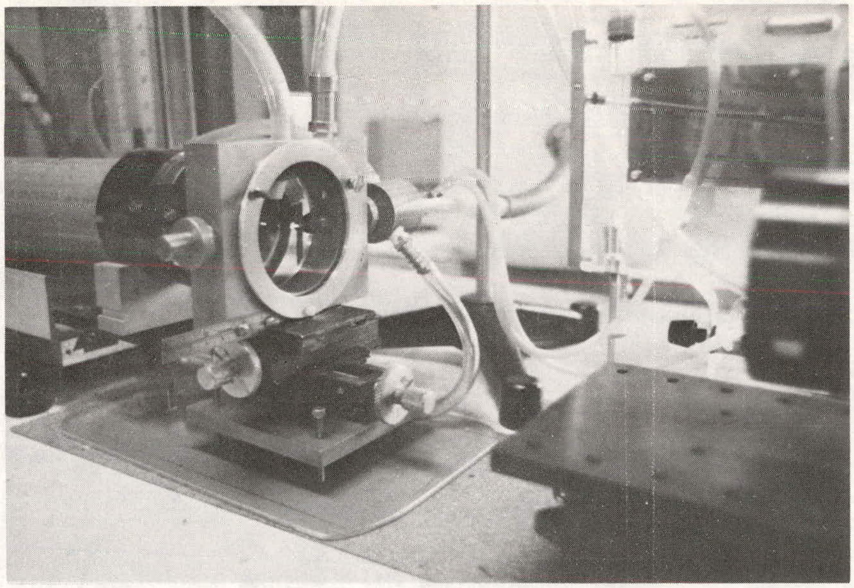

Figure 2.4 Photograph of nozzle in the chamber.

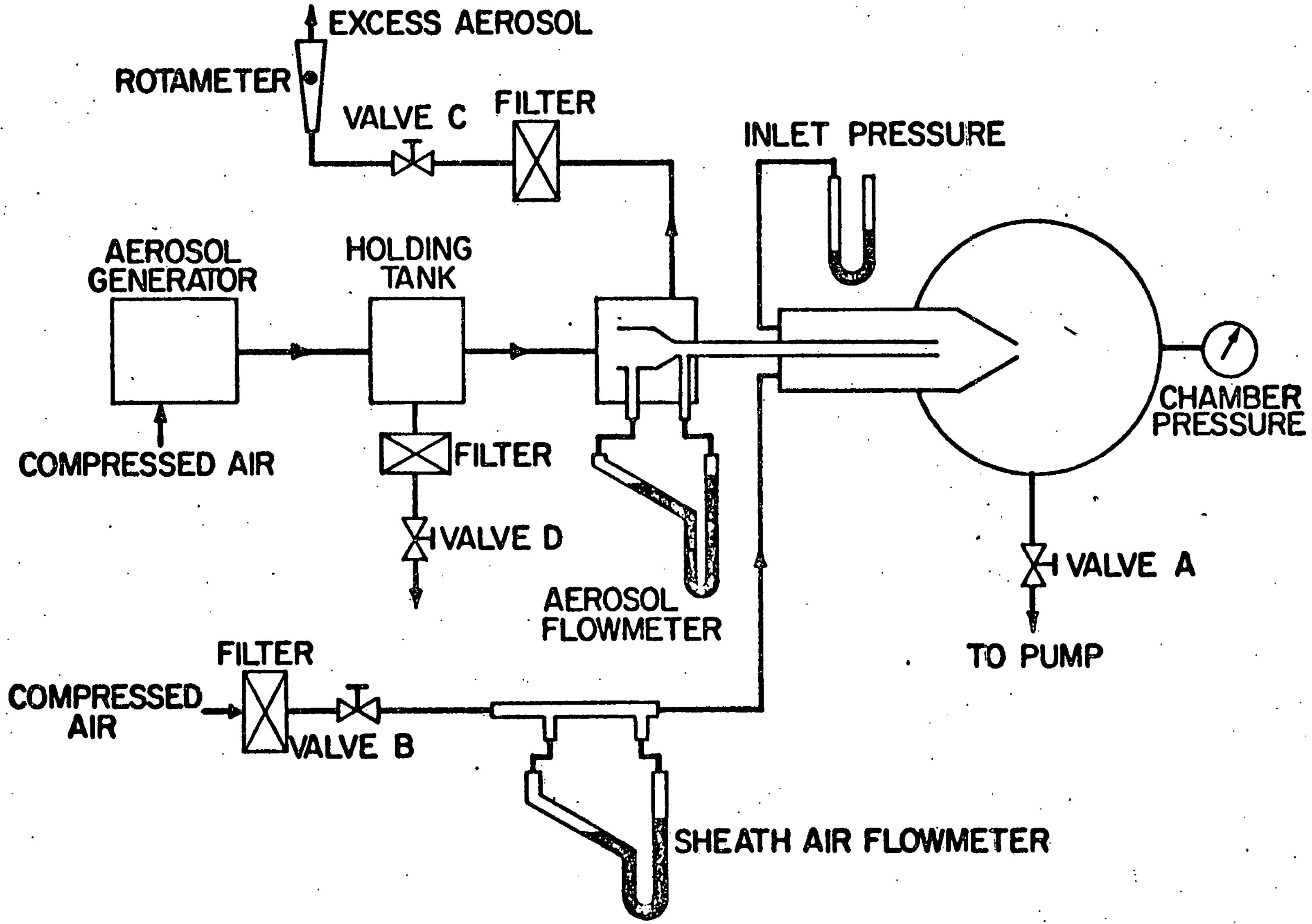

Figure 2.5 Flow system for large values of pressure drop.

Since the values are interdependent, it was necessary to repeat the sequence a few times to obtain the desired conditions. Occasionally the aerosol generator flows were adjusted to help obtain the appropriate value of inlet pressure when atmospheric pressure was low, or to provide adequate transport flow.

The flow conditions used in the experiment are summarized below.

Table 2.3 Flow conditions for large pressure drop flows

Pressure Across the Nozzle cm of H_2O	Chamber Pressure cm of H_2O	Aerosol Flow lpm	Sheath Flow lpm	Total Flow lpm
691	345	.98	9.8	10.8
484	552	.98	9.7	10.7
276	760	.90	8.8	9.7
69.1	967	.54	4.6	5.2

2.3.2 Flow System for Small Values of Pressure Drop

Figure 2.6 shows the arrangement for smaller flows. In this case, the pressure drop across the nozzle is measured directly. The aerosol flows were so small that the pressure drop across the aerosol flow meter was insufficient to provide a useful indicator. Therefore, the sheath air, measured by a capillary tube flow meter of smaller diameter, was used to set the proper balance between aerosol and sheath air flow. This capillary tube flow meter consists of a tube .139 cm in diameter and about 20.7 cm in length. The upstream pressure tap is placed approximately 8 cm from the entrance, leaving the distance between pressure taps

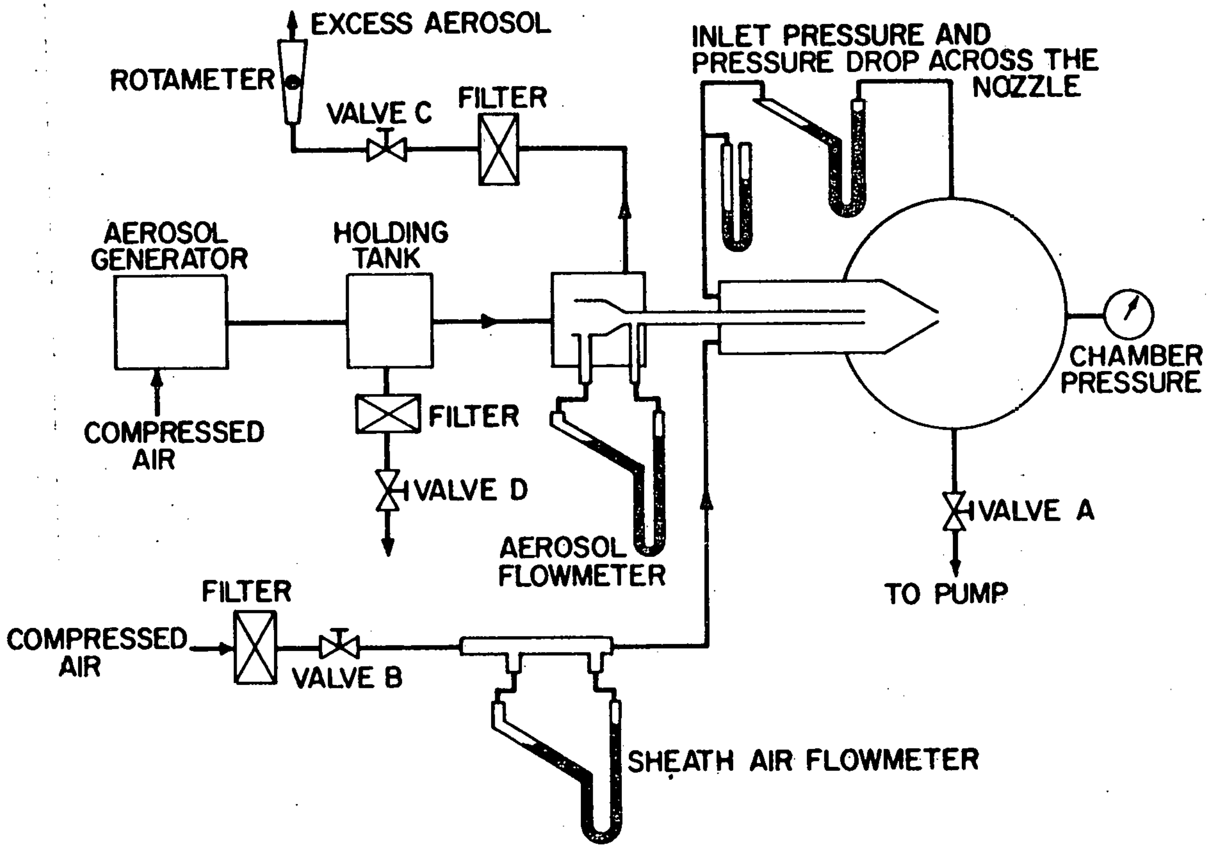

Figure 2.6 Flow system for small values of pressure drop.

to be 12.7 cm. Although intended for Poiselle flow, this flow meter was operated beyond its linear range and was calibrated for this condition.

The total flow through the nozzle was determined by placing a soap bubble flow meter between the chamber and valve A. The measured value of volumetric flow was corrected to a pressure of 72.6 cm of Hg (1036 cm H_2O), which again was the value of inlet pressure maintained for these trials. The flow conditions used for low flow tests are listed below.

Table 2.4 Flow conditions for small pressure drop flows

Pressure Drop Across the Nozzle - cm of H_2O	Total Flow lpm	Sheath Air Flow lpm
25.4	3.25	2.9
12.7	2.31	2.1
7.62	1.77	1.6
2.54	1.02	.9

To obtain these conditions, valves A, B, D and C were adjusted in sequence. Again, isokinetic sampling at the inlet of the aerosol flow nozzle was only important for the largest particles.

2.4 Measurement of Particle Velocity

2.4.1 The Laser-Doppler Velocimeter

A laser-Doppler velocimeter (LDV) was used to measure particle velocity. These instruments are widely used in the study of fluid mechanics and appear in a number of configurations.

A recent review by Durst, Melling and Whitelaw (1976) discusses the principles of the method and illustrates some of its diversity.

In the present case, a configuration referred to as the dual beam configuration was used. In this method, a laser beam is split into two equally intense beams. The two beams are passed through a converging lens and thus are brought to a point of intersection. At the point where they overlap, they form interference fringes nearly parallel to the line which bisects the angle between the beams and perpendicular to the plane of the two beams. The fringe spacing, d_f, is given by:

$$d_f = \frac{\lambda}{2\sin(\phi/2)} \tag{2.2}$$

where λ is the wavelength of the laser radiation and ϕ is the angle between the beams. A particle passing through the fringes will scatter light, and the intensity of the scattered light will be modulated as the particle passes through the dark and bright fringes. The frequency of this modulation is directly proportional to the velocity of the particle in the direction perpendicular to the fringes. Radiation scattered from the particle is collected and focused onto a photo-sensitive device which measures the scattered intensity, and responds quickly enough so that the frequency of modulation, called the Doppler frequency, can be detected. The velocity of the particle, U_p, perpendicular to the fringes equals:

$$U_p = f_D\, d_f \tag{2.3}$$

where f_D is the Doppler frequency. A schematic diagram of the LDV system used in this experiment is presented in Figure 2.7.

The above explanation is commonly used to explain the frequency of dual beam Doppler signals, but is of little use in arriving at an understanding of the amplitude of the signal. This requires reference to Doppler theory and Mie theory. Such an explanation involves calculating the intensity of the radiation scattered by the particle from each beam using Mie theory. The frequency of the radiation scattered from each beam is calculated noting the respective Doppler shifts up and down due to the component of particle velocity along the axis of each beam. The radiation scattered from each beam is superimposed on the photosensitive device where the beat frequency emerges as the Doppler frequency and the intensity emerges from the Mie calculations. Such a calculation for a reference beam configuration is given by Adrian and Goldstein (1971). The problem of signal amplitude will not receive much attention in this work since the principal concern here is particle velocity, which can be calculated by either model.

The LDV used in this experiment was obtained from Thermo-Systems, Inc. (P. O. Box 3394, St. Paul, MN 55165), and TSI model numbers will be indicated for the major items. The transmitting optics (TSI Model 910) consists of a beam splitter, an angle reducer and focusing lens. For this experiment, two focusing lenses were used with the beam splitter and angle reducer: a 551.2 mm focal length lens for the larger particles, and a 243.5 mm focal length lens for the smaller particles. The angle reducer

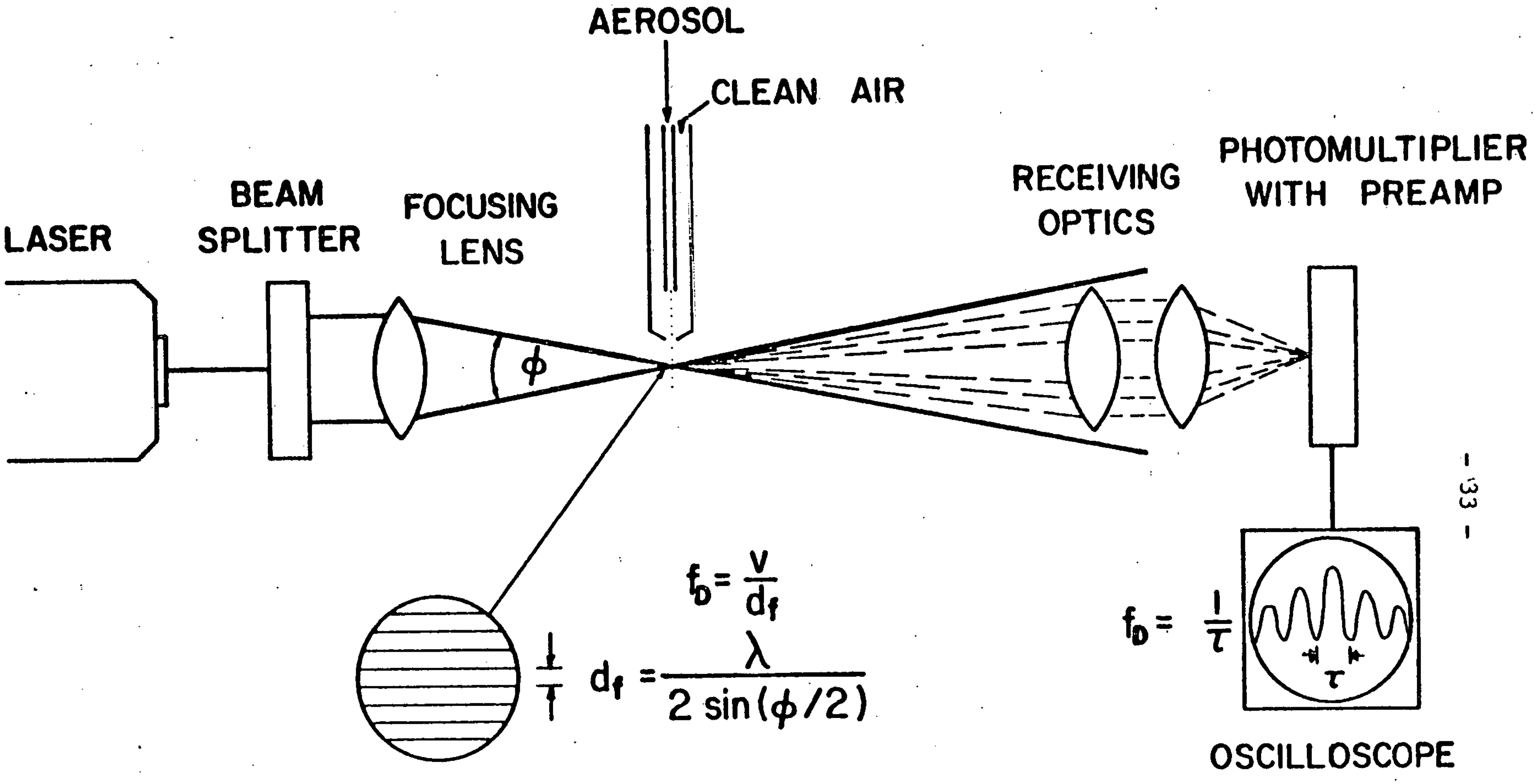

Figure 2.7 Diagram of LDV system.

reduces the beam separation to 22 mm, and the resulting values of ϕ become 5.09° for the 243.5 mm lens and 2.28° for the 551.2 mm lens (Instruction Manual, 900 Series Laser Optics, Thermo-Systems, Inc.).

Two lasers were used in the experiment: a Spectra-Physics (1250 W. Middlefield Rd., Mountain View, CA 94042) Model 120, 5 mw He-Ne laser for larger particles, and a Spectra-Physics Model 124, 15 mw He-Ne laser for smaller particles. The wavelength of the radiation is 632.8 nm. The resulting fringe spacings from Equation (2.2) are 15.9 μm for the 551.2 mm lens and 7.13 μm for the 243.5 mm lens.

The receiving optics were fashioned from standard TSI components. A Model 935 lens, focal length 193 mm, was attached to two Model 937 lenses, focal lengths 102.5 mm and 104.5 mm, to fashion a lens having a focal length of approximately 50 mm. This allows the collection lens to be placed close to the nozzle and, hence, intercept a larger fraction of the scattered radiation. This lens was fixed approximately 50 cm from the photomultiplier (PM) and the aperture plate. The TSI Model 960 photomultiplier includes the preamplifier and power supply. The PM aperture limits what is seen by the PM, and two such plates were used in this study. A .11 cm diameter aperture was used with the 243.5 mm lens, and a .19 cm diameter aperture was used with the 551.2 mm lens. Figure 2.8 shows a diagram of the receiving optics, and Figure 2.9 is a photograph of the entire optical system including the chamber. The chamber windows

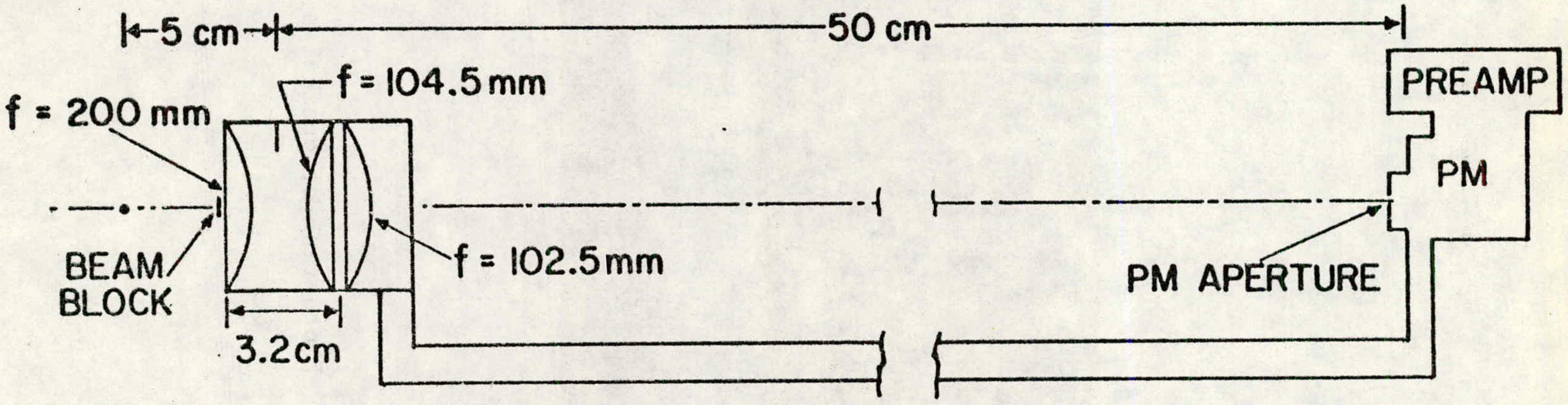

Figure 2.8 Diagram of receiving optics.

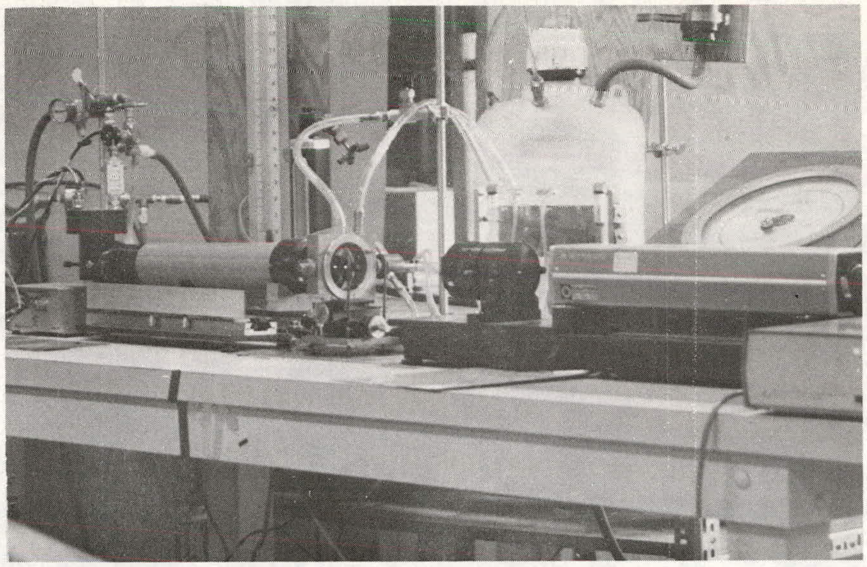

Figure 2.9 Photograph of optical system.

are coated to reduce reflections. When the system is properly aligned, the images of the fringes can be seen and counted on the aperture plate. The smaller aperture accommodates 17 fringes, and the larger accommodates 13 when used with their respective lenses. Table 2.5 below summarizes the optical parameters.

2.4.2 Alignment of Optics and Chamber

The optics and chamber must be aligned and positioned so that the velocity is measured at a known repeatable position and the path of the particles is perpendicular to the fringes. Figure 2.10 is provided to simplify the explanation of the alignment and shows two planes, both perpendicular to the plane containing the two crossing laser beams. Plane A is parallel to the planes containing the fringes, and Plane B is perpendicular to those planes. The procedure followed is listed below:

a) The unfocused split laser beam was allowed to fall on the window of the chamber, and the chamber position and leveling screws were adjusted until the beams reflected off the window were colinear with the incident beams. The object was to place the axis of the nozzle in a plane parallel to Plane B.

b) The leveling screws on the base of the chamber are adjusted so that when the transverse position screw is turned (see Figure 2.4), the tip of the nozzle passes through each of the split beams. The object was to orient the axis of the nozzle so that it is perpendicular to Plane A.

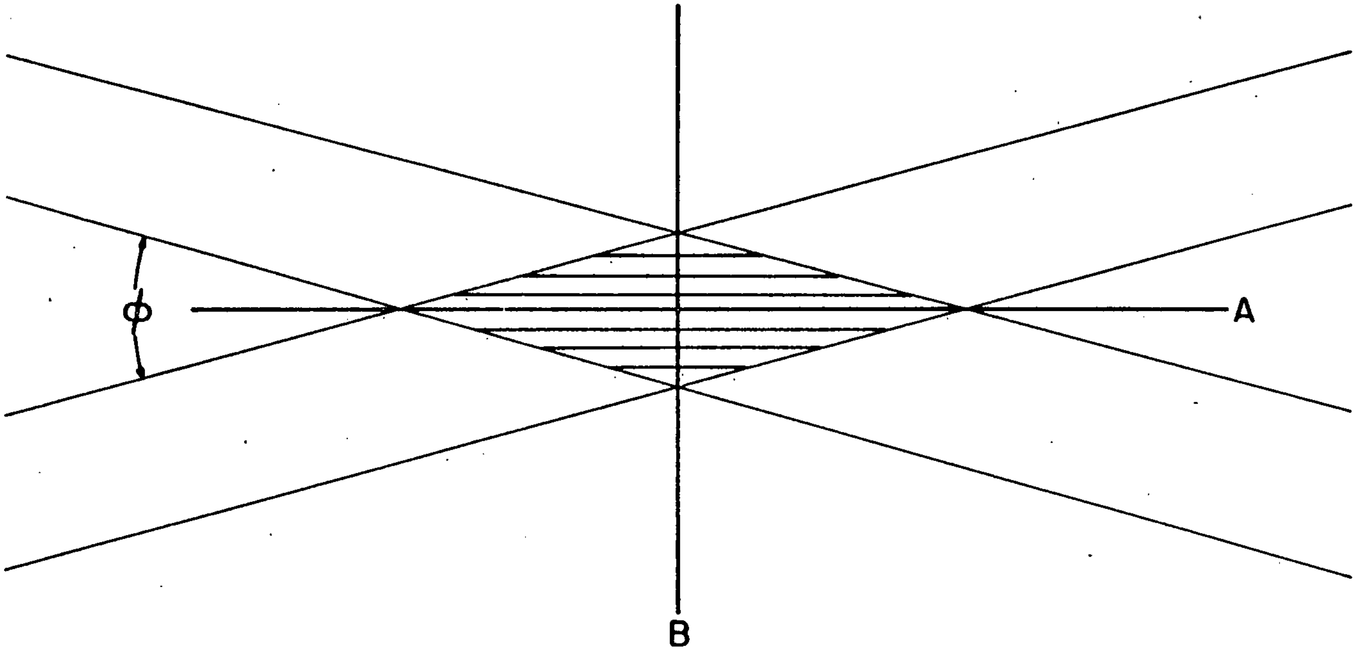

Figure 2.10 Alignment planes in LDV measuring volume.

c) The focusing lens was attached to the beam splitter and angle reducer, and the receiving optics assembly was moved as a unit until the beam intersection volume was imaged on the PM aperture plate. The position of the receiving optics unit was adjusted until the image of the beam intersection point remained nearly circular as the beams were alternately blocked. This was to insure that Plane B is being imaged onto the PM aperture plate. Then the nozzle is moved using the axial and transverse adjustment screws until the shadow of the nozzle was sharply focused on the PM aperture plate and did not change position much as the beams are alternately blocked. This procedure is intended to insure that the axis of the nozzle is in Plane B.

d) A microscope was placed so that the images of the fringes could be seen and counted on the PM aperture plate. The aperture and nozzle were positioned, without changing the plane of either, so that a specified number of fringes fall between the image of the nozzle and the aperture. Also, the PM aperture was positioned near the center of the circular image of the intersection volume, and on the axis of the nozzle. Therefore, the particles passed through the center of the intersection volume of tbe beams and were only seen by the PM when they are near the brightest portion of that volume.

e) The last step was to block the main beams after they emerge from the chamber so that only light scattered by particles reached the PM. This is accomplished by making a mask of black tape to block the beams and other stray light. The optical parameters are given in Table 2.5.

Table 2.5 Optical parameters for experiments

Focal length of focusing lens mm	d_f μm	PM aperture diameter cm	Number of fringes from nozzle to aperture	Particle diameter μm
551.2	15.9	.19	4	3 - 11.3
243.5	7.13	.105	16	.5 - 3

As is indicated below, the frequency counter measures Doppler frequency by timing the passage of eight Doppler cycles. Thus, the determination of particle velocity occurs in a volume having the cross-sectional area of the aerosol flow and a length of eight fringes. The size of this measuring volume is important in determining the possibility of coincidence, and this is discussed in Chapter 5. The location of the center of this measuring volume is needed for the theoretical calculations, for it will be assumed that the velocity at this point equals the average velocity measured over the eight-fringe interval. In the present case, the center of the measuring volume is four fringes beyond the edge of the aperture. Allowing for some uncertainty in the placement of the nozzle shadow and the edge of the aperture, it is possible to estimate the distance from the nozzle exit to the center of the measuring volume. Allowing 9 ± 1 fringes for the $d_f = 15.9$ μm case, and 21 ± 1 fringes for the $d_f = 7.13$ μm case, particles travel some 145 μm ± 15 μm from the nozzle exit to the center of the measuring volume.

2.4.3 Counting and Analysis of Doppler Frequency

The method described above produced highly uniform signals which could have been measured on an oscilloscope. Figure 2.11 shows the oscilloscope display of the output of the PM for data taken in trial 64E. This photograph is a time exposure encompassing hundreds of individual Doppler signals. However, a counter was used to provide accurate measurement of the frequency of a large number of individual signals, thus allowing analysis of the frequency distributions produced for each trial.

A modified TSI 1094 counter was used in this experiment. This modified counter had a 500 MHz clock. The processing of signals by this counter is illustrated in Figure 2.12 (Laser Anemometer Systems, Thermo-Systems, Inc.). A high pass filter removes the low frequency component from the signal so that it oscillates about zero rather than above it. The cut-off for this filter can be set from the front panel of the instrument. A Schmitt trigger then converts the Doppler signal to a square wave. The Schmitt trigger is activated when the Doppler signal crosses zero after it has crossed the threshold. The threshold crossing arms the Schmitt trigger, and its inclusion is intended to prevent noise near zero from activating the Schmitt trigger. The value of the threshold can be set from the front panel. The resulting square wave is timed for five cycles and eight cycles by a 500 MHz

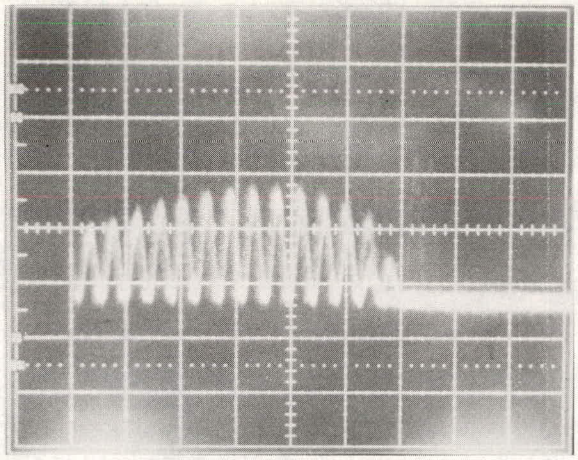

Figure 2.11 Oscilloscope display of Doppler signal Trial 64E, 2 μs/div.

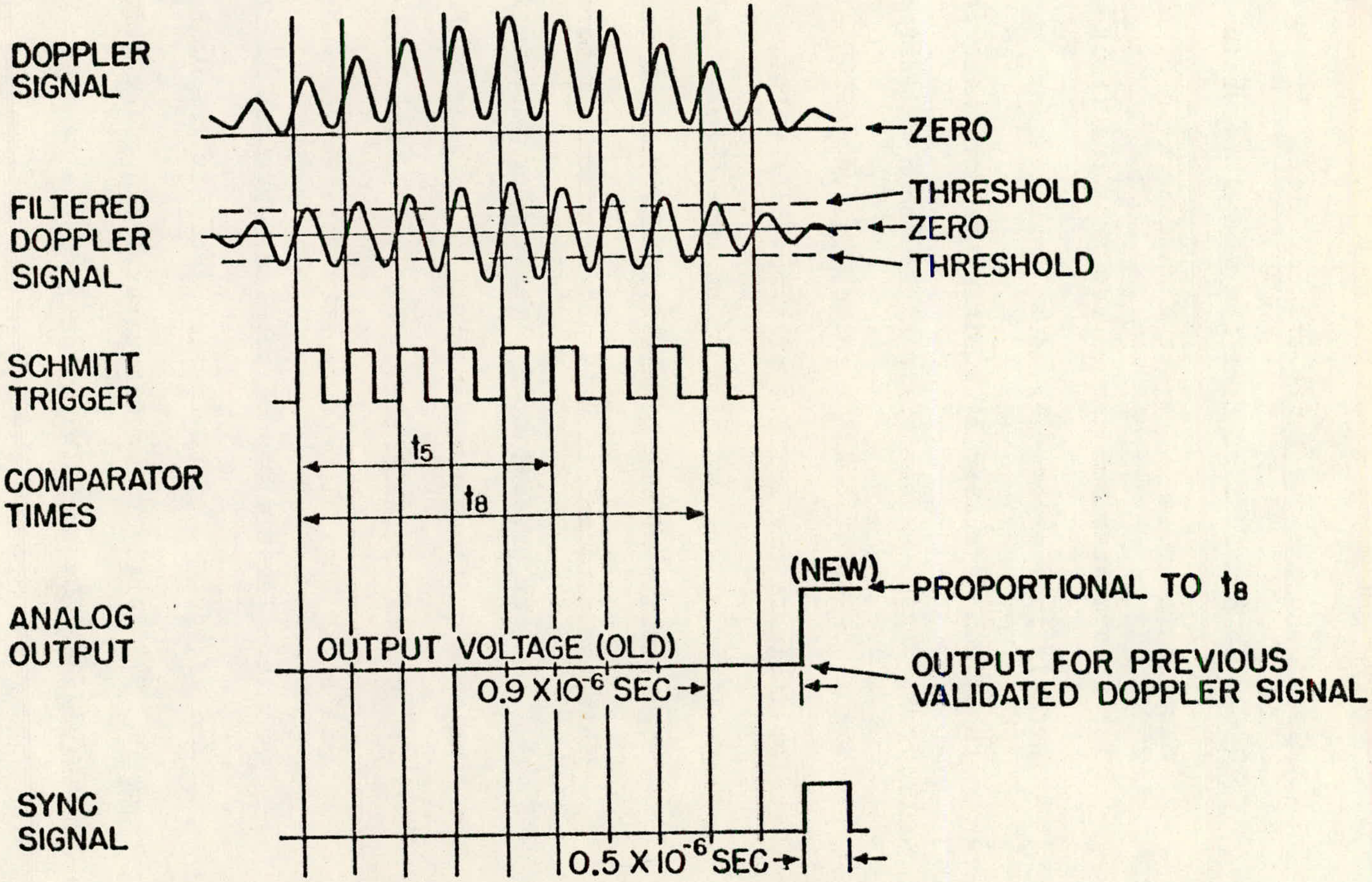

Figure 2.12 Processing of a Doppler signal by the counter.

clock, and the two times are compared. If the ratio of the two times is nearly 5/8, then the signal is validated. This procedure is intended to reject data generated by noise. The criterion for this comparison can be set from the front panel. The output used in this experiment is an analog signal nearly proportional to the time and scaled by a binary factor which is read out on the front panel. After a signal has been validated, the output analog signal is updated and a pulse, called a SYNC signal, is generated to indicate the arrival of a new data point. The counter was modified by the addition of an end-of-burst detector, but the high quality of the Doppler signals reduced the importance of this addition and it will not be discussed here.

In the present study, the analog output signal was analyzed using a multi-channel analyzer (MCA) made by Nuclear Data Inc. (P. O. Box 451, Palatine, IL 60067), consisting of a Model ND560 Analog to Digital Converter, a Data Handling Module, and a Memory Module. The MCA was DC coupled, operated in the coincidence mode and gated by a pulse from a Tektronix (P. O. Box 500, Beaverton, OR 97005) 115 Pulse Generator. The pulse generator was of course triggered by the SYNC pulse from the counter. Since the MCA requires a gate of at least 1 μs duration, and the SYNC pulse lasts only .5 μs, the pulse generator was introduced. Thus, the MCA samples the analog signal from the counter when gated by a pulse triggered by the SYNC pulse. The input impedance of the ND560 is only 1000 ohms. Therefore, a high-input-impedance, unity-gain amplifier was introduced in the analog circuit between the MCA and the counter so that the counter output would not be loaded down. A block diagram showing this arrangement is presented in Figure 2.13, and Figure 2.14 is a photograph of the electronics.

The counter was calibrated using a sinewave with a frequency counter at the input and a digital multimeter at the output. The MCA was calibrated using a DC supply, a voltage divider and a digital multimeter. Equations (2.4) and (2.5) give the calibration relations for the counter where V_c is the output voltage in volts, and f_c is the calibrating frequency in Hz. The exponent n is the range and is given on the front panel of the counter.

$$f_c = \frac{313.8 \times 10^6}{(2^n)V_c} + 209 \times 10^3; \ 10 \text{ MHz} < f_c < 50 \text{ MHz} \quad (2.4)$$

$$f_c = \frac{316.2 \times 10^6}{(2^n)V_c} - 3.9 \times 10^3; \ .75 \text{ MHz} < f_c < 10 \text{ MHz} \quad (2.5)$$

These relations result from linear regressions performed on five or more data points in each interval. The regression coefficients were greater than .9999. Equation (2.6) presents the calibration relation for the MCA with V_c being the voltage and C_h, the channel number. The instrument was set on a nominal conversion gain of eight volts per 256 channels.

$$V_c = (.0317)\ C_h + .0837 \quad (2.6)$$

This relation results from a regression done on five points. Each point was the average of two voltages representing the channel boundaries. The regression coefficient was .99999997.

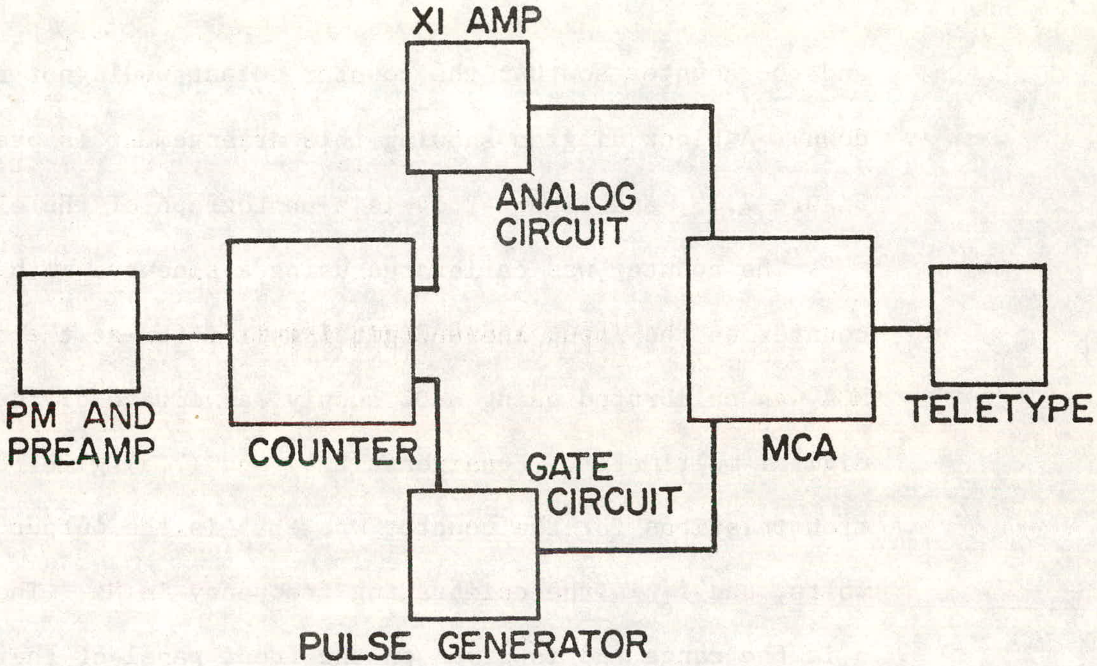

Figure 2.13 Block diagram of the electronics.

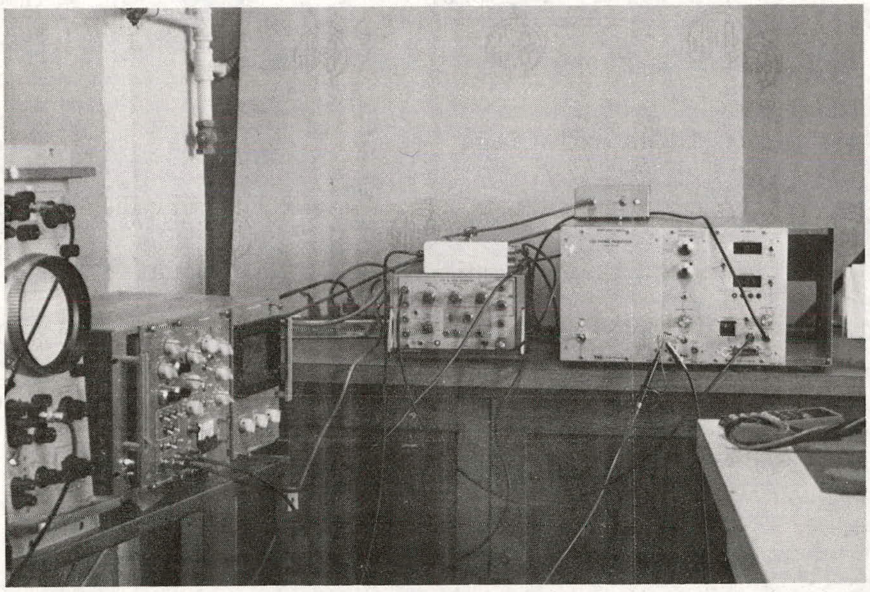

Figure 2.14 Photograph of the electronics.

The gain of the unit gain amplifier was found to be one to four significant figures.

Actual data-taking proceeded as follows. Particles were generated and the chamber and flow adjusted as described above. The output of the PM was viewed on the oscilloscope to insure that good Doppler signals were being produced. The gate pulse to the MCA was input into the second channel of the oscilloscope and the signals were added. When the counter was counting valid Doppler signals, a signal like that shown in Figure 2.15 was produced. These results from the arrival of the gate pulse after the Doppler have been counted and validated. Single-sweep triggering made it possible to verify that gate pulses were generated in response to genuine Doppler signals. In order to obtain the proper response to genuine Doppler signals, the high voltage on the PM tube, the gain on the counter amplifier and the threshold on the counter were adjusted. A signal-to-noise ratio of about three to one was sought, and signal amplitudes greater than 30 mv were needed. The comparator accuracy on the counter was set to two, which requires the five-to-eight comparison to be within a few percent of 5/8. The counter was allowed to auto range until a convenient value of n was displayed, and then it was switched to the hold range position, after which n remained constant. For smaller particles, a low-pass filter was used to improve the signal-to-noise ratio. The high-pass filter on the counter was set to a value less than the frequency being counted.

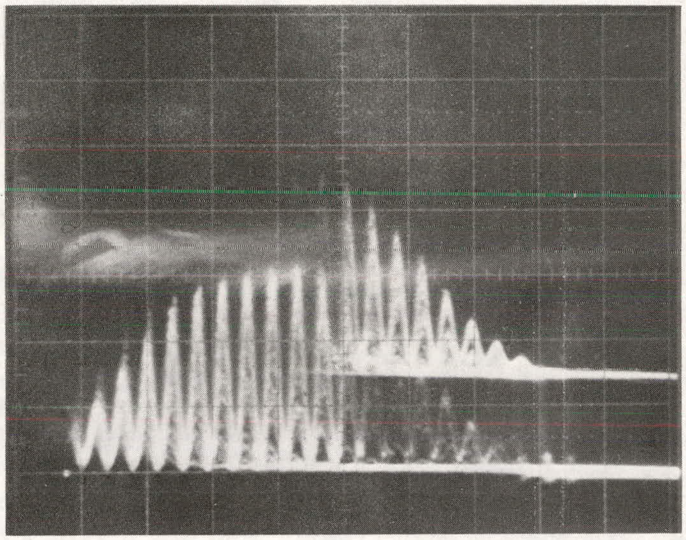

Figure 2.15 Oscilloscope display of Doppler signal and gate pulse superposed.

For example, in the case of trial 64E, 3.04 μm oleic acid particles were measured using the 35 mw laser and 551.2 mm focusing lens; the amplifier gain was set on 10, the threshold on 5.3, the high-pass filter on .5 MHz. The Doppler signal from the PM had an amplitude of nearly 100 mv; the frequency measured on the scope (see Figure 2.10) equaled approximately 1.2 MHz, and that resulting from the MCA analysis was 1.19 MHz. The raw data output from the MCA for this trial (64E) is given in Appendix E. This result demonstrates that the frequency counting and data analyzing electronics were calibrated and used in such a way that valid Doppler signals were accurately counted.

Not every particle, however, generated a Doppler signal which was counted, validated and analyzed. Using the single-sweep method of checking the data validation revealed that often a significant fraction of the obviously correct Doppler signals were not counted by the counter. These unmeasured signals were indistinguishable on the scope from many which were measured. Assuming that the signals were randomly ignored, this fact presents no problems for the determination of particle velocity and thus was not pursued.

2.5 Results

The measurements of Doppler frequency and particle velocity are reported in Tables 2.6, 2.7, 2.8 and 2.9 for various particle sizes and values of pressure drop across the nozzle. Each trial consisted of hundreds of individual measurements analyzed and stored by the MCA. Only the geometric mean, $\overline{f}_g$, and geometric

Table 2.6 $\bar{f}_g$, $\bar{U}_p$ and σ_g as a function of D_p and pressure drop

		.500 μm PSL				2.02 μm PSL				3.04 μm Oleic Acid		
Pressure Drop cm H_2O	Trial	$\bar{f}_g$ MHz	$\bar{U}_p$ m/s	σ_g	Trial	$\bar{f}_g$ MHz	$\bar{U}_p$ m/s	σ_g	Trial	$\bar{f}_g$ MHz	$\bar{U}_p$ m/s	σ_g
691	53A	39.2	279	1.04	53G	28.6	204	1.02	52C	11.6	184	1.014
484	53B	36.0	257	1.022	53H	26.4	188	1.02	52A	10.8	172	1.009
276	53C	28.0	200	1.024	53J	21.5	153	1.016	52F	8.86	141	1.01
69.1	53D	14.6	104	1.02	53K	12.3	87.7	1.01	52H	5.02	79.8	1.006

Table 2.7 $\overline{f}_g$, $\overline{U}_p$ and σ_g as a function of D_p and pressure drop

	3.8 µm Oleic Acid				6.1 µm Oleic Acid				7.7 µm Oleic Acid				9.0 µm Oleic Acid				11.3 µm Oleic Acid			
Pressure Drop cm H_2O	Trial	$\overline{f}_g$ MHz	$\overline{U}_p$ m/s	σ_g	Trial	$\overline{f}_g$ MHz	$\overline{U}_p$ m/s	σ_g	Trial	$\overline{f}_g$ MHz	$\overline{U}_p$ m/s	σ_g	Trial	$\overline{f}_g$ MHz	$\overline{U}_F$ m/s	σ_g	Trial	$\overline{f}_g$ MHz	$\overline{U}_p$ m/s	σ_g
691	52C	10.6	169	1.018	51C	8.65	138	1.017	51C	7.93	126	1.012	49A	7.55	120	1.016	49A	7.00	111	1.007
													49C	7.53	120	1.017	49C	6.99	111	1.016
484	52A	9.88	157	1.012	52I	8.28	132		51A	7.56	120	1.01	49F	7.03	112	1.009	49F	6.57	1.04	1.015
					51A	8.19	130	1.008	51D	7.66	122	1.01								
					51D	8.31	132	1.008												
					51I	8.25	131	1.008												
276	52F	8.06	128	1.009	51F	6.67	106	1.007	51F	6.08	96.7	1.01	49H	5.58	88.7	1.006	49H	5.12	81.4	1.013
													49V	5.59	88.9	1.007				
69.1	52H	4.59	73.0	1.006	51H	3.76	59.8	1.005	51H	3.42	54.4	1.006	49J	3.08	49.0	1.007	49J	2.76	43.9	1.010
													49P	3.09	49.1	1.008	49P	2.77	44.0	1.010

Table 2.8 $\overline{f}_g$, $\overline{U}_p$ and σ_g as a function of D_p and pressure drop

	.500 µm PSL				.794 µm PSL				1.10 µm PSL				2.02 µm PSL				3.04 µm Oleic Acid			
Pressure Drop cm H_2O	Trial	$\overline{f}_g$ MHz	$\overline{U}_p$ m/s	σ_g	Trial	$\overline{f}_g$ MHz	$\overline{U}_p$ m/s	σ_g	Trial	$\overline{f}_g$ MHz	$\overline{U}_p$ m/s	σ_g	Trial	$\overline{f}_g$ MHz	$\overline{U}_p$ m/s	σ_g	Trial	$\overline{f}_g$ MHz	$\overline{U}_p$ m/s	σ_g
25.4	66C	8.97	64.0	1.009	66M	8.90	63.5	1.01	65Q	8.50	60.6	1.009	65M	7.82	55.8	1.011	64N	3.21	51.0	1.007
	66AA	8.93	63.7	1.012	66AF	8.91	63.5	1.010	66AM	8.69	62.0	1.013	65AM	7.85	56.0	1.012	64R	3.24	51.5	1.007
	66AE	8.97	64.0	1.012	65V	8.84	63.0	1.010									65C	7.08	50.5	1.006
	65X	8.91	63.5	1.014													63M	3.17	50.4	1.011
	65ZZZ	8.91	63.5	1.010													63N	3.26	51.8	1.006
12.7	66F	6.38	45.5	1.008	66L	6.34	45.2	1.007	65P	6.13	43.7	1.008	65L	5.76	41.1	1.012	63A	2.40	38.2	1.005
	66G	6.32	45.1	1.008	66AG	6.34	45.2	1.008	66AL	6.24	44.5	1.009	66AL	5.78	41.2	1.009	64J	2.40	38.2	1.008
	66AB	6.34	45.2	1.008	65U	6.28	44.8	1.006												
	65Y	6.28	44.8	1.01																
7.62	66H	4.92	35.1	1.011	66K	4.93	35.2	1.007	65O	4.81	34.3	1.01	65K	4.55	32.5	1.006	62A	1.93	30.7	1.006
	66AC	4.92	35.1	1.007	66A	4.97	35.4	1.007	65R	4.82	34.4	1.009	66AK	4.59	32.7	1.009	63I	1.89	30.1	1.005
	65Z	4.87	34.7	1.01	65T	4.90	34.9	1.01	66AK	4.86	34.7	1.008					64F	1.92	30.5	1.006
																	65B	4.27	30.4	1.007
2.54	66I	2.89	20.6	1.009	66J	2.91	20.7	1.007	65N	2.85	20.3	1.008	65J	2.77	19.8	1.008	65A	2.66	19.0	1.005
	66AD	2.88	20.5	1.007	66AI	2.86	20.4	1.007	66AJ	2.86	20.4	1.006	66AJ	2.79	19.9	1.006	64A	1.20	19.1	1.005
	65ZZ	2.86	20.4	1.008	65S	2.86	20.4	1.007									64E	1.19	18.9	1.005
					65W	2.85	20.3	1.005									64AB	1.20	19.1	1.004

Table 2.9 $\overline{f}_g$, $\overline{U}_p$ and σ_g as a function of D_p and pressure drop

Pressure Drop cm H_2O		3.8 µm Oleic Acid				6.1 µm Oleic Acid				7.7 µm Oleic Acid				9.0 µm Oleic Acid				11.3 µm Oleic Acid		
	Trial	$\overline{f}_g$ MHz	$\overline{U}_p$ m/s	σ_g	Trial	$\overline{f}_g$ MHz	$\overline{U}_p$ m/s	σ_g	Trial	$\overline{f}_g$ MHz	$\overline{U}_p$ m/s	σ_g	Trial	$\overline{f}_g$ MHz	$\overline{U}_p$ m/s	σ_g	Trial	$\overline{f}_g$ MHz	$\overline{U}_p$ m/s	σ_g
25.4	64N	2.95	46.9	1.009	61H	2.50	39.8	1.007	61H	2.26	35.9	1.009	62T	2.03	32.3	1.007	62T	1.81	28.8	1.01
	64R	2.98	47.4	1.009																
	65C	6.55	46.7	1.007																
	63M	2.92	46.4	1.02																
	63N	3.02	48.1	1.007																
12.7	63A	2.23	35.5	1.008	61A	1.99	31.6	1.01	61A	1.79	28.5	1.009	62X	1.56	2.48	1.006	62X	1.40	22.3	1.01
	64J	2.20	35.0	1.015	61B	1.93	30.7	1.006	61B	1.75	27.8	1.006								
7.62	62A	1.82	28.9	1.007	61P	1.55	24.6	1.005	61P	1.41	22.4	1.006	62N	1.26	20.0	1.007	62N	1.14	18.1	1.011
	63I	1.77	28.1	1.007																
	64F	1.76	28.0	1.013																
	65B	3.97	28.3	1.005																
2.54	65A	2.53	18.0	1.005	61L	1.01	16.1	1.004	61L	.922	14.7	1.006	62S	.842	13.4	1.004	62S	.756	12.0	1.007
	64A	1.13	18.0	1.009																
	64E	1.13	18.0	1.009																
	64AB	1.14	18.1	1.006																

standard deviation, σ_g, are reported for each distribution of Doppler frequency. The velocity, $\overline{U}_p$, reported for each distribution equals $(d_f)(\overline{f}_g)$. Definitions of $\overline{f}_g$ and σ_g are given in Equations (2.6) and (2.7). Clearly, σ_g applies to both the velocity and Doppler frequency distributions.

$$\ln \overline{f}_g = \frac{\Sigma\, N_i[\ln f_{Di}]}{\Sigma\, N_i} \tag{2.6}$$

where N_i is the number of counts in the i^{th} channel of the MCA output, and f_{Di} is the Doppler frequency corresponding to that channel as calculated by Equations (2.6) and (2.4) or (2.5).

$$[\ln \sigma_g]^2 = \frac{\Sigma\, N_i[\ln f_{Di} - \ln \overline{f}_g]^2}{(\Sigma\, N_i) - 1} \tag{2.7}$$

The output of the MCA for nine representative trials is given in Appendix E. The brackets indicate which channels were included in the calculations of $\overline{f}_g$ and σ_g. As can be seen from the sample output, channels containing counts were excluded from the calculations. For example, oleic acid aerosols containing primary and doublet particles produce two easily distinguished peaks, but there are non-zero channels between the peaks which are not easily assignable. Such channels are not included in the analysis. In most trials, the total number of counts attributed to a given particle size exceeds 1000. Exceptions include doublet particle sizes for some trials and occasional PSL trials. Of the approximately 95 trials which were analyzed, four were excluded from this tabulation. Three of these were associated with questionable aerosol generating conditions, and the fourth varied too much from four other trials at the same conditions and was rejected.

Figures 2.16, 2.17, and 2.18 are graphs of the experimental data with particle velocity shown as a function of particle diameter and pressure drop across the nozzle. In those cases where three or more trials were analyzed for a single set of conditions, the graphical presentation consists of the mean of the values of $\overline{U}_p$ and error bars indicating the 95% confidence interval about the mean. This confidence interval equals $\pm 2\sigma_m$ where:

$$\sigma_m = \frac{\sigma}{\sqrt{N_t}} \tag{2.8}$$

N_t is the number of values of $\overline{U}_p$ averaged to find the mean and σ is the standard deviation of this set.

These results show that the particle velocity does depend upon both the size of the particle and the flow rate in the nozzle. The curves in the figures were drawn to suggest the dependence on density which is discussed in detail in the next two chapters. The mismatch between the PSL and oleic acid curves could have been ignored by paying less strict attention to the points representing multiple trials and by attempting to join all the points in a smooth line. This was not done.

The resolution of the instrument depends upon its intrinsic dispersion, which is the width of the size distribution indicated by the instrument when measuring a perfectly monodisperse aerosol. The intrinsic dispersion may depend on the counter resolution,

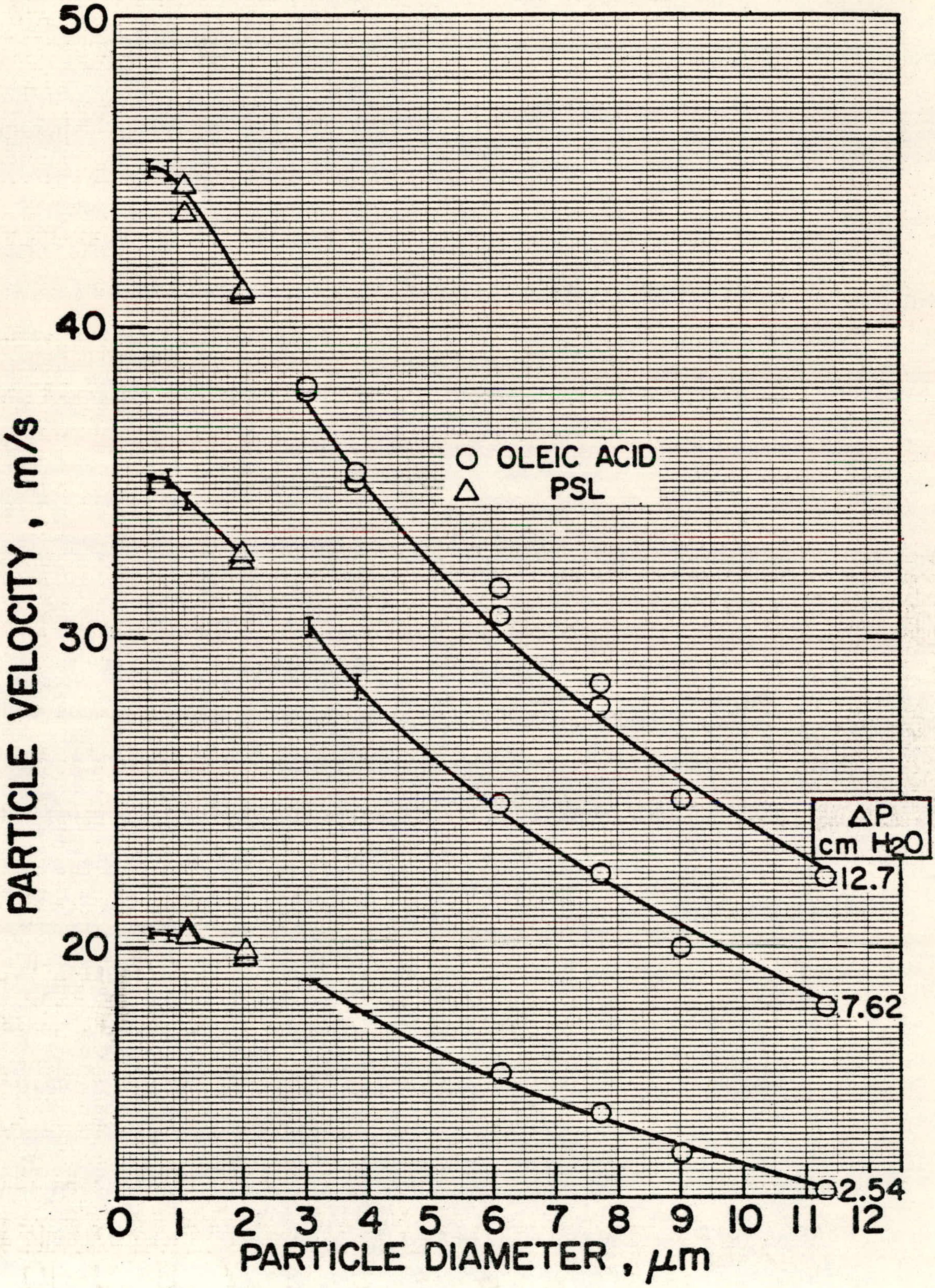

Figure 2.16 Measured particle velocity as a function of particle diameter.

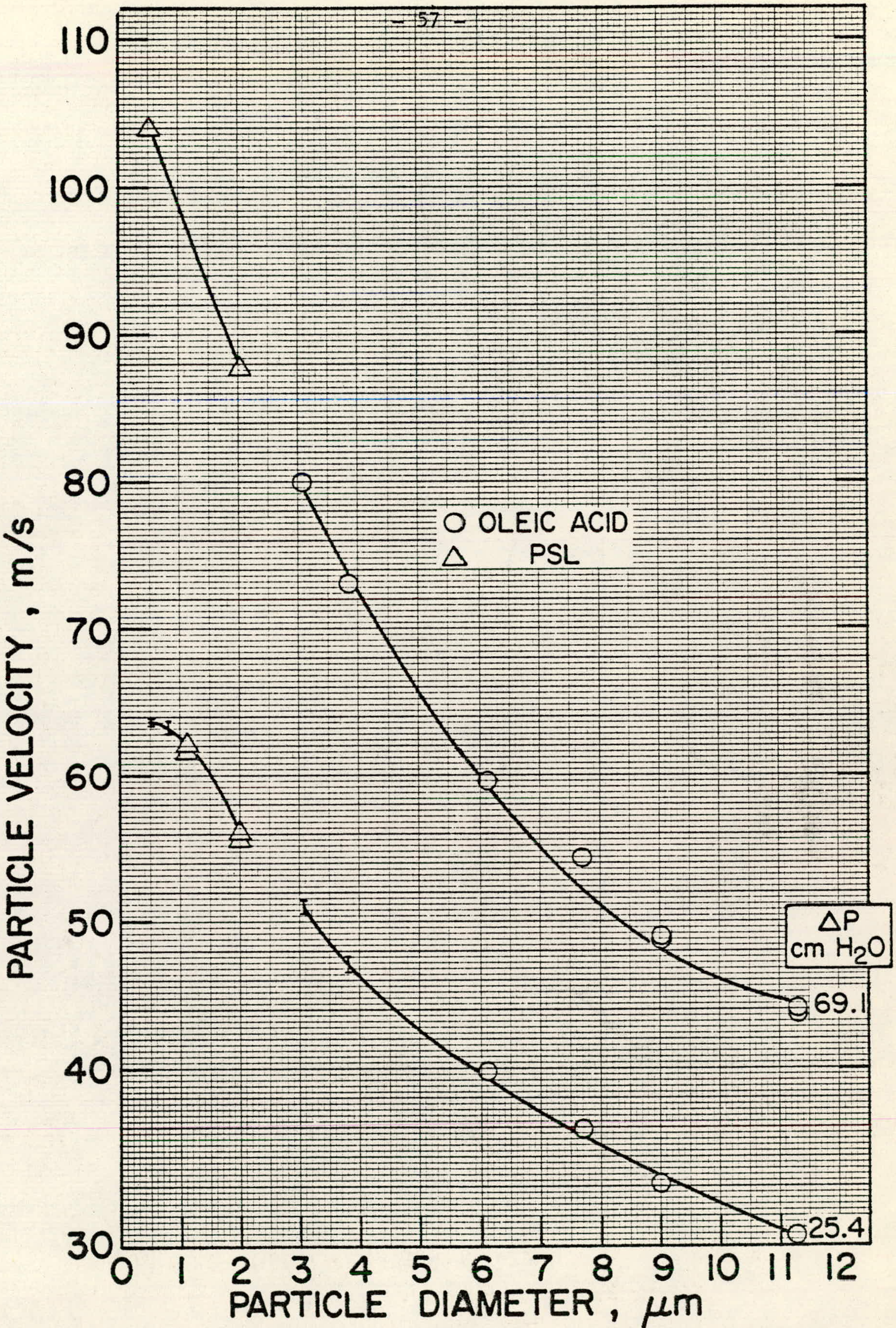

Figure 2.17 Measured particle velocity as a function of particle diameter.

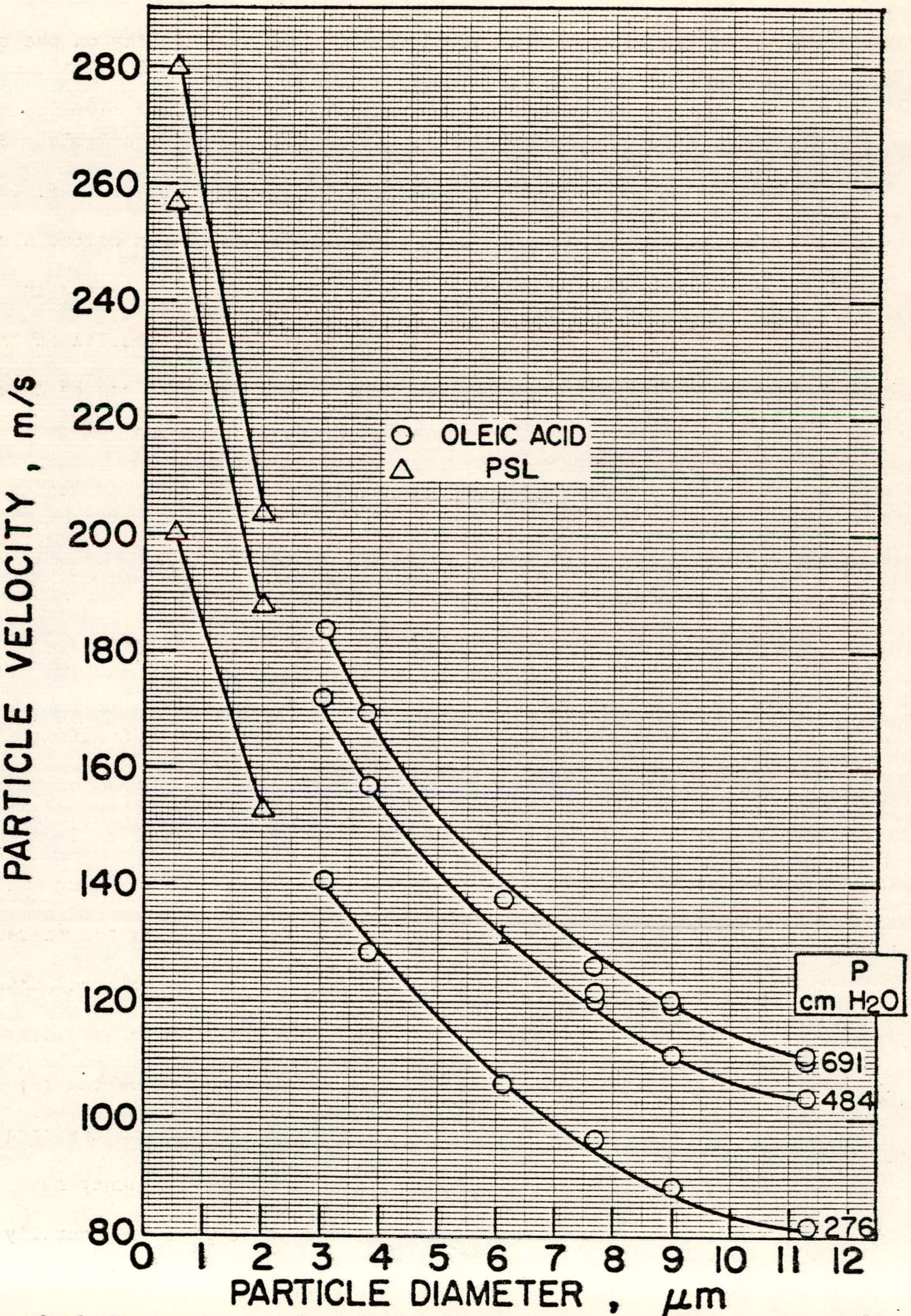

Figure 2.18 Measured particle velocity as a function of particle diameter.

turbulence in the jet, dependence of gas velocity on the radial position in the jet, etc.

Perfectly monodisperse aerosols are not available. So to evaluate the intrinsic dispersion of the instrument, it is necessary to compare the relative standard deviation of the size distribution as measured by the instrument, $(\sigma_{rs})_m$, with the actual relative standard deviation of the size distribution of the test aerosol, $(\sigma_{rs})_a$. Approximate values of $(\sigma_{rs})_a$ can be calculated from the information given in Section 2.2.

Values of $(\sigma_{rs})_m$ can be calculated from the relative standard deviation, σ_{rv}, of the corresponding velocity distribution, and the $\overline{U}_p$ vs. D_p curve.

$$(\sigma_{rs})_m \simeq \left(\frac{d\overline{U}_p}{dD_p}\right)^{-1} \frac{\sigma_{rv}}{D_p} \qquad (2.9)$$

where σ_{rv} equals σ_g-1, since the reported distributions are quite narrow. The results of several calculations are given below. The intrinsic dispersion of the instrument is seen to increase with decreasing particle size. Operating the test nozzle at 69.1 cm of H_2O provides very good resolution for micron-sized aerosols, but less adequate resolution for submicron aerosols.

As is indicated above, the counter measures the time for eight Doppler cycles with a 500 MHz clock. Thus the resolution of the counter for a single cycle is .25 ns, and the frequency resolution expressed as a fraction of the frequency is (.25 ns)(f_D). The tables indicate that σ_g-1 is generally

Table 2.10 Measured and actual values of the width of size distributions for selected test aerosols

	Pressure Drop			
	69.1 cm H_2O		691 cm H_2O	
D_p, μm	σ_{rs} Measured	σ_{rs} Actual	σ_{rs} Measured	σ_{rs} Actual
9	.02	.014	.02	.014
3	.02	.014	.04	.014
.5	.37	.005	.27	.005

more than three times the value of (.25 ns)($\overline{f}_g$), and so the resolution of the instrument is not limited by the counter.

The repeatability of the measurements determines the precision of the instrument. The four trials taken with D_p = 3.04 μm and a pressure drop of 7.61 cm of H_2O give an indication of repeatability. Both the flow and the nozzle position were reset between each of the trials. The standard deviation of the four values of $\overline{U}_p$ from the mean of 30.4 x 10^2 cm/s is 300 cm/s. This implies a relative standard deviation of .01. However, the aerosol was also changed between trials, and that may well exaggerate the variability. Only one other set of conditions for which four or more trials was run produced a larger relative standard deviation. That was a value of .013 for 3.04 μm particles at 25.4 cm of H_2O pressure drop. Other conditions for which four or more trials were taken all resulted in smaller relative standard deviation. Therefore, .01 must be taken as a large value for variability. It should be noted that these calculations were only done for primary particles, and not for doublets. The value of .01 is very near the values of σ_{rv} which produced Table 2.10. The precision then is of the same order as the resolution. They are both adequate to allow measurements to be made on micron-sized aerosols. Submicron aerosols, however, may require some modification of the system, and that task is undertaken in later chapters.

CHAPTER 3

THEORETICAL ANALYSIS - TEST NOZZLE

3.1 Introduction

A theoretical analysis of particle motion in the test nozzle is presented in this chapter. The model developed and verified here will be used in later chapters to design a nozzle for use in a practical aerosol measuring instrument.

The first step in the analysis is to determine the flow field of air in the test nozzle. Then the motion of particles can be predicted. The flow field is first calculated using the boundary layer approximation for incompressible, laminar flow. The gas velocities on the centerline of the nozzle are then compared with those predicted assuming inviscid, incompressible plug flow (i.e., Bernouli's Law), and good agreement is found.

Using the information provided by the flow calculations, the velocity of particles is predicted from the equations of particle dynamics and is compared with the experimental results presented in Chapter 2. The good agreement between theory and experiment verifies the validity of the model and allows the confident application of the theory to practical nozzle design.

3.2 The Boundary Layer Calculation

The first task in the theoretical analysis is the determination of the fluid flow in the nozzle. Various approaches, some more complicated than others, are possible and it is necessary to choose one which fits the conditions found in the nozzle. It is possible to numerically solve the full Navier-Stokes equations for compressible flow (Gosman et al., 1970). But this is an expensive adventure in computing, and simplifying assumptions can be made which result in equations that are less demanding.

The first simplication involves calculating only for incompressible flow. The air can be considered to have constant density as long as the pressure drop across the nozzle is small compared to atmospheric pressure. Although the ability to size small particles increases with gas velocity, experimental results indicate that sufficient resolution can be achieved at a relatively low pressure drop. This is beneficial because the lower gas velocities require less pumping power and limit the Reynolds numbers of the particles, and hence, the ill effects of being beyond the Stokes law regime. Therefore, incompressible flows will receive all the theoretical attention.

The second simplification involves the structure of the Navier-Stokes equations, and is referred to as the boundary layer approximation. This approximation is best known for its success in predicting the flows along a bounding surface. Schlichting (1968) shows that in these cases, it is possible to neglect transverse pressure gradients and velocity gradients along the direction of the flow. The resulting simplification produces equations which are much easier to treat than are the full Navier-Stokes equations. In the present study, the boundary layer equations are applied to the entire region of the flow and not only near the wall. This method is described by Patankar and Spalding (1970) who argue that it is applicable when there exists a "single, predominant direction of flow...and the only significant shear stresses...are caused by the gradients in the directions normal to the streamlines." The present case fits these requirements. The boundary layer approximation is useful because it transforms the Navier-Stokes equations from the elliptic form in the axial direction to the parabolic form. That is, all second derivatives with respect to the axial position coordinate vanish. Therefore, it is possible to solve the equations numerically by a marching procedure, i.e., given the conditions at the inlet to the nozzle, the calculation proceeds down the axis to the exit and stops. When the full Navier-Stokes equations are to be solved, on the other hand, the presence of second derivatives in the axial direction requires that the region from entrance to exit be solved using an iterative procedure. Thus the boundary layer equations require less computer time and storage space than do the full Navier-Stokes equations.

Finally, the gas velocities were calculated only for laminar flows. This is clearly justified at the lower Reynolds number flows. At higher flows, the narrowness of the velocity distributions measured for the smallest particles suggests that turbulence is not an important factor in the nozzle.

The boundary layer approach resulted in good agreement between the theoretical and experimental particle velocities, even in the case where the pressure drop across the nozzle approached 30% of the absolute upstream pressure and the Reynolds number of the flow at the nozzle exit approached 14,000.

3.2.1 Equations to be Solved

The boundary layer equations follow from the Navier-Stokes equations and the equation of continuity. These latter three equations are listed for steady, laminar, incompressible, axially-symmetric flow (Landau and Lifschitz, 1959):

$$v\frac{\partial v}{\partial r} + u\frac{\partial v}{\partial x} = -\frac{1}{\rho}\frac{\partial P}{\partial r} + \frac{\mu}{\rho}\left(\frac{\partial^2 v}{\partial r^2} + \frac{\partial^2 v}{\partial x^2} + \frac{1}{r}\frac{\partial v}{\partial r} - \frac{v}{r^2}\right) \qquad (3.1)$$

$$v\frac{\partial u}{\partial r} + u\frac{\partial u}{\partial x} = -\frac{1}{\rho}\frac{\partial P}{\partial x} + \frac{\mu}{\rho}\left(\frac{\partial^2 u}{\partial r^2} + \frac{\partial^2 u}{\partial x^2} + \frac{1}{r}\frac{\partial u}{\partial r}\right) \qquad (3.2)$$

$$\frac{\partial v}{\partial r} + \frac{\partial u}{\partial x} + \frac{v}{r} = 0 \qquad (3.3)$$

where r is the radial coordinate and v is the radial velocity; x is the axial coordinate and u is the axial velocity; ρ is the gas density and μ is the gas viscosity; and P is the pressure.

The corresponding boundary layer equations are given by Patankar and Spalding (p. 20, p. 22) as:

$$\frac{\partial P}{\partial r} = 0 \qquad (3.4)$$

$$u\frac{\partial u}{\partial x} + v\frac{\partial u}{\partial r} = -\frac{1}{\rho}\frac{dP}{dx} + \frac{\mu}{\rho}\left(\frac{1}{r}\frac{\partial u}{\partial r} + \frac{\partial^2 u}{\partial r^2}\right) \qquad (3.5)$$

In order to arrive at Equations (3.4) and (3.5) from Equations (3.1) and (3.2), it is necessary to neglect all derivatives of v and the terms v/r^2. Partial differentiation of (3.3) with respect to x produces an equation for $\frac{\partial^2 u}{\partial x^2}$ in terms of the derivatives of v. Thus, this term is neglected with the others. The neglect of these terms is consistent with the qualitative condition that there is a predominant direction of flow and no significant shear stresses perpendicular to that direction.

3.2.2 Solution Method for the Boundary Layer Equations

The computer program used to solve the boundary layer equations was written by Baliga and Patankar (see Sparrow et al., 1977) and follows the method devised by Patankar and Spalding. The program can be applied to a broad range of problems. The present discussion, however, will focus on the particular application to the present problem and is adapted from that given by Patankar and Spalding. The derivation of the finite difference equation is discussed in more detail in Appendix A, and the program, named BNDARL, is listed in Appendix B with a glossary of terms. The program was executed on the University of Minnesota CDC 6400 computer with the MNF compiler.

The numerical solution of Equations (3.4) and (3.5) requires that they be expressed in finite difference form. First, Equation (3.5) is transformed so that the normalized stream function, ω, replaces the coordinate r as the cross-stream variable,

$$\omega = \frac{\Psi - \Psi_I}{\Psi_E - \Psi_I}, \qquad \frac{\partial \Psi}{\partial r} = \rho\, u\, r \tag{3.6}$$

where Ψ is the stream function and Ψ_I is the value of Ψ at the interior boundary of the calculation. Ψ_E is the value of Ψ at the exterior boundary. Under this transformation, and in the case of impermeable walls in enclosed flow, Equation (3.5) becomes:

$$\frac{\partial u}{\partial x} - \frac{\partial}{\partial \omega}\left(\frac{r^2\, \rho\, \mu\, u}{(\Psi_E - \Psi_I)^2}\,\frac{\partial u}{\partial \omega}\right) = -\frac{1}{\rho u}\,\frac{dP}{dx} \tag{3.7}$$

This equation expresses conservation of x-momentum, and is transformed into a finite difference equation by integration over a control volume in x-ω space, shown in Figure 3.1. The points represent the nodes at which the values of r, u, and P are to be calculated in the finite difference scheme. The index i is used to locate the cross-stream nodes and the i^{th} cross-stream node maintains its value of ω for all values of x.

In a marching procedure, the values of u, P and r for all the nodes at a given x can be calculated using the knowledge of the values at the previous x. Therefore, the integration will be done so that the resulting finite difference equation permits the calculation of the u_i, r_i and P at x based on the values at x-Δx. In addition, the equations will be linear in $u_i(x)$, the method will be stable regardless of downstream step size, and the conservation equations will apply over any number of control volumes.

In order to achieve these results, the derivatives with respect to ω are expressed in terms of values of u_i at x, and u is assumed to be linear between adjacent nodes in r for the evaluation of these derivatives. Also, all coefficients of $u_i(x)$ are expressed in terms of values at x-Δx.

The integration over the control volume produces an equation of the form:

$$a_i u_i(x) = b_i u_{i+1}(x) + c_i u_{i-1}(x) + d_i + e_i \frac{dP}{dx} \qquad (3.8)$$

where a_i, b_i, c_i, d_i and e_i are functions of ω_i, r_i and u_i evaluated at the position x-Δx. The values of r_i at x-Δx

3.1

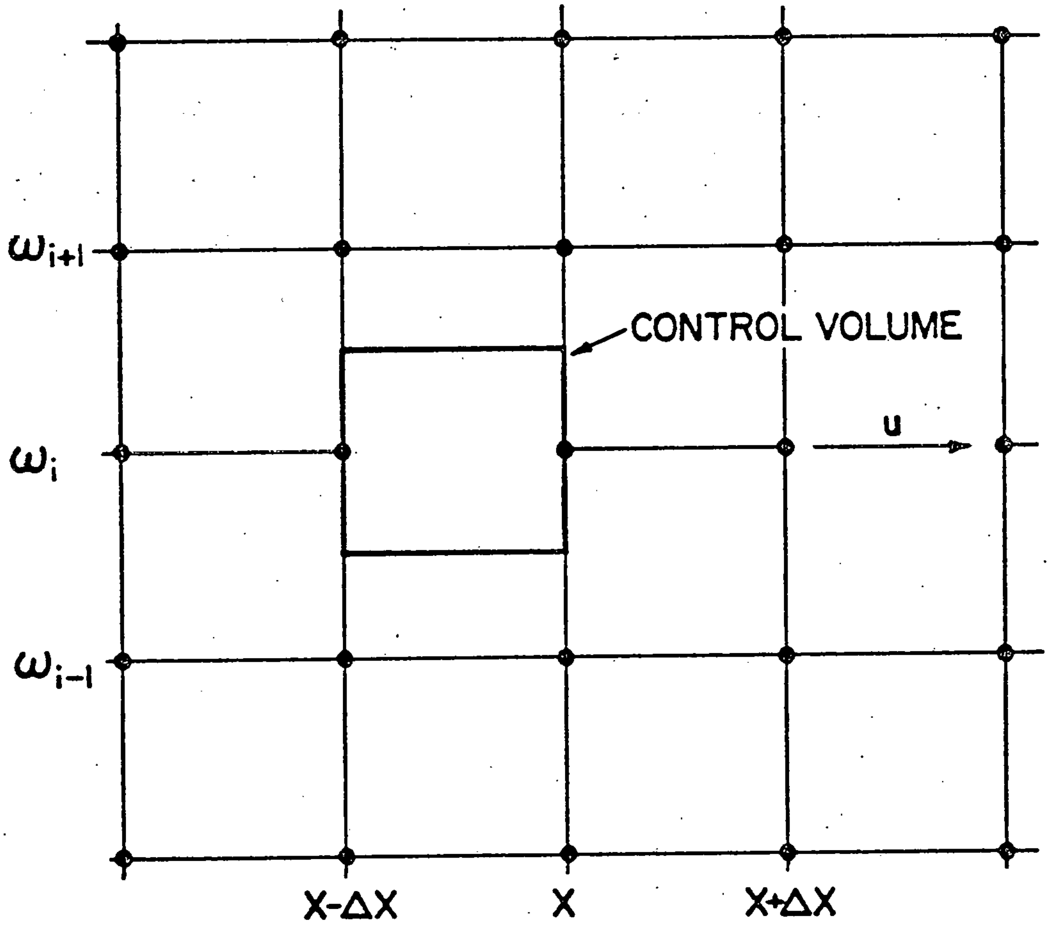

Figure 3.1 Nodes and a control volume for the boundary layer calculation.

are obtained by integrating Equations (3.6). Special equations are derived for the boundaries, but their form is similar.

For a given value of x, there is an equation like (3.8) for each node. In addition, $\frac{dP}{dx}$ is necessary for the solution of this system of equations. In confined flows, the value of $\frac{dP}{dx}$ is determined by the interaction of geometry and the conservation equations. The geometrical considerations are input into the solution process through the definition of stream function,

$$\int_{\Psi_I}^{\Psi_E} \frac{d\Psi}{\rho u} = \int_o^R rdr = \frac{R^2}{2} \qquad (3.9)$$

In the present case, R is the radius of the nozzle at the value of x under consideration. Equation (3.9) can be expressed in terms of ω and in discrete form,

$$2(\Psi_E-\Psi_I) \sum \frac{(\omega_{i+1}-\omega_i)}{\rho \; u_i} = R^2 \qquad (3.10)$$

Equation (3.10) is then added to the system of Equations (3.8) and the system is solved for the u_i and $\frac{dP}{dx}$ using an iterative technique described by Sparrow, Baliga and Patankar (1977).

Thus the solution proceeds across the nozzle from inlet to exit.

3.2.3 Check of the Flow Program

The program was checked by calculating the developing laminar flow in the entrance region of a cylindrical pipe and comparing the results with the published solution of Hornbeck (1963).

Hornbeck's method involved similar assumptions and is used here as a standard for checking BNDARL. In particular, the sensitivity of the calculation to the number of cross-stream nodes and downstream step size was checked.

Figures 3.2 and 3.3 show Hornbeck's solution and the results of boundary layer calculations of fluid velocity and pressure on the axis of the cylindrical pipe. The dimensionless variables referred to in the figure are defined as:

$$u^* = \frac{u}{\bar{u}}$$

$$x^* = \frac{x\,\mu}{R^2\bar{u}\rho} \qquad (3.11)$$

$$P^* = \frac{P-P_o}{\bar{u}^2\rho}$$

where $\bar{u}$ is mean axial velocity, R is the radius of the pipe, and P_o is the pressure at the inlet.

The maximum step size was varied from $\Delta x^* = .0005$ to $\Delta x^* = .005$ without significantly altering the results. However, the figures indicate that the number of cross-stream nodes does affect the results. The calculated velocity and pressure more closely approached Hornbeck's result as the number of cross-stream nodes increased. However, the cost of the computer calculation also increases with the number of nodes and a balance must be struck. It seems that the improvement from 90 nodes to 200 nodes does not justify the more than doubling in cost that it entails.

3.2

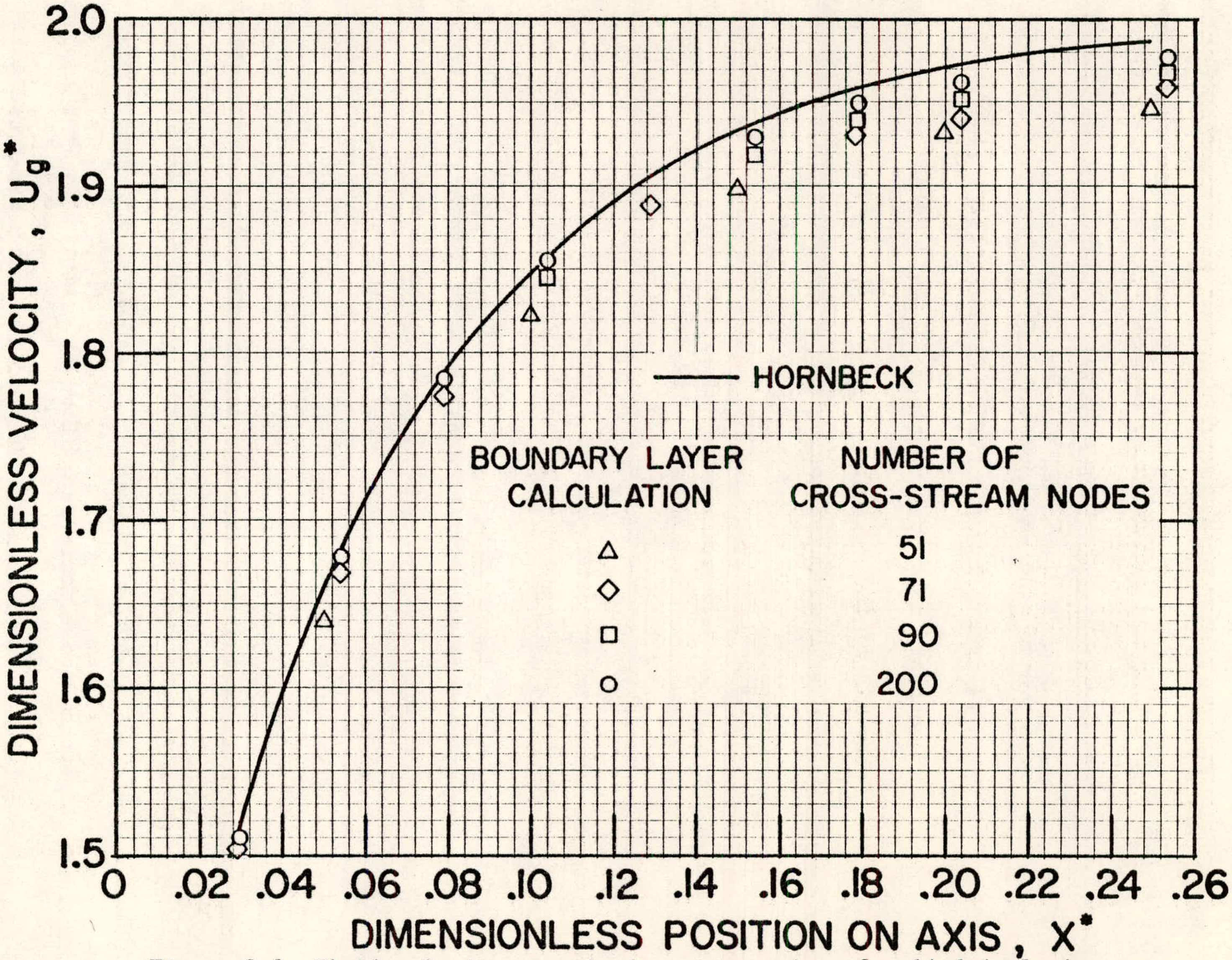

Figure 3.2 Fluid velocity on axis in entry region of cylindrical pipe.

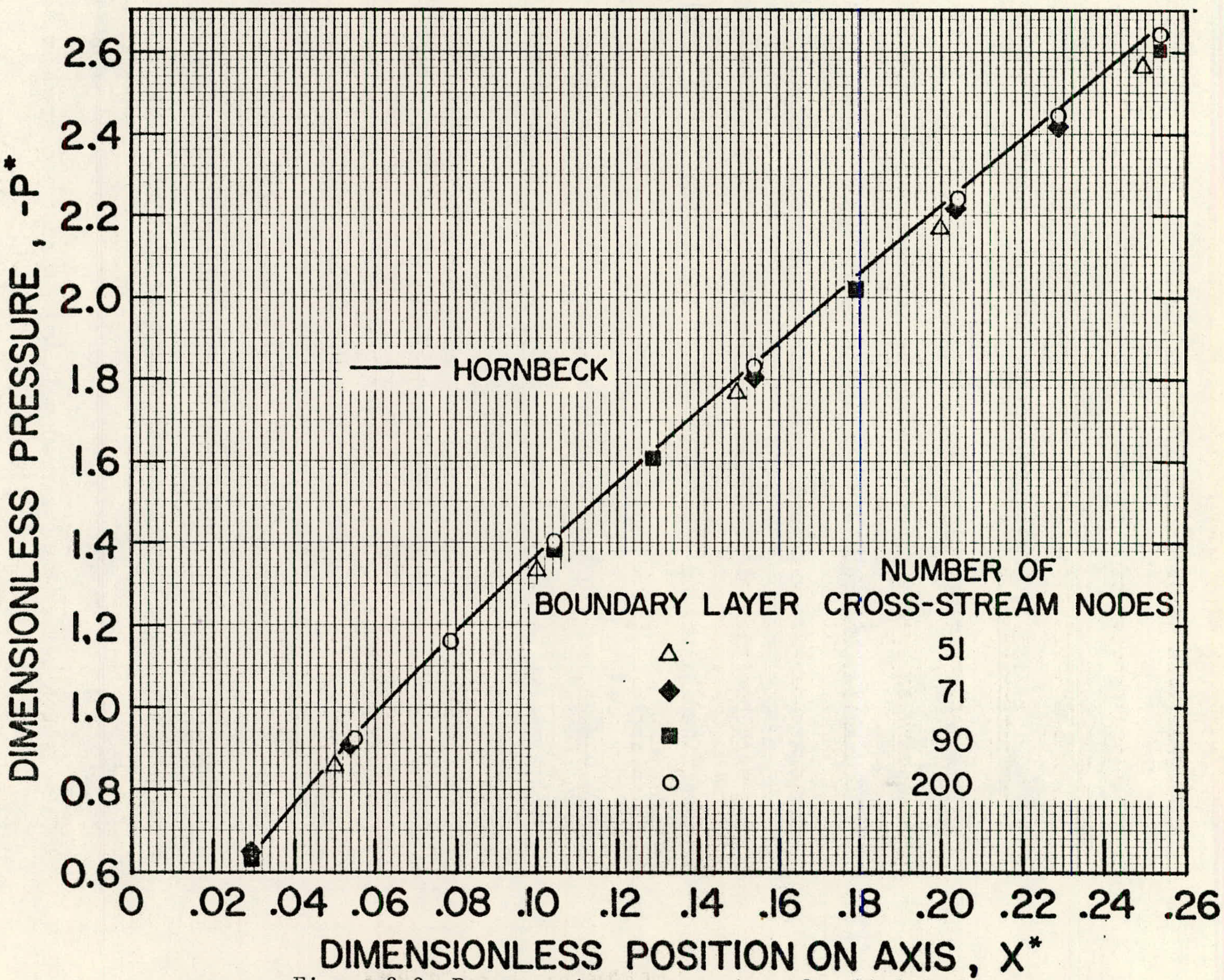

Figure 3.3 Pressure in entry region of cylindrical pipe.

The check verified that the program BNDARL produces values which are consistent with those produced by other calculations for a well-known situation.

3.2.4 Geometry of the Test Nozzle

In order to calculate the flow in the test nozzle, it is necessary to specify the shape of the nozzle. Due to machining inaccuracies, the nozzle was found to exhibit some asymmetries, but a method was devised for assigning an average value of radius for each position along the axis. The shape of the nozzle was determined by making a plastic mold of the inside of the nozzle. The plastic, Rigidax compound is produced by Argueso and Co., Inc. (Mamaroneck, NY 10543) for this kind of use. The model was examined with an optical comparator at magnifications of 20X and 100X. The nozzle was found to have a nearly conical entrance region and a short throat at the exit. The characterization of the nearly conical entrance region was straightforward. However, the critical region near the exit required more careful examination. Nine tracings of the exit region were made at a magnification of 100X as the model was rotated by approximately 20° between tracings. Measurements were made of the overall length of the model using the micrometer table on the optical comparator. This length measurement agreed well with direct measurement done on the nozzle itself, and supported confidence in the accuracy of the model. In addition, a #58 drill bit was found to slide into the exit region of the nozzle. The diameter of this drill was measured to be 1.06 mm.

The tracings of the throat region were superimposed and found to be nearly congruent in the conical section leading into the throat and at the farthest extremity of the throat. Figure 3.4 shows the superposition of the nine tracings which have been aligned using the section leading into the throat.

The characterization of the throat region is based upon the congruence of the tracings in the section leading into the throat, the congruence of the tracings at the farthest extremity of the throat and the radius of the drill #58. An axis was drawn bisecting the angle formed by the congruent lines, and the farthest extremity of the throat was assigned an axial position of $x = 1.770$ cm, which agrees well with overall length measurements made on the nozzle. The congruent lines leading into the throat section were then found to have the formula $R = -.311x + .584$. A line perpendicular to the axis was constructed through $x = 1.770$ cm, and the distances corresponding to $R = .053$ cm were marked off. These points represent the radius of the nozzle at the exit which was determined from the drill bit. Figure 3.4 shows rounding of the model near the radius of the exit. This is assumed to be due to loss of plastic when the model was extracted from the nozzle.

The nine tracings result in eighteen characterizations, each consisting of the line $R = -.311x + .584$, a point (R_i, x_i) where the throat begins and a line from (R_i, x_i) to the point $x = 1.770$, $R = .053$ where the throat ends. The points (R_i, x_i) were grouped into nine groups for convenience and an average of the eighteen

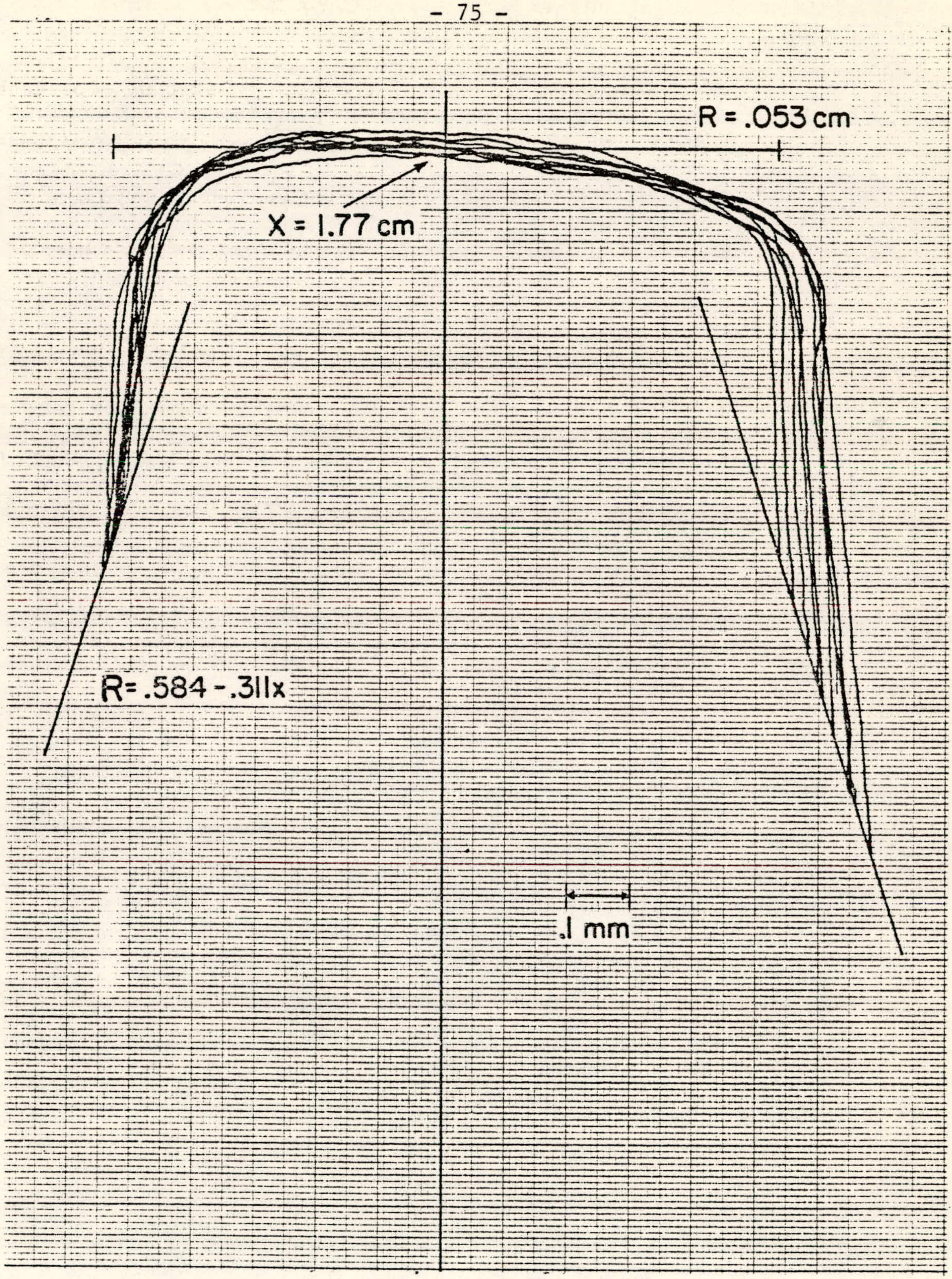

Figure 3.4 Exit region of the test nozzle.

radii was taken at each of the nine positions. For each characterization, the radius R at a position x is determined either by the line $R = -.311x + .584$ or by the line connecting (R_i, x_i) with (.053, 1.770) depending on whether x is greater or less than x_i.

In addition, the smaller magnification tracing revealed a position where the angle of the cone changed slightly: x = 1.580, R = .0922. Therefore, the characterization of nozzle consists of eleven points and straight line segments connecting the points which provide an axi-symmetric outline. Figure 3.5 illustrates the result near the exit. Table 3.1 lists the points.

Table 3.1 Points defining outline of axi-symmetric characterization of test nozzle

x, cm	R, cm
0	.527
1.580	.0922
1.661	.0670
1.670	.0644
1.677	.0625
1.684	.0606
1.691	.0589
1.701	.0566
1.706	.0559
1.712	.0552
1.770	.0530

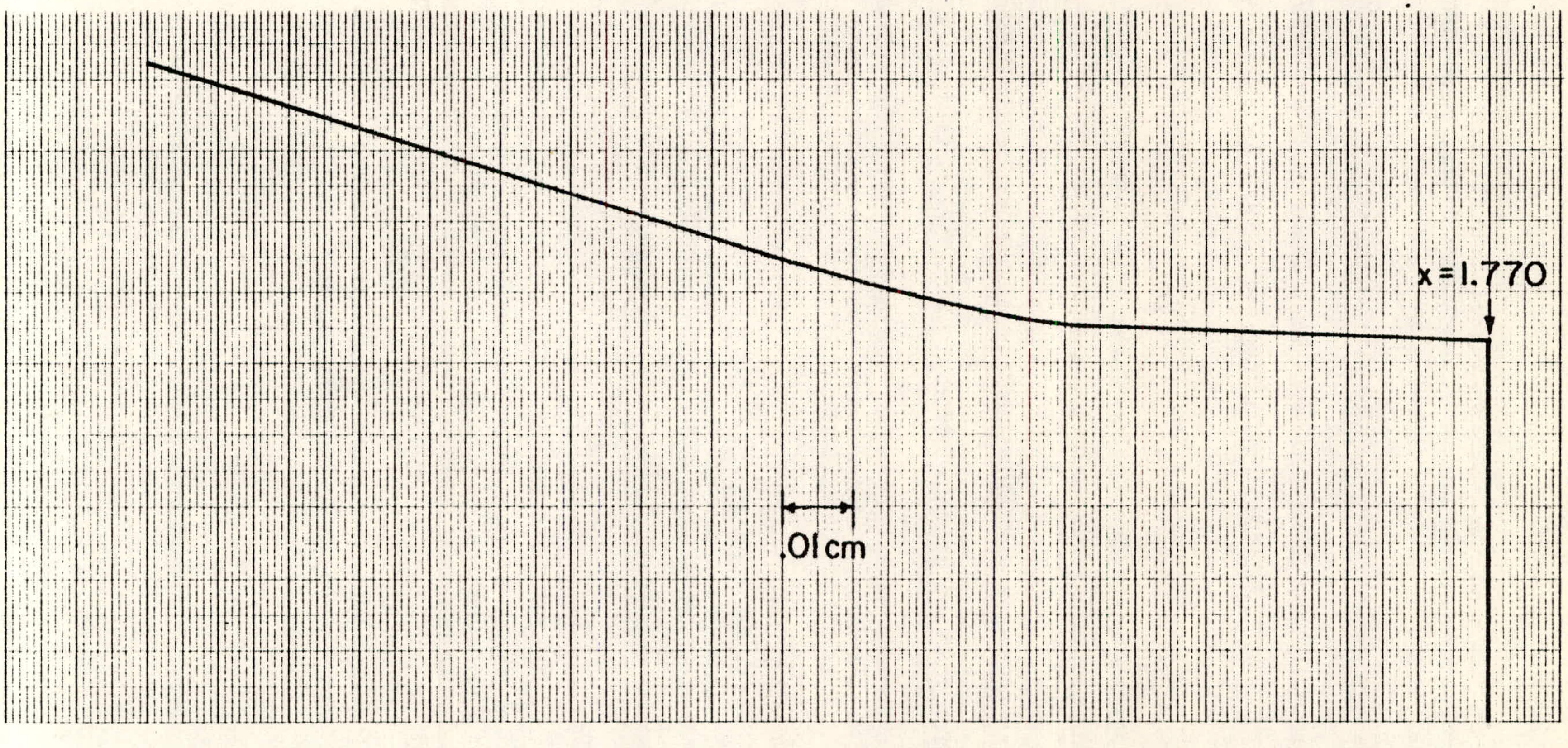

Figure 3.5 Characterization of exit region of the test nozzle.

3.2.5 Calculation of Flow in the Test Nozzle

In addition to the geometry specified in the last section, the flow program requires that the number of cross-stream nodes and maximum down-stream step size be set. Also necessary are the fluid properties and the velocity profile at the entrance to the nozzle. Finally, it is necessary to decide how to relate a theoretical flow to one observed in the experiment.

The fluid properties were specified as .001185 g/cm^3 for density and 188 x 10^{-6} poise for viscostiy. These values correspond to a temperature of 26°C and an inlet gas pressure of 1.015 x 10^6 $dynes/cm^2$ or 76.2 cm of Hg. The values were interpolated from values given in the Handbook of Chemistry and Physics (Weast, 1975, p. f-11, p. f-58).

The solution method was checked for sensitivity to number of cross-stream nodes as in Section 3.2.3. Ninety-one cross-stream nodes were chosen for the final calculations as further increase seemed uneconomical. Table 3.2 shows centerline gas velocity at the exit of the nozzle, U_e, pressure drop across the nozzle, ΔP, and the number of nodes used in each calculation. The entrance velocity for these calculations had a parabolic profile in r and a centerline velocity of 83.6 cm/s. The nodes were distributed uniformly in ω.

A similar test was done on maximum down-stream step size, using ninety-one cross-stream nodes and the same inlet flow as in the above test. Table 3.3 shows the results. R is the radius of the nozzle and depends upon position on the axis.

Table 3.2 Effect of number of cross-stream nodes on calculation of flow in the test nozzle

Number of Cross-stream Nodes	U_e cm/s	ΔP cm of H_2O
91	4585	12.76
50	4559	12.56
20	4470	12.07

Table 3.3 Effect of largest down-stream step size on calculations of flow in a test nozzle

Largest Down-stream Step Size	U_e cm/s	ΔP cm of H_2O
.01R	4585	12.76
.05R	4587	12.60
.1 R	4594	12.49

In the final flow calculations, the largest down-stream step size was limited to .01R.

Tests were also done to determine the effect of the shape of the inlet velocity profile on the velocity of particles leaving the nozzle. Flat and parabolic entrance profiles were used to generate flows with $\Delta P = 2.54$ and 25.4 cm of H_2O. Particle velocities were then calculated for the flat and parabolic cases for each value of ΔP. The particle velocities at the exit of the nozzle for the two entrance conditions were found to agree to four significant figures for both values of ΔP. The choice between flat and parabolic profiles was found to be insignificant and parabolic entrance profiles were used throughout the theoretical work.

The final question to be resolved before the flows could be calculated concerns the method of relating a theoretical to an experimental flow. Pressure drop across the nozzle is quite sensitive to changes in velocity and was the most accurately determined flow parameter in the experiment. Therefore, in the calculation, inlet velocities were varied until the calculated pressure drop fell within .5% of the measured pressure drop. The results of the calculation producing this agreement were stored for use in the particle velocity calculations. The program solved the flow field in approximately 80 seconds of central processor time and required 932 down-stream steps.

3.2.6 Results of the Flow Calculations

Flow calculations were done for each of six values of pressure drop across the nozzle. In each case, thirty-three values of centerline velocity, the corresponding axial coordinate and pressure were stored in a file for later use. A listing of these files is found in Appendix B.3. Graphs of the centerline velocity as a function of position are plotted in Figures 3.6 and 3.7, along with the outline of the nozzle. Figure 3.8 shows velocity profiles at four points along the axis for two values of ΔP.

Figures 3.6 and 3.7 reveal curves which are very similar in shape, a fact to be considered in the next section. In addition, it is clear that most of the velocity change occurs near the end of the nozzle; hence, it is not surprising that inlet velocity

3.6

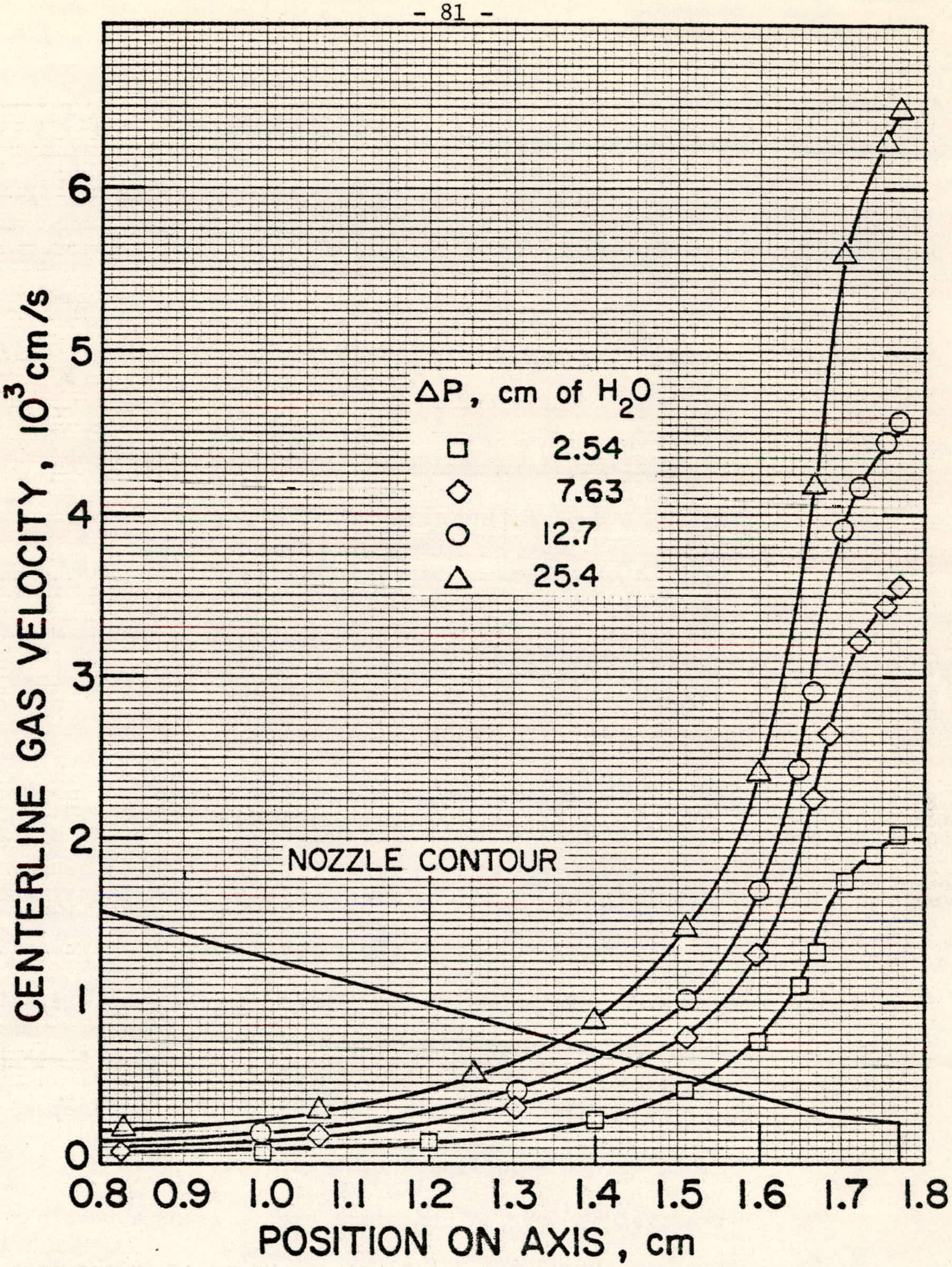

Figure 3.6 Centerline gas velocity in the test nozzle.

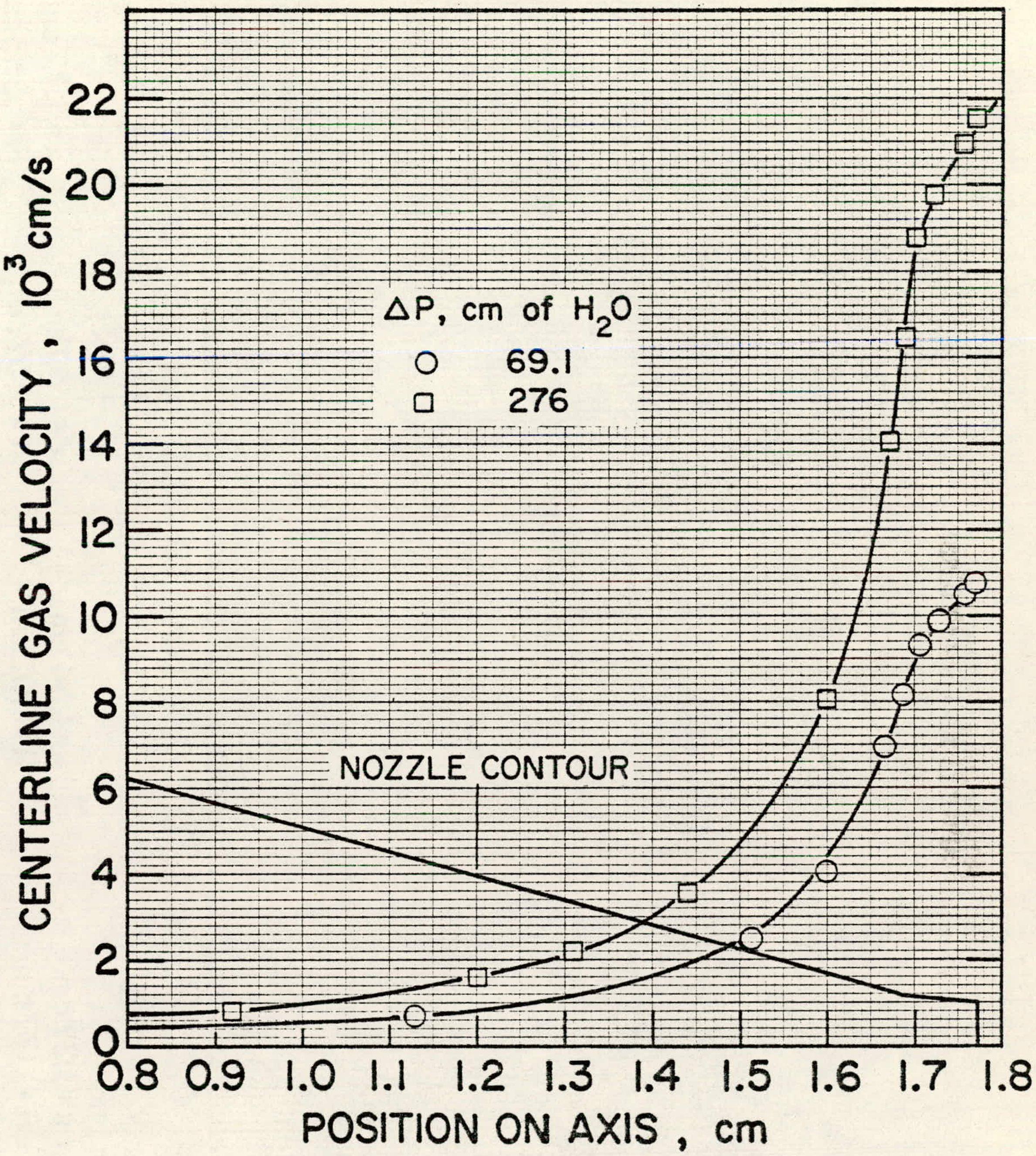

Figure 3.7 Centerline gas velocity in the test nozzle.

3.8

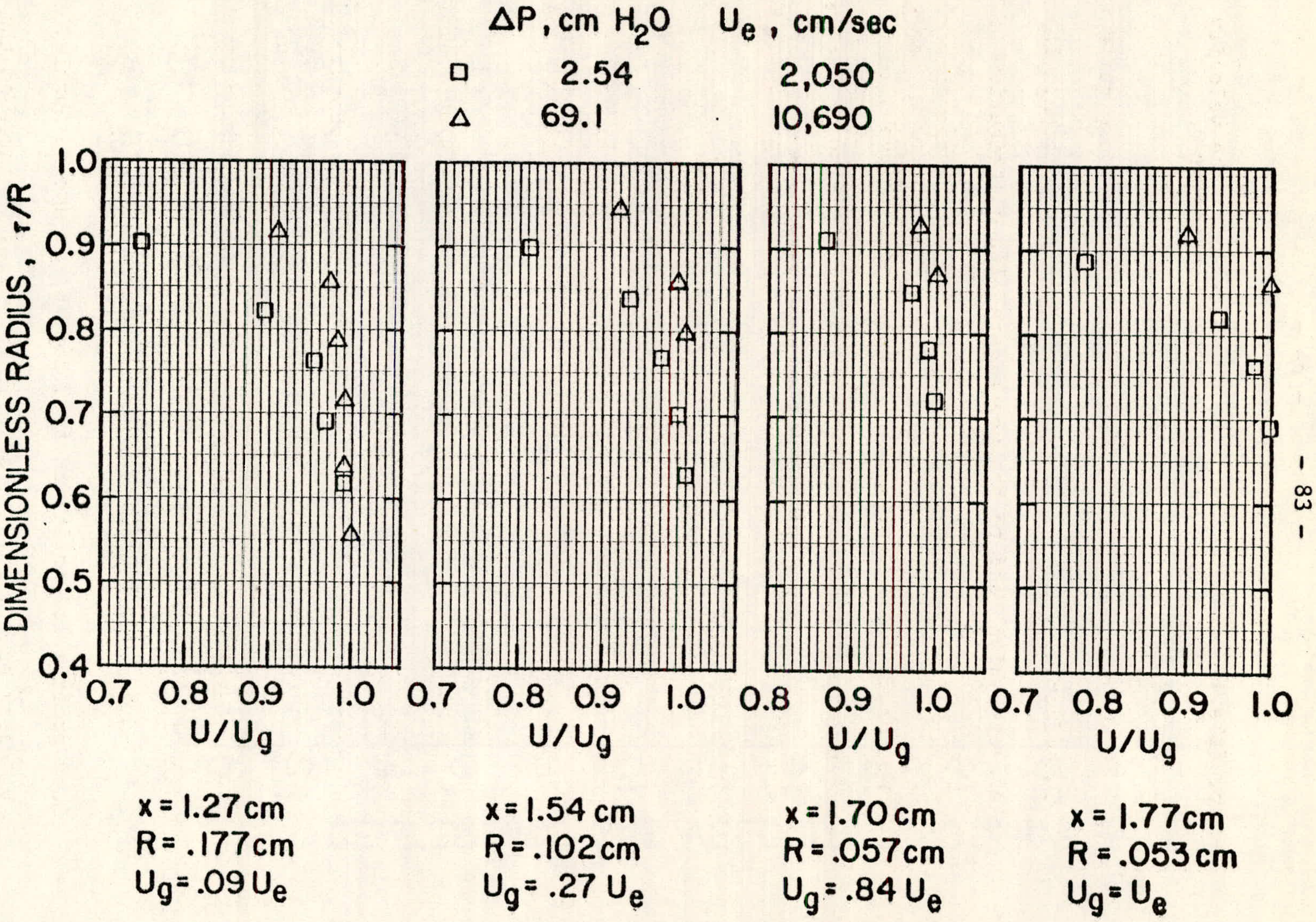

Figure 3.8 Velocity profiles in the test nozzle.

profile is not very important in determining the velocity of particles at the nozzle exit.

The velocity profiles shown in Figure 3.8 are quite flat. This fact will also be taken up in the next section. The viscous effects which tend to produce a parabolic distribution of velocity along the radial direction are counteracted by the convergence of the nozzle which flattens the flow. The relative size of the flat portion of the curve actually increases slightly as one moves down the axis until the throat is entered, at which point the flow again begins to develop a more rounded profile. It is clear that aerosol could occupy more than the center 10% of the flow without showing significantly different particle velocities at the exit.

3.3 Comparison of Boundary Layer Calculations with Calculations of Inviscid, Incompressible, Plug Flow

The similarity in shape of the curves in Figures 3.6 and 3.7 and the flatness of the velocity profiles shown in Figure 3.8 suggest that additional simplifying assumptions concerning the flow might be made. In this section, the predictions of inviscid, incompressible plug flow will be compared with those of the boundary layer theory.

Under the assumptions of incompressible plug flow, the velocity profile is considered flat across the entire nozzle, and the velocity at any given cross-section times the area of the cross-section gives the volumetric flow through the nozzle. Thus, given the velocity at any point in the nozzle, it is possible to predict the velocity at all other points in the nozzle by conservation of mass, i.e., the product of velocity and area is a constant.

The assumption of inviscid flow allows the application of Bernouli's Law to the flow, by which one can relate the volumetric flow of the fluid through the nozzle, Q, to the pressure drop, ΔP, across the nozzle,

$$\Delta P = \frac{1}{2} \rho Q^2 \left(\frac{1}{A_E^{\,2}} - \frac{1}{A_I^{\,2}} \right) \qquad (3.12)$$

where A_E is the area of the nozzle exit and A_I, the area of the entrance.

The assumption of incompressible, inviscid plug flow (hereafter referred to as one-dimensional ideal flow) is compared to the boundary layer approximation to see if the two agree on total flow, velocity of the gas on the centerline at the exit of the nozzle and dependence of centerline gas velocity on axial position.

In Table 3.4, experimental values of Q have been included for reference with those predicted by ideal flow and boundary layer. All values of Q are for P = 76.2 cm of Hg. Centerline velocities at the exit predicted by boundary layer are tabulated with the exit velocities predicted by ideal flow. Figure 3.9 shows the dependence of centerline velocity on the axial position as predicted by boundary layer and by the plug flow assumption. The dimensionless velocity is the centerline velocity, U_g, divided by the centerline velocity at the exit, U_e.

A significant disagreement concerning total flow exists between the boundary layer and ideal flow calculations. The percent discrepancy decreases with increasing flow Reynolds number, Re_f.

3.9

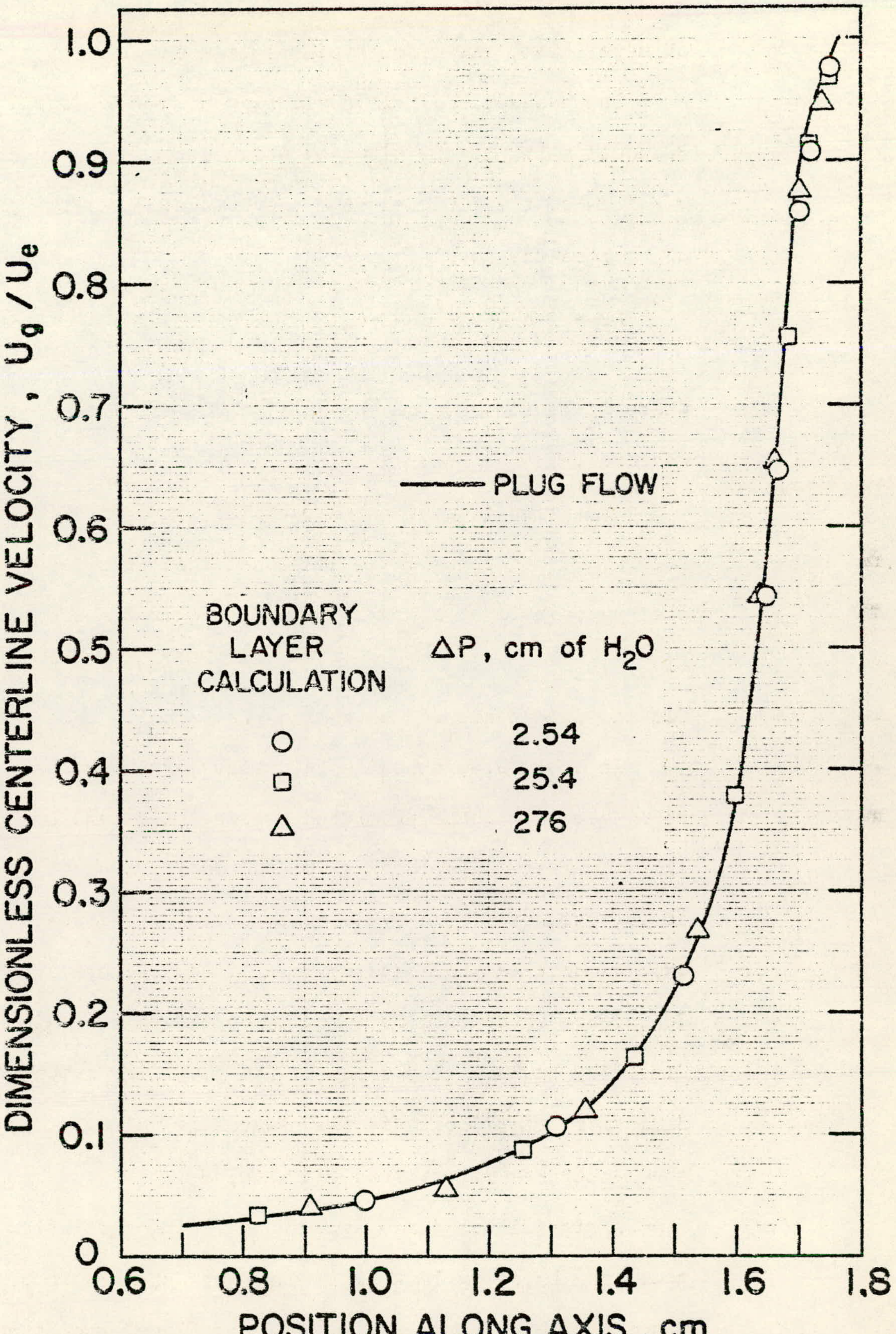

Figure 3.9 Centerline gas velocity by boundary layer and plug-flow assumptions.

Table 3.4 Comparison of boundary layer and inviscid incompressible plug flows in the test nozzle

ΔP cm of H_2O	Flow Rate, lpm			Exit Centerline Velocity, cm/s	
	Measured	Theoretical Boundary Layer Calculation	Bernouli's Law	Boundary Layer Calculation	Bernouli's Law
2.54	1.02	.94	1.09	2054	2050
7.63	1.77	1.69	1.89	3557	3553
12.7	2.31	2.21	2.43	4585	4584
25.4	3.25	3.2	3.4	6480	6482
69.1	5.2	5.3	5.7	10690	10692
276	9.7	10.9	11.4	21380	21370

The ratio of total flow predicted by the boundary layer to that predicted by ideal flow increases from .85 when $Re_f = 12 \times 10^2$ ($\Delta P = 2.54$ cm of H_2O) to .96 where $Re_f = 14 \times 10^3$ ($\Delta P = 276$ cm of H_2O). This illustrates the expected effect of viscosity. The energy dissipated by viscous effects results in lower flow rates for a given ΔP than would be expected for inviscid flow. This energy is lost in the region near the wall where the velocity gradients are largest and there is development of a flow profile. The velocity predicted by boundary layer in the center region of the flow exceeds the mean velocity. It turns out that these effects balance and the centerline velocity predicted by the boundary layer theory agrees well with the velocity predicted by ideal flow. This is true of both the exit velocities tabulated in Table 4.3 and the velocity as function of position shown on Figure 3.9. The two models agree on the values which are critical to this study, i.e., prediction of centerline velocity as a function of position on the axis from the pressure drop.

3.4 Calculation of Particle Trajectories

3.4.1 Equations to be Solved

The equations for spherical particles moving in a fluid are given for the one-dimensional case [Equations (3.13) and (3.14)]. Due to the flatness of the theoretical velocity profile and the use of sheath air to confine the aerosol in a region around the center streamline, it is necessary only to solve for the particle motion along the center streamline. The narrowness of the measured particle velocity distributions supports this view.

The equations of motion of the particle are:

$$\frac{dU_p}{dx} = \frac{3\pi\mu(U_g-U_p)D_p}{C\ M\ U_p} \qquad (Re_p < .5) \qquad (3.13)$$

$$\frac{dU_p}{dx} = \frac{3\quad(U_g-U_p)D_p}{C\ M\ U_p} + \frac{D_p^{5/3\ 2/3\ 1/3}(U_g-U_p)^{5/3}}{2C\ M\ U_p} \qquad (Re_p \geq .5) \qquad (3.14)$$

where D_p is the particle diameter, U_g, the gas velocity, U_p, the particle velocity, M, the particle mass, μ, the gas viscosity, and ρ, the gas density. Re_p, the particle Reynolds number, and C, the slip correction, are given in Equations (3.15) and (3.16). The formula for C is adapted from Liu (1972).

$$Re_p = \frac{\rho D_p(U_g-U_p)}{\mu} \qquad (3.15)$$

$$C = 1 + \frac{16.5}{D_pP} + \frac{5.5}{D_pP} \exp\ (-0.65\ D_pP) \qquad (3.16)$$

where P is the air pressure. Although the flow is solved for the incompressible case, changes in gas density enter into the particle dynamics through Equation (3.16).

Equation (3.13) is merely Stokes' law and expresses the fact that at low Reynolds number, the drag coefficient of a sphere is $24/Re_p$. Equation (3.14) is an extension of Stokes' law to be used at higher Reynolds numbers. It was proposed by Klyachko (see Fuchs, 1964, p. 33). This equation results from an empirical fit to drag coefficient data, and is equivalent to $C_D = 24/Re_p + 4/(Re_p)^{1/3}$. The transition point from Equation (3.13) to Equation (3.14) is somewhat arbitrary. Figure 3.10

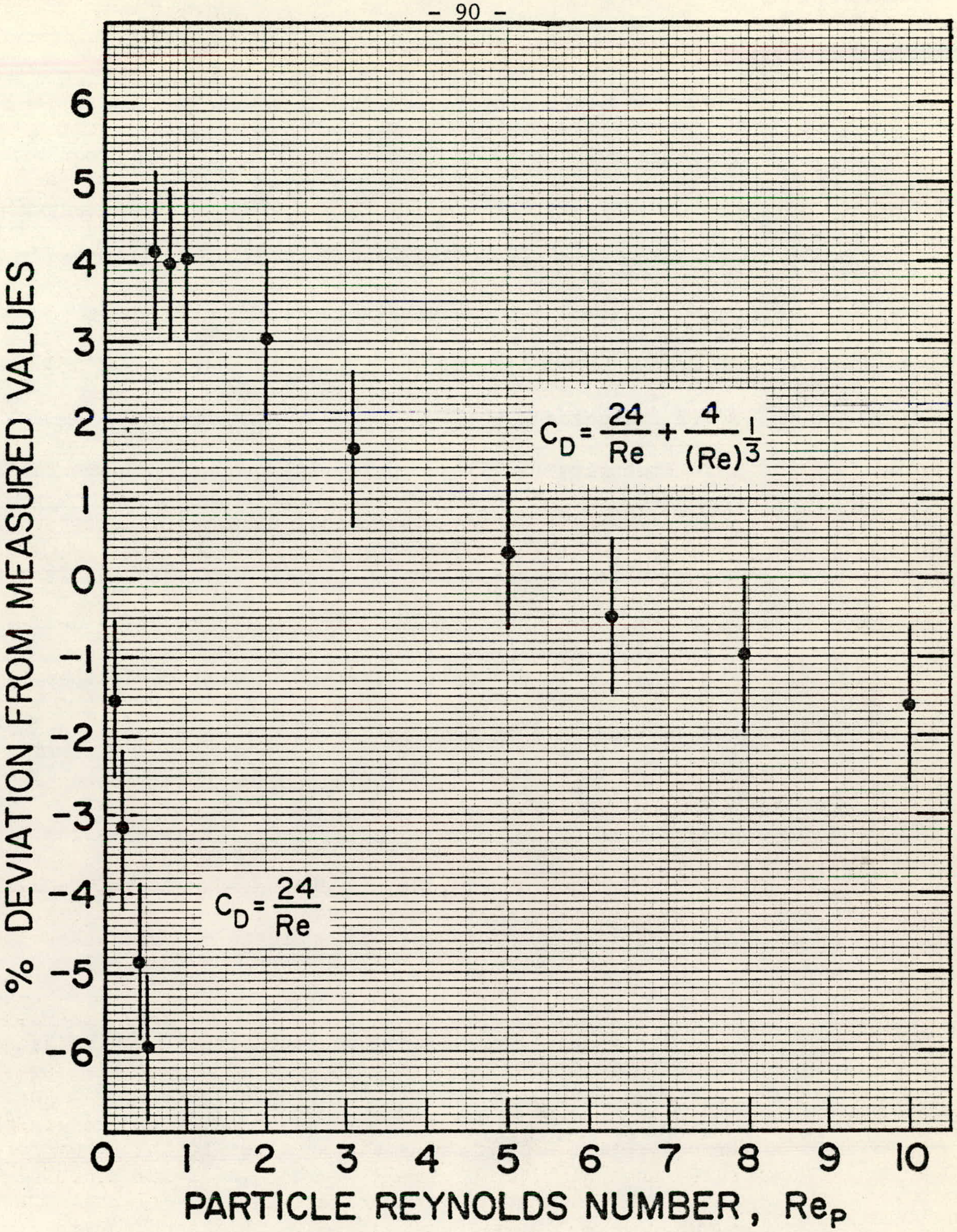

Figure 3.10 Deviation of calculated drag coefficients from measured values.

shows the percent deviation from measured values of the drag coefficients calculated by (3.13) and (3.14). The error bars show the probable error cited by Fuchs. The percent discrepancy between the formulas and the measured values has approximately the same magnitude but opposite sign at $Re_p = .5$ where the transition between Equation (3.13) and (3.14) is made.

3.4.2 Solution Method

Equations (3.13) and/or (3.14) are solved numerically using a Runge-Kutta solution subroutine. The gas velocity and pressure are supplied as a function of position on the axis from the boundary layer flow calculations. The particle diameter and density are supplied by the user. The solution proceeds step-by-step down the axis using P to calculate C [Equation (3.16)], and finding U_p for each step. The Runge-Kutta routine requires that dU_p/dx be supplied in order to integrate for U_p. Each time the Runge-Kutta routine demands dU_p/dx, Re_p is evaluated. If Re_p is less than .5, Equation (3.14) is used to evaluate dU_p/dx; otherwise, Equation (3.14) is used.

The Runge-Kutta library routine, programmed by Frisch and Hotchkiss (1965), has variable integration step size and automatic error control. The user assigns values to the error parameters, ETA and EPS. These parameters are used as follows: the routine integrates between two points, x_1 and x_2, and produces a value of U_p at x_2. Then the interval is halved and the integration is done between x_1 and $(x_1 + x_2)/2$, and then from $(x_1 + x_2)/2$ to x_2. The second two-step integration produces U_p'. If $|U_p - U_p'| < EPS \times U_p$, or if $|U_p - U_p'| < \text{ETA}$, the routine continues on to x_3. If the criteria are not met, the interval is halved and reintegrated.

Clearly, the Runge-Kutta routine with variable step size requires that a value for dU_p/dx be available for any value of x. However, the information supplied from the flow calculations consists of gas velocity and pressure at thirty-three points on the axis of the nozzle. A library routine using Aitken's method was used to interpolate between these points when the Runge-Kutta routine required intermediate values of U_g (Skow and Hotchkiss, 1972). Three points were used in the interpolations. The thirty-three supplied values of P were used to calculate C, since P changes slowly.

The main solution program, named PARVEL, is listed in Appendix C with a glossary of those terms which are modified by the user.

3.4.3 Test of the Solution Method

The particle velocity program was tested in the case of a particle with a small initial velocity in a flow of larger constant velocity. Stokes' law was used. The equations were non-dimensionalized and solved numerically. An analytic solution was used for comparison, and the two agree to four significant figures for values of EPS less than 10^{-2}.

3.4.4 Calculations of Particle Trajectories in the Test Nozzle

The particle trajectory program requires that particle density and diameter be specified, gas velocities and pressures be supplied, and values be assigned to EPA and ETA. In addition, some accounting must be made for the fact that in the experiment, the measurement of particle velocity is made some distance from the end of the nozzle.

The error criteria, EPS and ETA, which control the step size in the integration routine, were set at 10^{-5}. The test and some preliminary calculations indicated that this is a safe value. Resulting integration step sizes and time required for solution of the equation depended primarily on particle lag. Those particles with velocities closest to that of the gas required smaller steps and longer computing times. CP times ranged from less than two seconds for 11.3 μm particles in the largest flow to 60 seconds for .5 μm particles in the smallest flow. The corresponding step sizes were on the order of .03 cm and .001 cm, respectively.

In the experiment, particles traveled some 145 μm ± 15 μm from the exit of the nozzle to the center of the measurement region. The theoretical treatment of this fact consists of continuing the integration to the measuring point, assuming that the gas velocity remains unchanged over this distance, which corresponds to approximately .13 of the nozzle exit diameter.

Velocities have been calculated for particles of density 1.05 g/cm^3 with diameters .5, .15, 1, and 2 μm for comparison with measurements made on PSL aerosol. Calculations for particles of density .886 g/cm^3 and diameters 3, 6, 9, and 11.3 μm provide theoretical comparison for the measurements made on oleic acid particles.

3.4.5 Results of Calculations and Comparison with Experiments

Figures 3.11, 3.12, and 3.13 present graphically the results of the theoretical calculations and measurements of particle velocity 145 μm from the exit of the nozzle.

The deviation of the experimental points from the theoretical curves is rather small. Considering only deviation in the velocity coordinate, the percent mean deviation is on the order of 1.4% for $\Delta P = 2.54$ cm of H_2O, 2.2% for $\Delta P = 12.7$ cm of H_2O, and 1.1% for $\Delta P = 61.9$ cm of H_2O. A mean deviation of only 3% for $\Delta P = 276$ cm of H_2O is surprising since the incompressible flow assumption should begin to fail at this large pressure drop.

The good agreement between theory and experiment must be understood as a verification of the model in the range of values tested. The boundary layer flow calculation produced centerline gas velocities at the exit which were very close to the velocities of the .5 μm diameter particles in the cases where the particle velocity curves become flat for small D_p. The flattening of these curves (see $\Delta P = 2.54$, 7.63, 12.7 cm of H_2O) indicates that the particles are traveling at velocities very near that of the gas, and these measurements tend to confirm the centerline exit velocity predicted by the boundary layer theory.

The remainder of the velocity measurements confirm the particle dynamics model as well. This method of theoretical analysis can be used with confidence to predict the velocity of particles confined near the center streamline in incompressible flows in nozzles of moderate convergence.

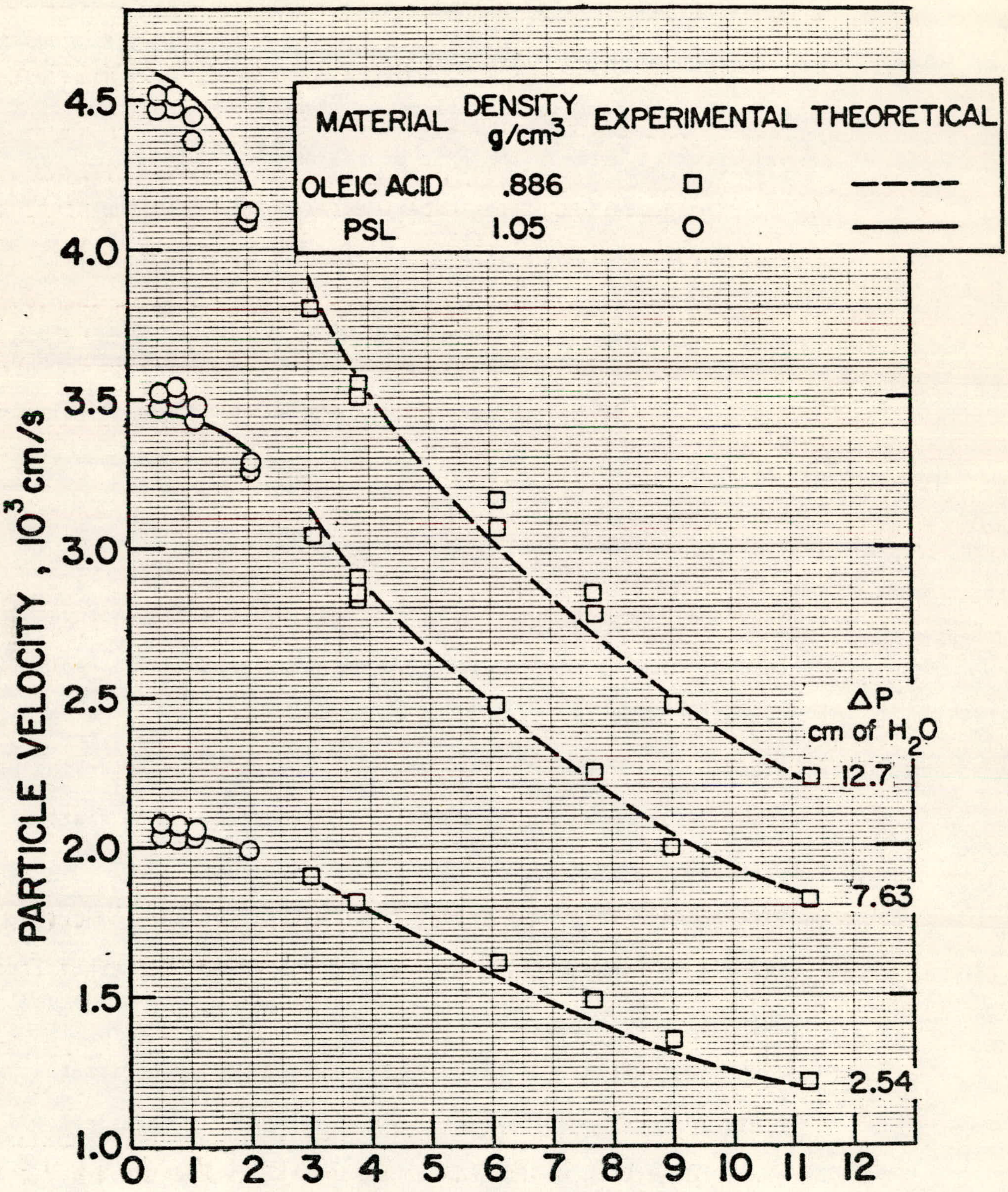

Figure 3.11 Experimental and theoretical particle velocities for test nozzle.

2

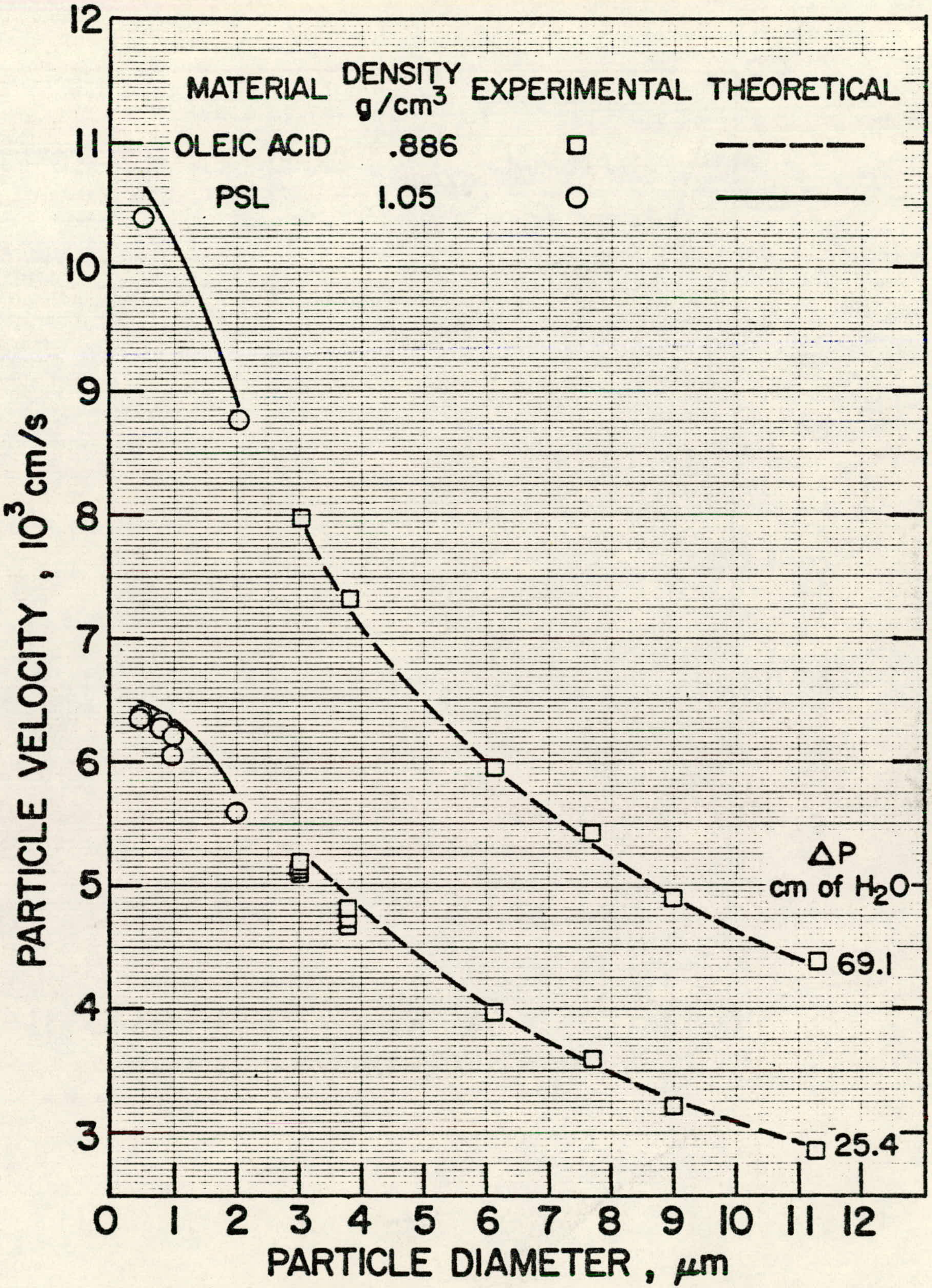

Figure 3.12 Experimental and theoretical particle velocities for test nozzle.

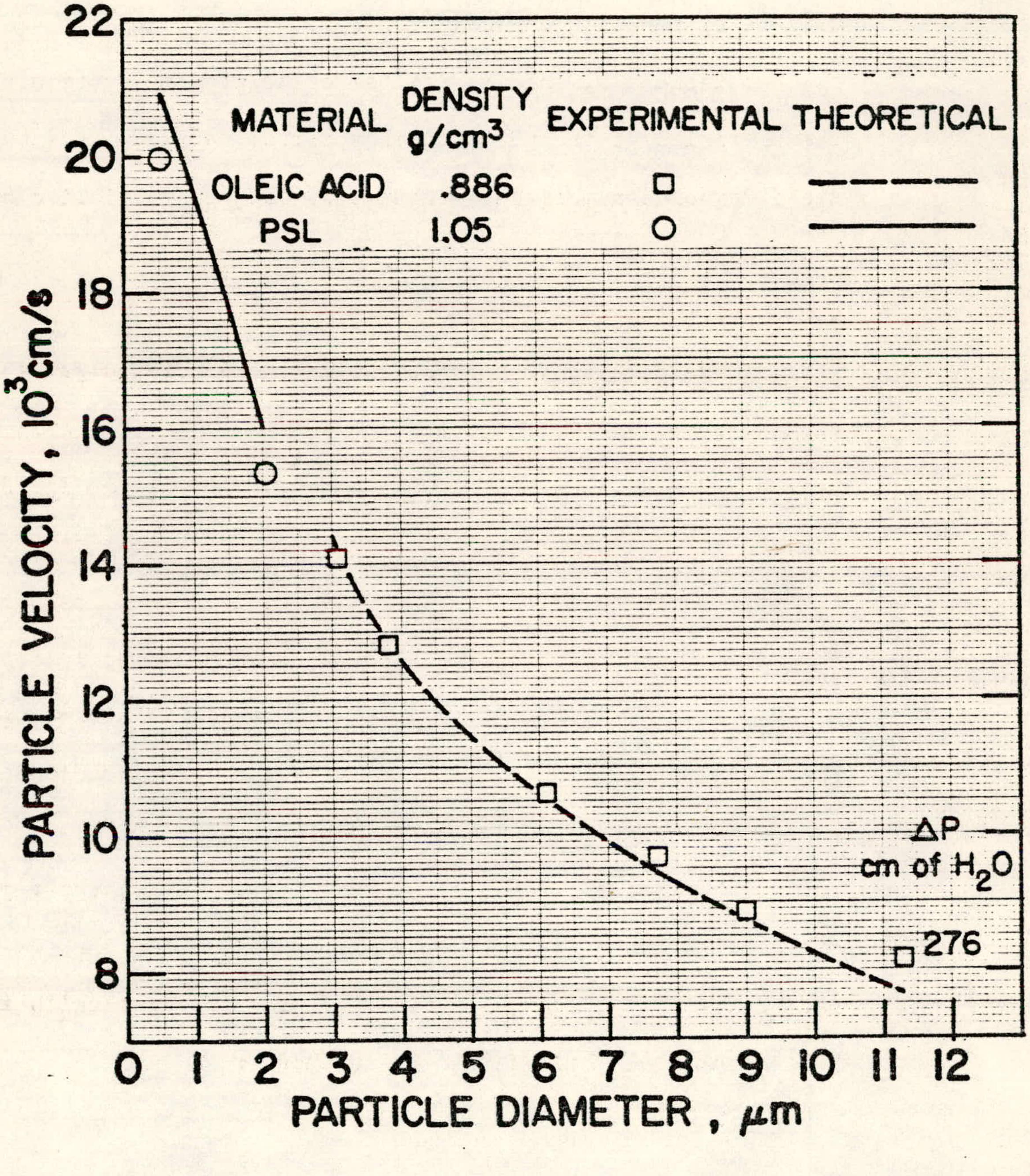

Figure 3.13 Experimental and theoretical particle velocities for test nozzle.

The use of Bernouli's Law to predict particle velocities will be examined in the next chapter.

In Table 3.5, the theoretical calculated velocities, U_p, of the particles at the point of measurement, dU_p/dx, and the particle Reynolds numbers are tabulated. dU_p/dx multiplied by the uncertainty in the measurement position is not large enough to account for the deviations.

Figure 3.14 shows the theoretically calculated gas and particle velocities as a function of position along the axis for the case of $\Delta P = 25.4$ cm of H_2O and two particle sizes. The fact that the slope of the gas velocity is greater than that of the particle velocity indicates that the particle Reynolds number, Re_p, is increasing throughout the trajectory in the nozzle.

As was noted in Section 3.4.1, C was allowed to change as P changed, even though the flow was calculated for the incompressible case. The actual variation in C is small. It will, of course, be greatest for small particle sizes and largest pressure drops. Table 3.6 indicates the increase in C for the smallest particle sizes and largest values of pressure drop calculated. This result will be referred to in Chapter 4.

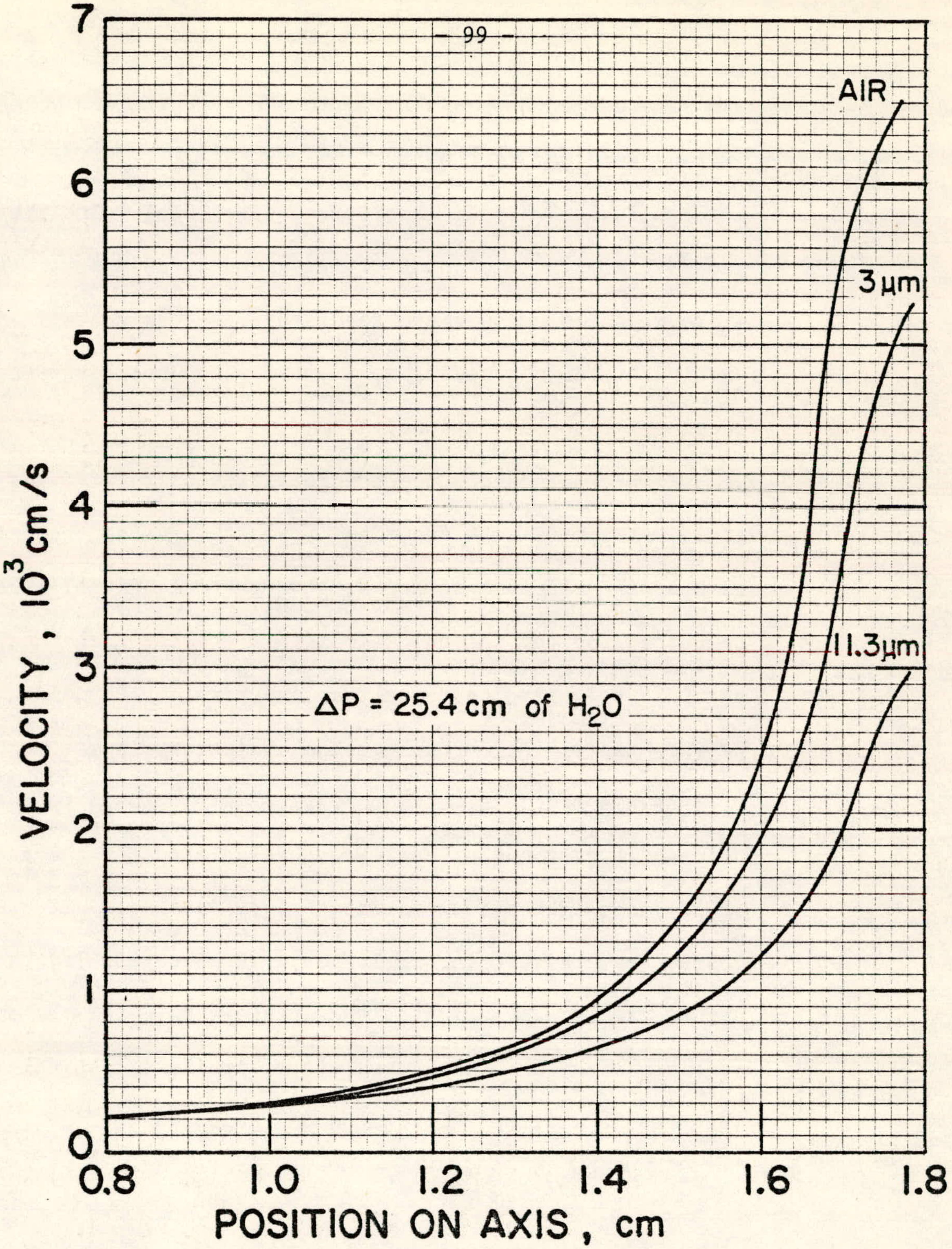

Figure 3.14 Theoretical gas and particle velocities along axis of test nozzle, $\Delta P = 25.4$ cm of H_2O.

Table 3.5 Theoretical values of U_p and dU_p/dx at 145 μm beyond the exit of the nozzle

	$\Delta P = 2.54$ $U_e = 2054$		$\Delta P = 7.63$ $U_e = 3557$		$\Delta P = 12.7$ $U_e = 4585$		$\Delta P = 25.4$ $U_e = 6491$		$\Delta P = 69.1$ $U_e = 10710$		$\Delta P = 276$ $U_e = 21380$	
D_p, μm / ρ, g/cm^3	U_p cm/s	dU_p/dx $10^3 s^{-1}$	U_p cm/s	dU_p/dx $10^3 s^{-1}$	U_p cm/s	dU_p/dx $10^3 s^{-1}$	U_p cm/s	dU_p/dx $10^3 s^{-1}$	U_p cm/s	dU_p/dx $10^3 s^{-1}$	U_p cm/s	dU_p/dx $10^3 s^{-1}$
.5 /1.05	2054	0	3556	0	4583	.4	6482	1.2	10650	4.6	20940	18
.75/1.05	2053	.14	3550	.9	4574	1.3	6440	3.7				
1. /1.05	2050	.53	3532	2.0	4532	3.3	6352	6.0	10240	13	19400	32
2. /1.05	1991	2.4	3328	5.0	4221	7.0	5768	10.8	8934	19	16100	38
3. / .886	1904	3.1	3138	6.1	3920	8.1	5288	11.8	8079	19	14410	37
6. / .886	1574	3.9	2469	6.5	3034	8.1	4020	11	6034	17	1062	31
9. / .886	1322	3.6	2044	5.8	2501	7.2	3299	9.6	4934	15	8670	26
11.3 / .886	1181	3.4	1818	5.3	222	6.6	2928	8.8	4376	13	7688	24

Table 3.6 Change in C for smallest particles and largest values of ΔP

ΔP, cm H_2O	D_p, μm	% Increase in C
276	.5	11 %
276	1.	5 %
276	3.	2 %
69.1	.5	2 %
69.1	1.	1 %
69.1	3.	.3%
25.4	.5	1 %
25.4	1.	.3%
25.4	3.	.2%

CHAPTER 4

THEORETICAL ANALYSIS - IDEAL NOZZLES

4.1 Introduction

The work described in Chapter 3 demonstrates that it is possible to accurately predict the velocity of particles moving on the centerline of a nozzle. In this chapter, the equations of particle motion are written in dimensionless form and applied to the problem of particles moving in conical nozzles. These calculations are done assuming inviscid, incompressible plug flow in the nozzle. The use of these assumptions in place of the boundary layer approximation is justified by additional comparisons between the two methods in which the centerline velocities are found to agree.

A dimensionless particle velocity results from the numerical solution to the dimensionless equation of motion. This dimensionless velocity is a function of Stokes number, a particle Reynolds number, the geometry of the nozzle and the dimensionless position of the particle. The dimensionless particle velocities are shown in tables and graphs which allow particle velocities to be determined for various flows, nozzle geometrics, particle sizes and densities.

In the final section of the chapter, the relationship between particle velocity and aerodynamic particle size is explored. Understanding this relationship is essential in order to evaluate this technique as a method of sizing particles.

4.2 Dimensional Analysis of the Equations of Motion

This analysis follows that of Friedlander (1977). Equation (4.1) expresses the drag force experienced by a particle moving in the same direction as the fluid.

$$F_D = \frac{\pi\rho(U_g - U_p)^2 D_p^{\,2} C_D}{8C} \tag{4.1}$$

The drag coefficient, C_D, depends only upon Re_p. C is included in Equation (4.1) to account for the slip experienced by smaller particles.

Newton's second law for a particle experiencing only drag force can be written as:

$$F_D = \frac{\pi}{6} D_p^{\,3} \rho' U_p \frac{dU_p}{dx} \tag{4.2}$$

where ρ' is the density of the particle.

If Equations (4.1) and (4.2) are combined, the resulting equation can be non-dimensionalized to give:

$$\frac{dU_p^{\,*}}{dx^*} = \frac{3}{4} \frac{\rho\ (U_g^{\,*} - U_p^{\,*})^2\ a\ C_D}{\rho'(U_p^{\,*})\ C\ D_p} \tag{4.3}$$

where the following dimensionless quantities are defined as:

$$U_p^{\,*} = \frac{U_p}{U_e}$$

$$U_g^{\,*} = \frac{U_g}{U_e} \tag{4.4}$$

$$x^* = \frac{x}{a}$$

U_e is the centerline gas velocity at the exit of the nozzle, and a is the radius of the nozzle exit.

This result can be simplified by the introduction of Stokes and Reynolds numbers. For spherical particles,

$$St = \frac{D_p^{\,2}\rho' U_e C}{18\mu a} \tag{4.5}$$

$$Re = \frac{\rho U_e D_p}{\mu} \tag{4.6}$$

and

$$Re_p = (U_g^{\,*} - U_p^{\,*})\ Re \tag{4.7}$$

The dimensionless equation becomes:

$$\frac{dU_p^{\,*}}{dx^*} = \frac{Re(U_g^{\,*} - U_p^{\,*})^2 C_D}{24\ (St)\ U_p^{\,*}} \tag{4.8}$$

In order to solve this equation, both C_D and $U_g^{\,*}$ must be provided. C_D is known to depend only on Re_p, and the assumption of one-dimensional ideal flow implies that $U_g^{\,*}$ is a function of x^* and nozzle shape. Thus, $U_p^{\,*}$ is a function of x^*, Re, St and nozzle geometry.

4.3 One-Dimensional Ideal Flow in a Conical Nozzle

In order to simplify and standardize the specification of nozzle geometry, only conical nozzles are treated in this and the following sections. A cone of sufficient length will be specified to insure that the approach velocity is negligible. In such a nozzle, the gas velocity at the exit depends primarily upon the pressure drop and not significantly upon the length of the nozzle. The dimensionless gas velocity in the nozzle as a function of dimensionless distance from the exit is identical in all nozzles having the same cone angle.

Figure 4.1 shows the conical nozzle used in subsequent calculations. The dimensionless velocities calculated for particles in this nozzle may be applied to all nozzles having the same cone angle and equal or greater length. For one-dimensional, ideal flow, the pressure drop across the nozzle and the dimensionless gas velocity are given by:

$$\Delta P = \frac{U_e^{2}\rho}{2}\,(.992) \tag{4.9}$$

$$U_g^{*} = \frac{1}{(11 - x^{*}\tan\alpha)^{2}} \tag{4.10}$$

Nozzles described by Equations (4.9) and (4.10) will be referred to as ideal nozzles.

U_g^* is needed for calculations of U_p^* in nozzles with α = 15°, 30°, and 45°, but the accuracy of one-dimensional ideal flow has been established only for the α = 15° case in Chapter 3. Results shown in Table 4.1 and Figure 4.2 indicate that the values of centerline gas velocity and pressure drop across the nozzle predicted by one-dimensional ideal flow agree with those calculated using the boundary layer model for α = 30° and 45° as well. Unlike the values for α = 15°, those for α = 30° and 45° have not been checked experimentally. Table 4.1 gives the volumetric flows (P = 76.2 cm Hg) and exit velocities, and Figure 4.2

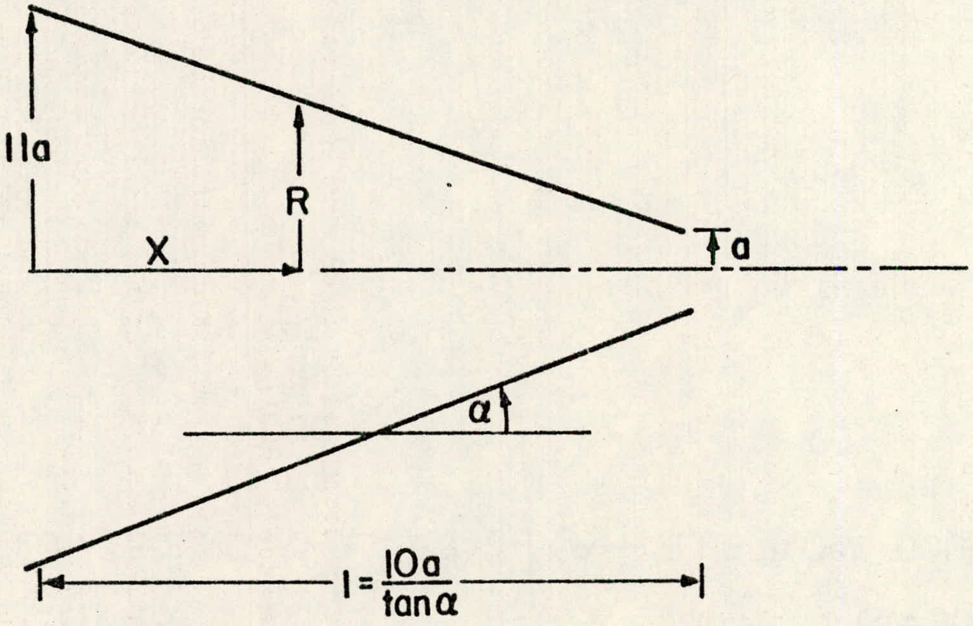

Figure 4.1 Geometry of the ideal nozzle.

4,2

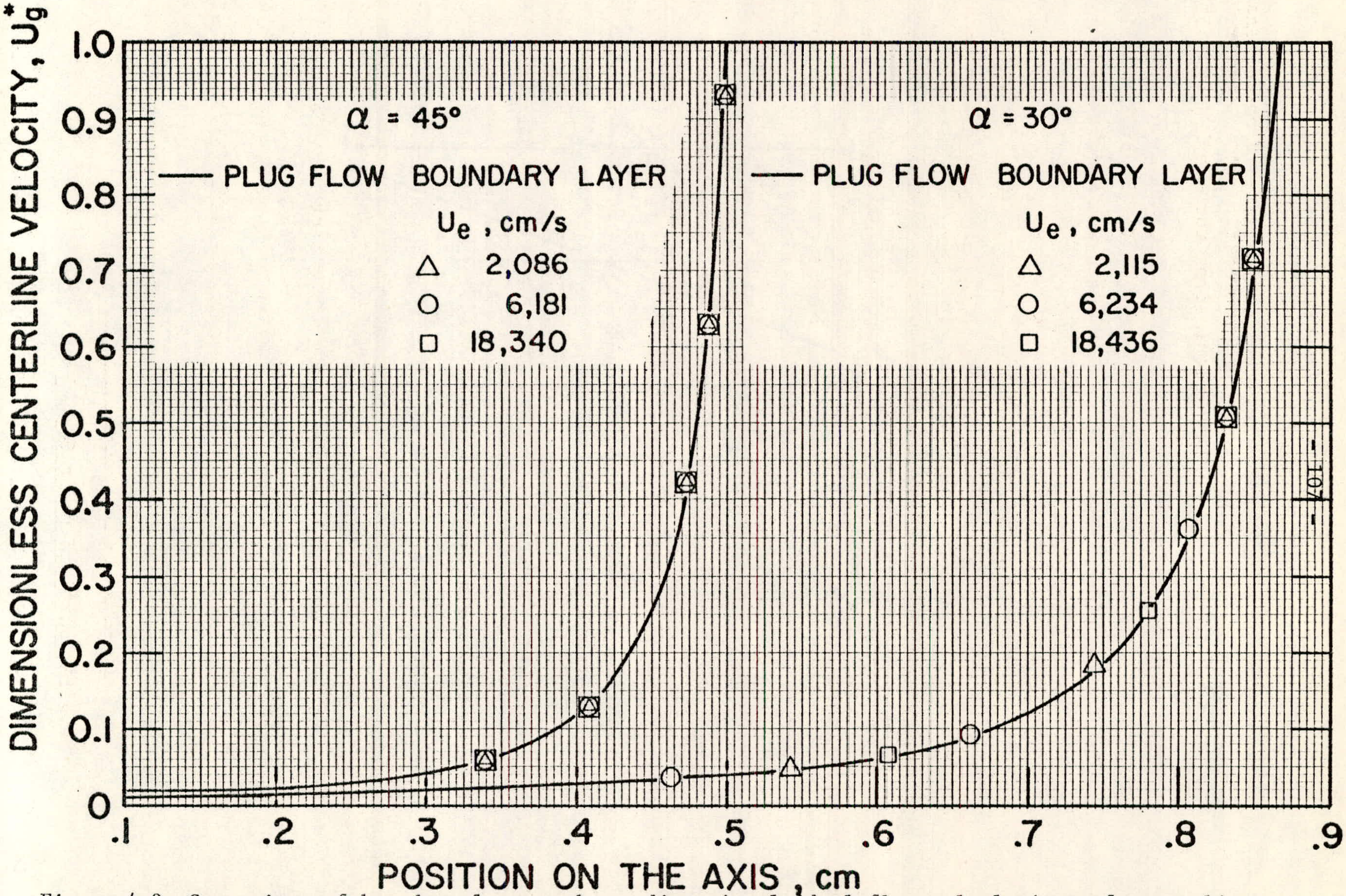

Figure 4.2 Comparison of boundary layer and one-dimensional ideal flow calculations of centerline gas velocities.

Table 4.1 Comparison of boundary layer and one-dimensional ideal flow calculations for α = 30° and 45°

		Boundary Layer		One-Dimensional Ideal Flow	
α	ΔP cm H_2O	Q lpm	U_e 10^3cm/s	Q lpm	U_e 10^3cm/s
30°	2.68	.94	2.12	1.00	2.12
30°	23.4	2.85	6.23	2.94	6.24
30°	204.	8.55	18.4	8.69	18.4
45°	2.60	.94	2.09	.98	2.08
45°	22.8	2.85	6.18	2.91	6.17
45°	201.	8.55	18.3	8.63	18.3

shows the centerline velocities predicted by the two methods. The flow Reynolds numbers range from 1300 to 11,600. In the one-dimensional ideal flow case, Bernouli's law, Equation (4.9), was applied to the pressure drop predicted by the boundary layer calculation to find U_e. Then Q was found by multiplying U_e by the area of the nozzle exit. The centerline gas velocities and pressures calculated by the boundary layer approximation are listed in Appendix B.3.2. The agreement of the two methods on U_g^* justifies the substitution of the one-dimensional ideal flow calculation for the other.

4.4 Particle Motion in Ideal Nozzles

4.4.1 Equations to be Solved

Equation (4.8) is to be solved for U_p^* where U_g^* is given by

Equation (4.10) and C_D is given below.

$$C_D = \frac{24}{Re_p} \quad ; \quad Re_p < .5 \tag{4.11}$$

$$C_D = \frac{24}{Rep} + \frac{4}{(Re_p)^{1/3}} \quad ; \quad Re_p \geq .5 \tag{4.12}$$

Equations (4.8), (4.11), and (4.12) express in dimensionless form the same information found in Equations (3.13) and (3.14).

4.4.2 Solution Method

Equations (4.8), (4.11), and (4.12) are solved numerically by methods similar to those described in Chapter 3 for the solution of Equations (3.13) and (3.14). However, two differences in the solution programs deserve mention. When solving Equations (3.13) and (3.14), the value of C was calculated for each value of pressure encountered along the particles' path. However, C is absorbed into St in the solution of Equation (4.6) and is thus constant. Table (3.6) shows the changes in C experienced in the actual calculations done for Chapter 3. If the pressure drop is kept small enough so that the assumption of incompressibility remains valid, the change in C will be small for moderate sized particles. For example, a ΔP equal to 7% of atmospheric pressure produces an increase in C of 2% for a .5 μm diameter particle. This will not result in large differences in the U_p calculated by the two methods. Secondly, no interpolations are needed to provide gas velocity in the solution of Equation (4.8) since the values of U_p^* are calculable for all x^*.

For the present case, the error parameters for the Runge-Kutta routine were set just as in Section 3.4.4 (i.e., EPS = ETA = 10^{-5}). The entrance conditions were $U_p^* = U_g^*$ at $x^* = 0$. $U_g^* = 1$ was assumed for all x^* greater than 10/tan α. U_p^* was calculated for $\alpha = 15°$, 30°, and 45° at the exit of the nozzle and at positions .2a, .4a, and .6a beyond the exit of the nozzle. St was varied from .02 to 200 and Re from .1 to 100. The program, named CONOPT, is listed in Appendix D with a glossary of terms and was run on the University of Minnesota's CDC 6400 computer with the MNF compiler.

4.4.3 Results of the Calculations

U_p^* as a function of St and Re is tabulated in Tables 4.2 through 4.13 for $\alpha = 15°$, 30°, and 45° at the exit and at distances equal to .2a, .4a, and .6a from the exit of the nozzle. Figures 4.3 through 4.14 are graphical presentations of the numerical results given in the tables.

Stokesian particles are those having $Re_p < .5$. The U_p^* of a particle which has been Stokesian throughout its motion shows no dependence on Re. This follows from Equations (4.12) and (4.6). Hence, the values of U_p^* for particles which have been Stokesian throughout will all fall on one line for a given and distance from the exit. At points beyond the exit, some particles which have been ultra-Stokesian in the nozzle catch up to the gas velocity and become Stokesian. U_p^* for such particles does show a dependence on Re.

Table 4.2 U_p^* as a function of St and Re at the exit of an ideal nozzle, $\alpha = 15°$

	Re							
St	.1	.5	1.	5.	10.	30.	50.	100.
.02	.989	.990	.990	.990	.990	.990	.990	.991
.12	.947	.947	.947	.947	.949	.954	.956	.960
.2	.919	.919	.919	.919	.926	.932	.936	.942
.5	.844	.844	.844	.853	.860	.873	.880	.892
1.2	.741	.741	.741	.759	.768	.790	.803	.823
2.	.671	.671	.671	.693	.704	.730	.746	.771
5.	.538	.538	.538	.564	.578	.611	.630	.663
12.	.416	.416	.419	.443	.457	.491	.512	.547
20.	.352	.352	.355	.377	.391	.424	.445	.479
50.	.254	.253	.257	.274	.286	.314	.333	.364
120.	.180	.180	.183	.196	.205	.228	.243	.269
200.	.146	.146	.149	.160	.167	.187	.200	.223

Table 4.3 U_p^* as a function of St and Re, .2a beyond the exit of an ideal nozzle, α = 15°

	Re							
St	.1	.5	1.	5.	10.	30.	50.	100.
.02	1.000	1.000	1.000	1.000	1.000	1.000	1.000	1.000
.12	.990	.990	.990	.990	.991	.993	.994	.995
.2	.972	.972	.972	.972	.975	.980	.982	.985
.5	.901	.901	.901	.910	.917	.929	.937	.947
1.2	.791	.791	.791	.812	.822	.845	.859	.880
2.	.715	.715	.715	.740	.753	.782	.800	.826
5.	.570	.570	.570	.601	.617	.653	.675	.711
12.	.438	.438	.443	.469	.485	.523	.547	.586
20.	.369	.369	.375	.398	.414	.451	.474	.512
50.	.264	.264	.270	.288	.301	.333	.354	.388
120.	.187	.187	.191	.206	.216	.241	.258	.286
200.	.151	.151	.155	.167	.176	.197	.211	.236

Table 4.4 U_p^* as a function of St and Re, .4a beyond the exit of an ideal nozzle, $\alpha = 15°$

	Re							
St	.1	.5	1.	5.	10.	30.	50.	100.
.02	1.000	1.000	1.000	1.000	1.000	1.000	1.000	1.000
.12	.998	.998	.998	.998	.998	.999	.999	.999
.2	.990	.990	.990	.990	.991	.993	.994	.995
.5	.936	.936	.936	.942	.949	.958	.963	.971
1.2	.830	.830	.830	.851	.861	.882	.895	.914
2.	.751	.751	.751	.778	.791	.821	.838	.864
5.	.598	.598	.598	.632	.649	.688	.711	.748
12.	.459	.459	.465	.493	.510	.551	.577	.618
20.	.386	.386	.392	.418	.435	.474	.500	.541
50.	.276	.275	.281	.302	.316	.350	.372	.410
120.	.194	.194	.199	.215	.226	.253	.271	.302
200.	.157	.157	.161	.174	.183	.206	.221	.249

Table 4.5 U_p^* as a function of St and Re, .6a beyond the exit of an ideal nozzle, α = 15°

	Re							
St	.1	.5	1.	5.	10.	30.	50.	100.
.02	1.000	1.000	1.000	1.000	1.000	1.000	1.000	1.000
.12	1.000	1.000	1.000	1.000	1.000	1.000	1.000	1.000
.2	.996	.996	.996	.996	.997	.997	.998	.998
.5	.958	.958	.958	.962	.966	.974	.978	.983
1.2	.861	.861	.861	.880	.889	.909	.920	.935
2.	.782	.782	.782	.808	.821	.850	.866	.890
5.	.624	.624	.624	.659	.677	.717	.741	.777
12.	.478	.478	.486	.514	.532	.576	.603	.646
20.	.401	.401	.409	.436	.454	.496	.523	.566
50.	.286	.286	.293	.314	.329	.366	.390	.429
120.	.201	.201	.207	.223	.235	.264	.283	.316
200.	.162	.162	.167	.181	.190	.215	.232	.260

Table 4.6 U_p^* as a function of St and Re at the exit of an ideal nozzle, α = 30°

	Re							
St	.1	.5	1.	5.	10.	30.	50.	100.
.02	.978	.979	.979	.979	.979	.981	.981	.982
.12	.901	.901	.901	.901	.911	.918	.923	.930
.2	.858	.858	.858	.866	.873	.884	.891	.902
.5	.755	.755	.755	.772	.781	.801	.814	.833
1.2	.634	.634	.634	.658	.670	.698	.716	.743
2.	.560	.560	.560	.586	.599	.631	.651	.681
5.	.430	.430	.433	.457	.472	.506	.527	.562
12.	.322	.322	.326	.346	.360	.391	.412	.446
20.	.268	.268	.271	.290	.302	.331	.350	.382
50.	.188	.188	.191	.205	.214	.238	.253	.280
120.	.131	.131	.133	.144	.151	.168	.181	.202
200.	.105	.105	.107	.116	.121	.136	.146	.164

Table 4.7 U_p^* as a function of St and Re, .2a beyond the exit of an ideal nozzle, α = 30°

	Re							
St	.1	.5	1.	5.	10.	30.	50.	100.
.02	1.000	1.000	1.000	1.000	1.000	1.000	1.000	1.000
.12	.983	.983	.983	.983	.985	.989	.990	.993
.2	.953	.953	.953	.956	.962	.969	.973	.979
.5	.851	.851	.851	.869	.879	.899	.910	.927
1.2	.714	.714	.714	.743	.758	.791	.810	.839
2.	.628	.628	.628	.661	.678	.716	.738	.774
5.	.478	.478	.485	.513	.531	.572	.598	.639
12.	.354	.354	.361	.385	.402	.441	.466	.507
20.	.293	.293	.300	.321	.336	.372	.395	.433
50.	.204	.204	.209	.225	.237	.265	.284	.316
120.	.141	.141	.145	.157	.166	.187	.201	.226
200.	.113	.113	.117	.126	.133	.151	.163	.184

Table 4.8 U_p^* as a function of St and Re, .4a beyond the exit of an ideal nozzle, α = 30°

	Re							
St	.1	.5	1.	5.	10.	30.	50.	100.
.02	1.000	1.000	1.000	1.000	1.000	1.000	1.000	1.000
.12	.997	.997	.997	.997	.997	.998	.998	.999
.2	.983	.983	.983	.984	.986	.990	.991	.994
.5	.905	.905	.905	.919	.927	.942	.950	.961
1.2	.771	.771	.771	.801	.815	.846	.864	.889
2.	.680	.680	.680	.716	.733	.772	.794	.828
5.	.519	.519	.525	.558	.577	.623	.650	.694
12.	.383	.383	.392	.419	.437	.481	.509	.553
20.	.316	.316	.325	.348	.365	.405	.431	.474
50.	.219	.219	.226	.244	.257	.289	.311	.347
120.	.151	.151	.156	.169	.179	.204	.220	.248
200.	.121	.121	.125	.136	.144	.164	.178	.201

Table 4.9 U_p^* as a function of St and Re, .6a beyond the exit of an ideal nozzle, α = 30°

	Re							
St	.1	.5	1.	5.	10.	30.	50.	100.
.02	1.000	1.000	1.000	1.000	1.000	1.000	1.000	1.000
.12	.999	.999	.999	.999	.999	1.000	1.000	1.000
.2	.994	.994	.994	.994	.994	.996	.997	.998
.5	.939	.939	.939	.947	.954	.965	.970	.978
1.2	.815	.815	.815	.843	.855	.883	.898	.920
2.	.723	.723	.723	.759	.776	.813	.834	.865
5.	.553	.553	.559	.595	.616	.663	.691	.735
12.	.408	.408	.420	.448	.468	.515	.544	.591
20.	.337	.337	.347	.372	.391	.435	.462	.508
50.	.233	.233	.241	.261	.275	.311	.334	.373
120.	.160	.160	.166	.181	.191	.218	.236	.267
200.	.128	.128	.133	.145	.153	.176	.191	.217

Table 4.10 U_p^* as a function of St and Re at the exit of an ideal nozzle, α = 45°

	Re							
St	.1	.5	1.	5.	10.	30.	50.	100.
.02	.965	.965	.965	.965	.965	.969	.970	.972
.12	.854	.854	.854	.863	.869	.881	.888	.900
.2	.800	.800	.800	.813	.821	.838	.848	.864
.5	.681	.681	.681	.702	.713	.739	.754	.779
1.2	.554	.554	.554	.580	.594	.626	.645	.677
2.	.481	.481	.481	.508	.522	.556	.577	.611
5.	.360	.360	.363	.386	.399	.432	.453	.488
12.	.264	.264	.268	.286	.297	.326	.345	.377
20.	.217	.217	.221	.236	.247	.273	.290	.319
50.	.150	.150	.153	.164	.172	.192	.205	.229
120.	.103	.103	.106	.114	.119	.134	.144	.161
200.	.083	.083	.084	.091	.096	.108	.116	.130

Table 4.11 U_p^* as a function of St and Re, .2a beyond the exit of an ideal nozzle, $\alpha = 45°$

	Re							
St	.1	.5	1.	5.	10.	30.	50.	100.
.02	1.000	1.000	1.000	1.000	1.000	1.000	1.000	1.000
.12	.976	.976	.976	.978	.980	.985	.988	.991
.2	.936	.936	.936	.943	.951	.961	.966	.974
.5	.812	.812	.812	.838	.850	.876	.890	.912
1.2	.661	.661	.661	.696	.714	.753	.776	.811
2.	.570	.570	.572	.608	.627	.671	.697	.737
5.	.422	.422	.431	.459	.477	.521	.549	.593
12.	.306	.306	.314	.336	.353	.392	.417	.458
20.	.250	.250	.256	.277	.291	.326	.348	.386
50.	.171	.171	.176	.191	.201	.228	.245	.275
120.	.117	.117	.120	.131	.139	.158	.171	.194
200.	.093	.093	.096	.104	.110	.126	.137	.156

Table 4.12 U_p^* as a function of St and Re, .4a beyond the exit of an ideal nozzle, α = 45°

	Re							
St	.1	.5	1.	5.	10.	30.	50.	100.
.02	1.000	1.000	1.000	1.000	1.000	1.000	1.000	1.000
.12	.995	.995	.995	.996	.996	.997	.998	.998
.2	.977	.997	.977	.980	.982	.987	.989	.992
.5	.883	.883	.883	.903	.912	.931	.941	.955
1.2	.733	.733	.733	.769	.786	.822	.843	.873
2.	.636	.636	.637	.677	.697	.741	.767	.806
5.	.472	.472	.484	.514	.535	.584	.614	.661
12.	.340	.340	.351	.377	.396	.441	.469	.516
20.	.278	.278	.287	.310	.327	.367	.393	.436
50.	.189	.189	.196	.213	.226	.257	.278	.312
120.	.129	.129	.134	.146	.155	.178	.193	.220
200.	.102	.102	.106	.116	.124	.142	.155	.177

Table 4.13 U_p^* as a function of St and Re, .6a beyond the exit of an ideal nozzle, $\alpha = 45°$

	Re							
St	.1	.5	1.	5.	10.	30.	50.	100.
.02	1.000	1.000	1.000	1.000	1.000	1.000	1.000	1.000
.12	.999	.999	.999	.999	.999	.999	1.000	1.000
.2	.992	.992	.992	.992	.993	.995	.996	.997
.5	.925	.925	.925	.937	.946	.959	.966	.974
1.2	.785	.785	.785	.819	.834	.867	.885	.910
2.	.687	.687	.688	.729	.747	.790	.814	.849
5.	.513	.513	.524	.559	.581	.632	.663	.710
12.	.371	.371	.383	.412	.432	.481	.512	.561
20.	.302	.302	.314	.339	.357	.402	.430	.477
50.	.205	.205	.214	.233	.247	.282	.305	.343
120.	.140	.140	.146	.159	.170	.195	.212	.242
200.	.111	.111	.116	.127	.135	.156	.170	.195

4.3

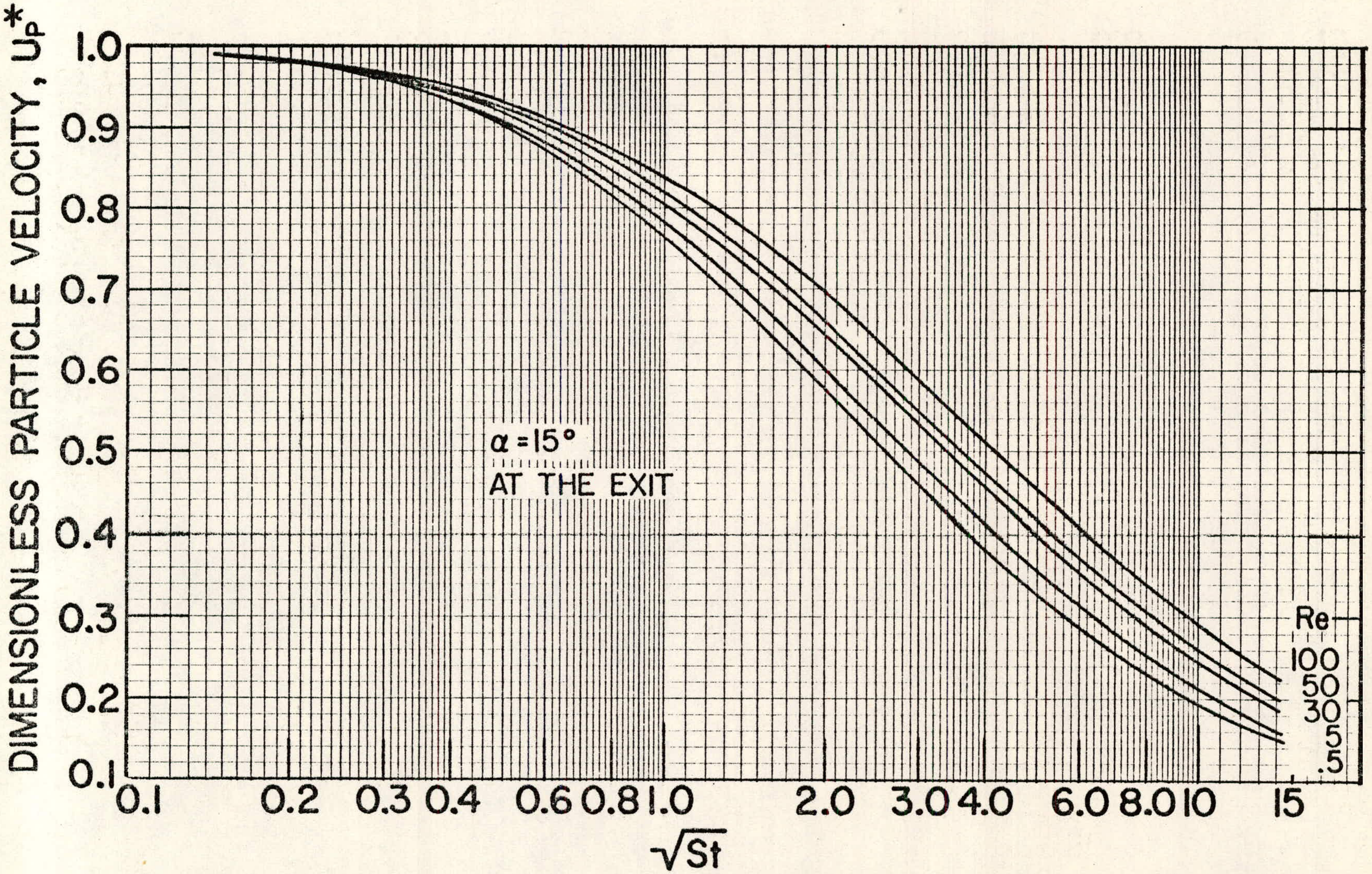

Figure 4.3 Dimensionless particle velocity as a function of St and Re. α = 15°, at the exit.

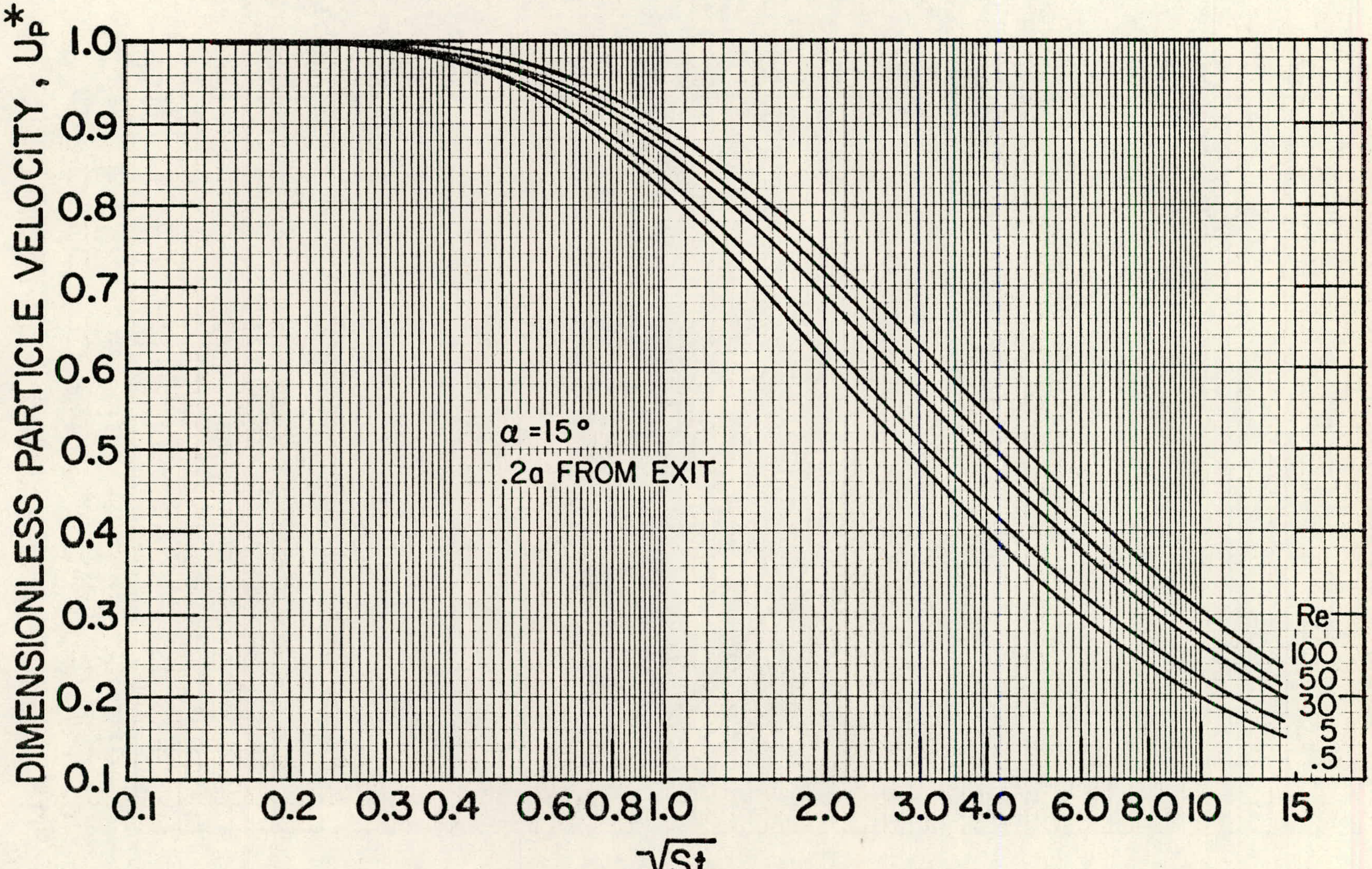

Figure 4.4 Dimensionless particle velocity as a function of St and Re. α = 15°, .2a beyond the exit.

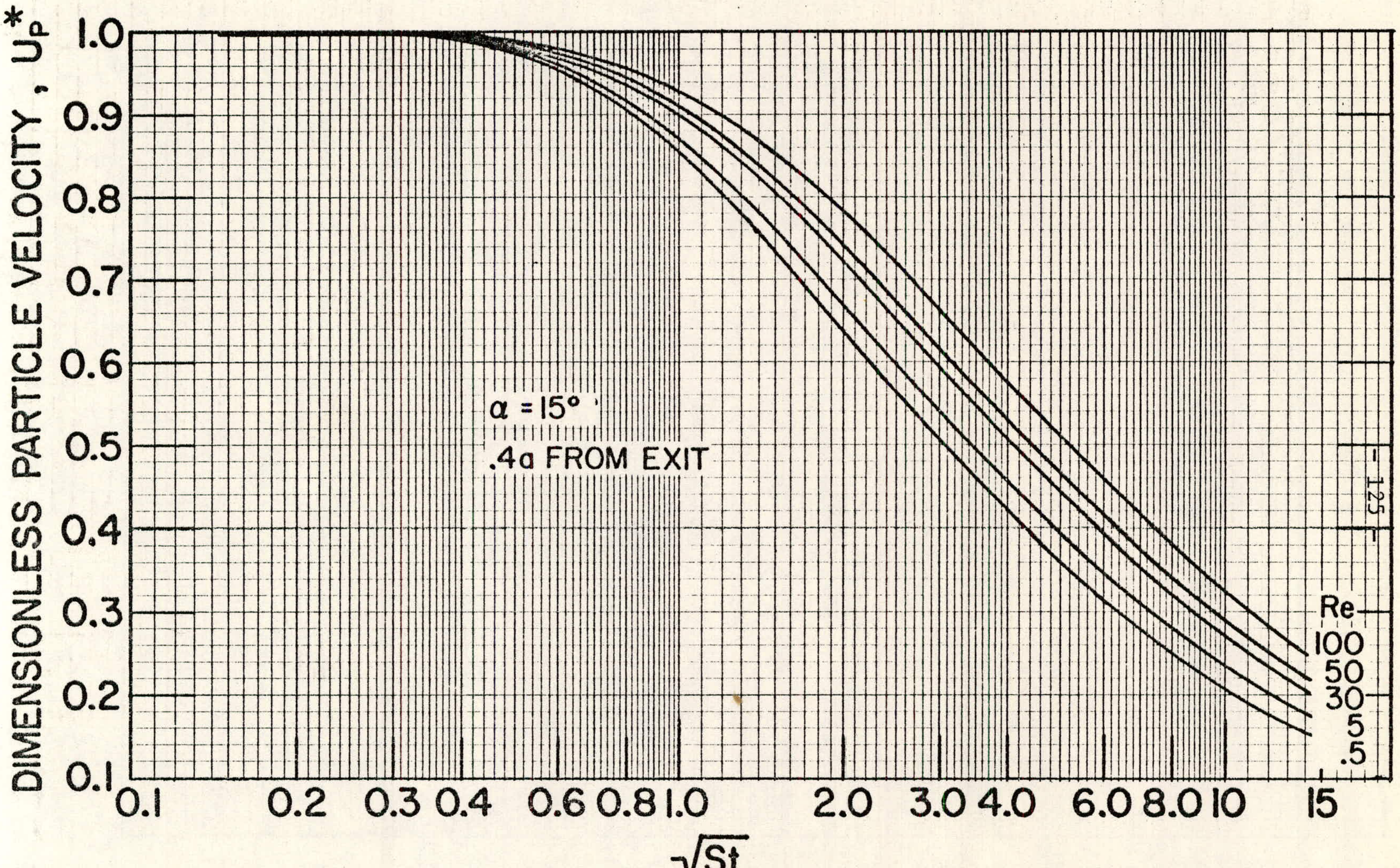

Figure 4.5 Dimensionless particle velocity as a function of St and Re. α = 15°, .4a beyond the exit.

4.6

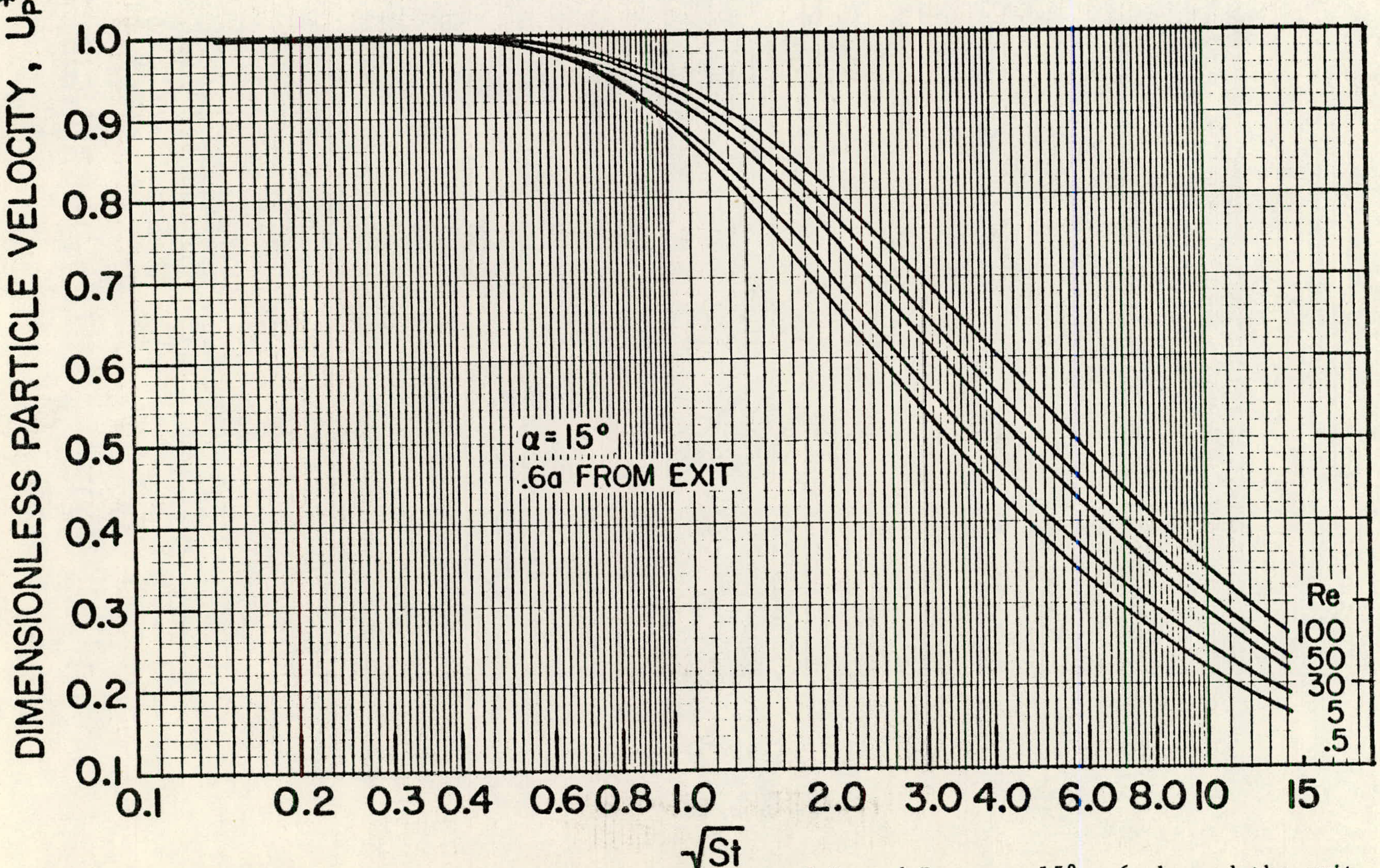

Figure 4.6 Dimensionless particle velocity as a function of St and Re. α = 15°, .6a beyond the exit.

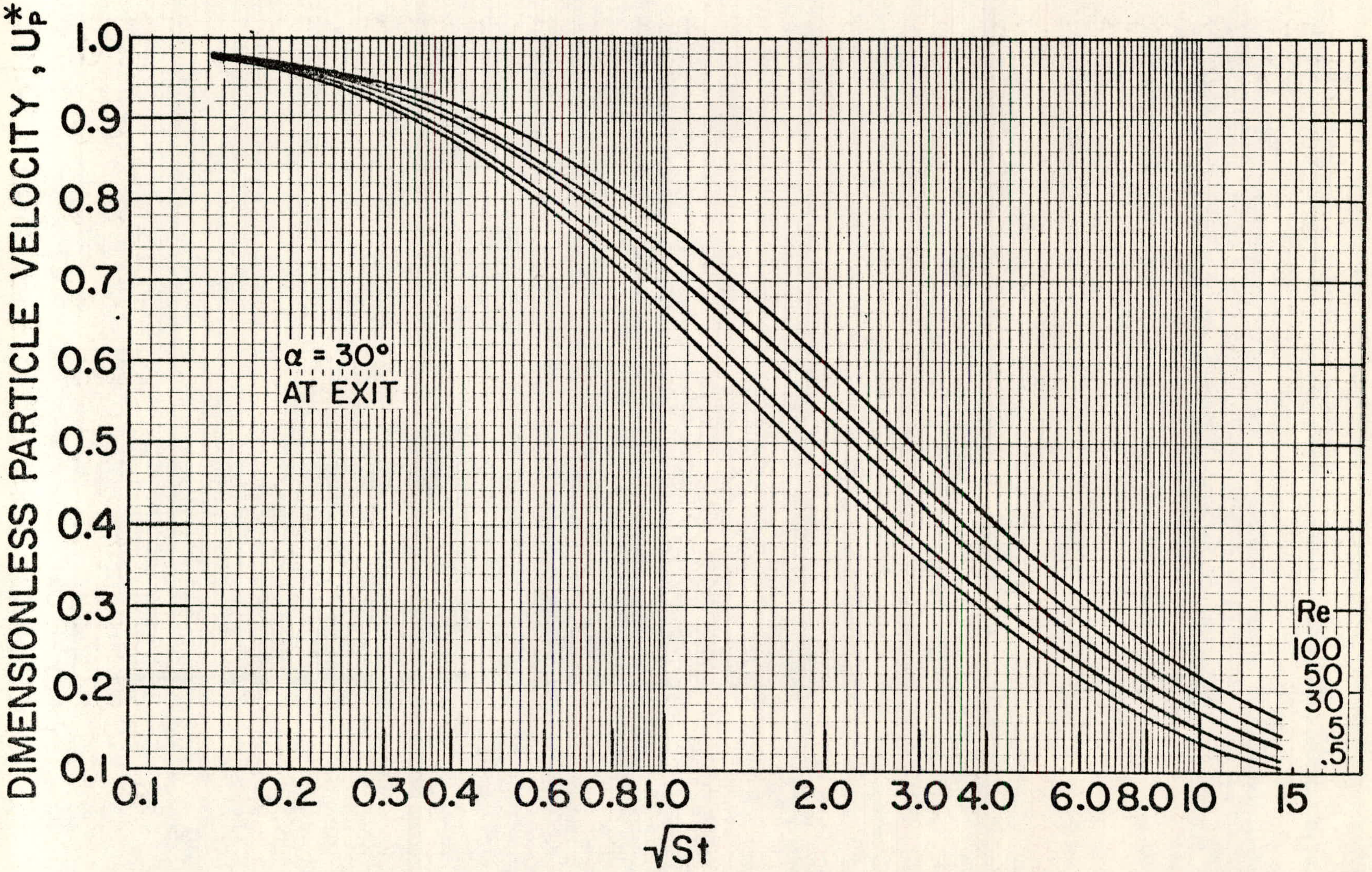

Figure 4.7 Dimensionless particle velocity as a function of St and Re. α = 30°, at the exit.

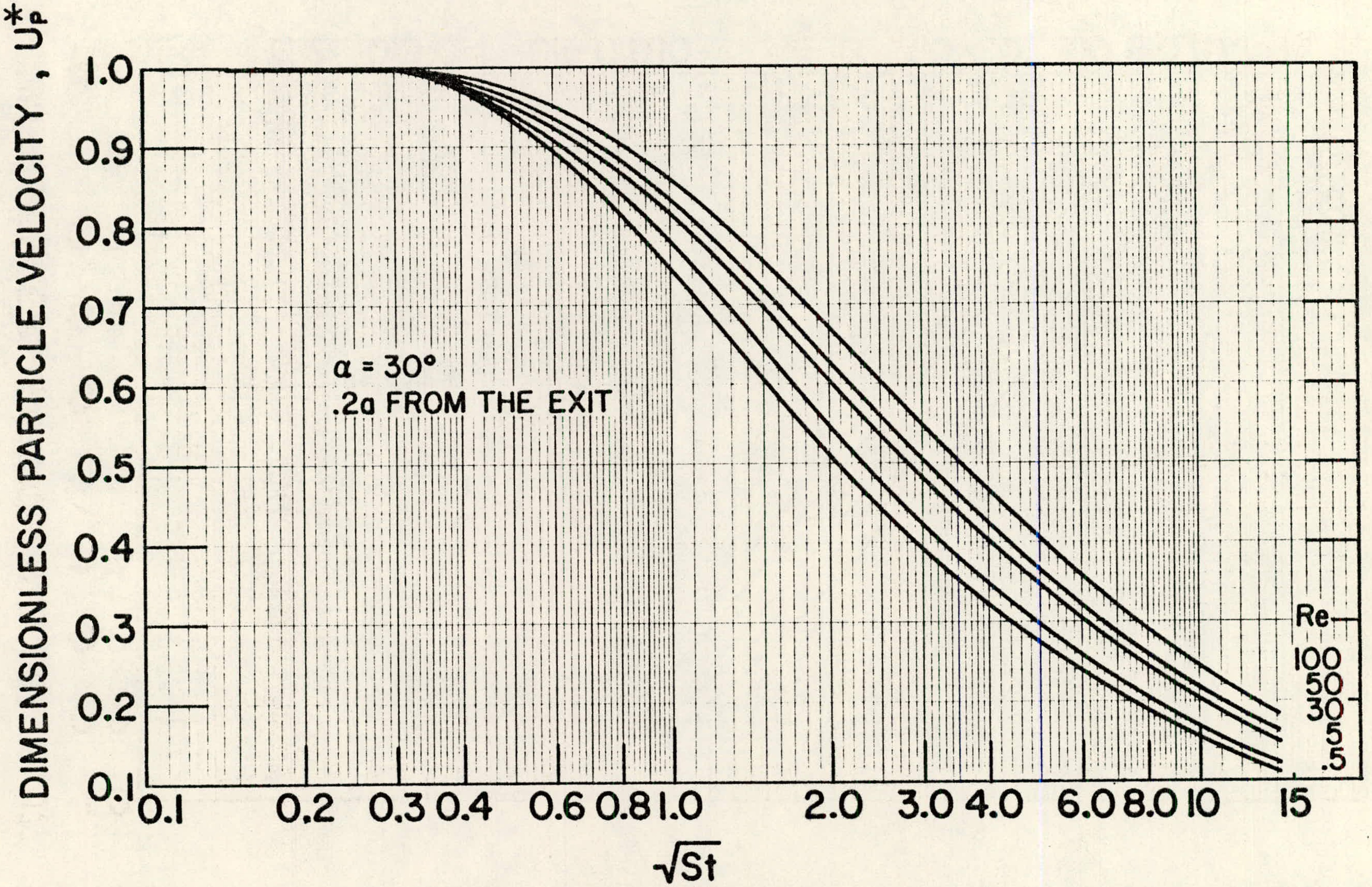

Figure 4.8 Dimensionless particle velocity as a function of St and Re. α = 30°, .2a beyond the exit.

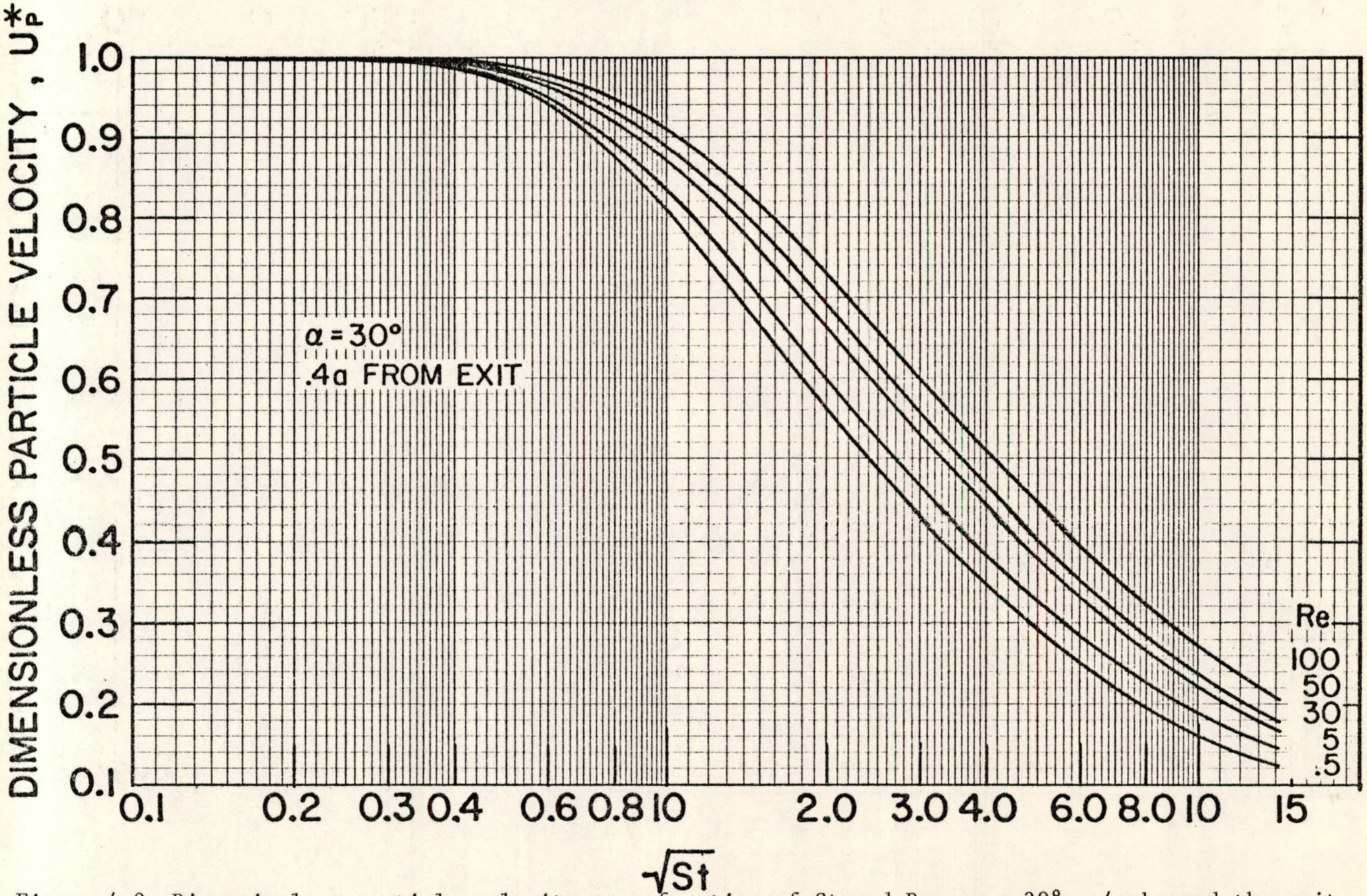

Figure 4.9 Dimensionless particle velocity as a function of St and Re. α = 30°, .4a beyond the exit.

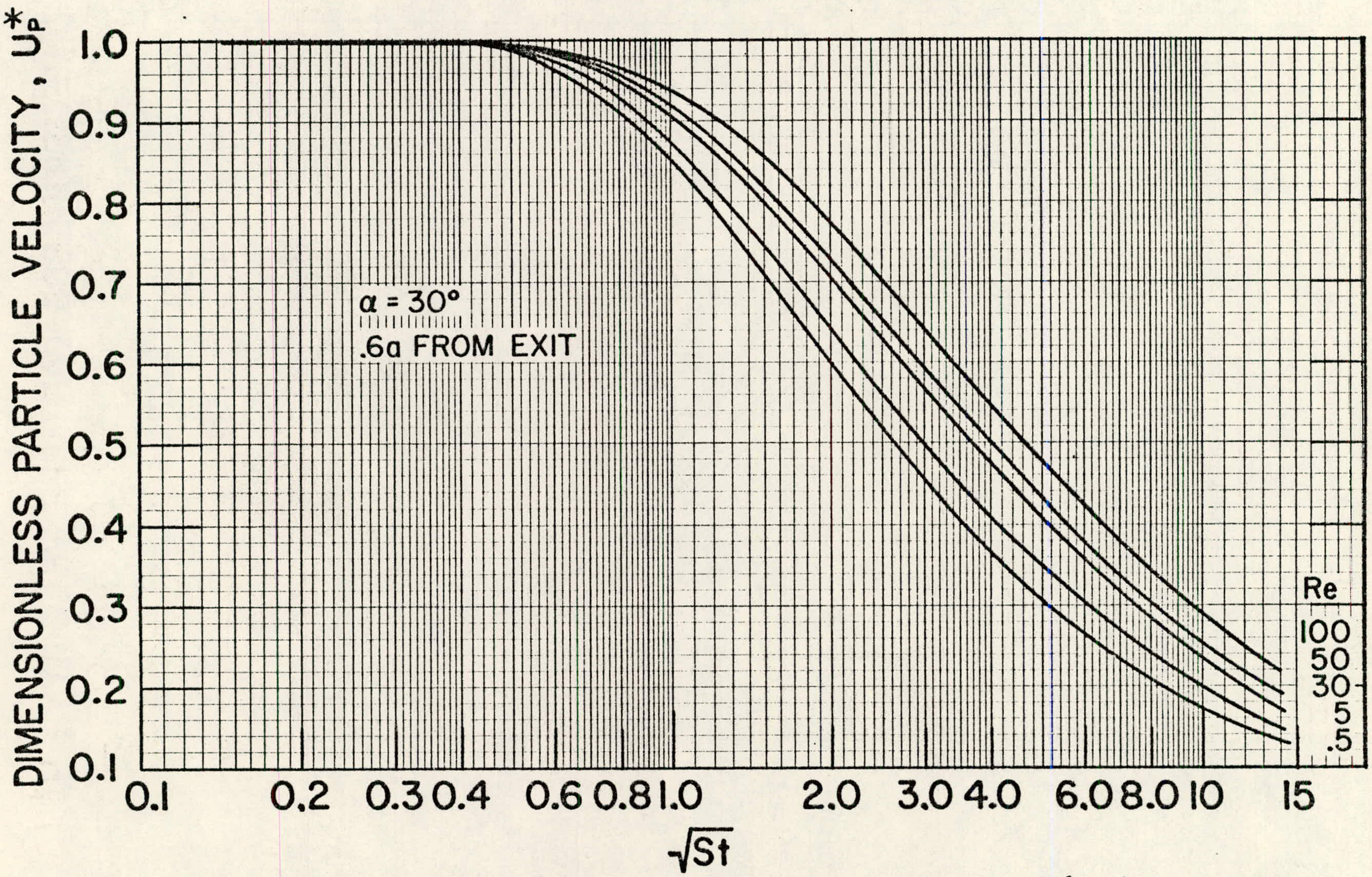

Figure 4.10 Dimensionless particle velocity as a function of St and Re. α = 30°, .6a beyond the exit.

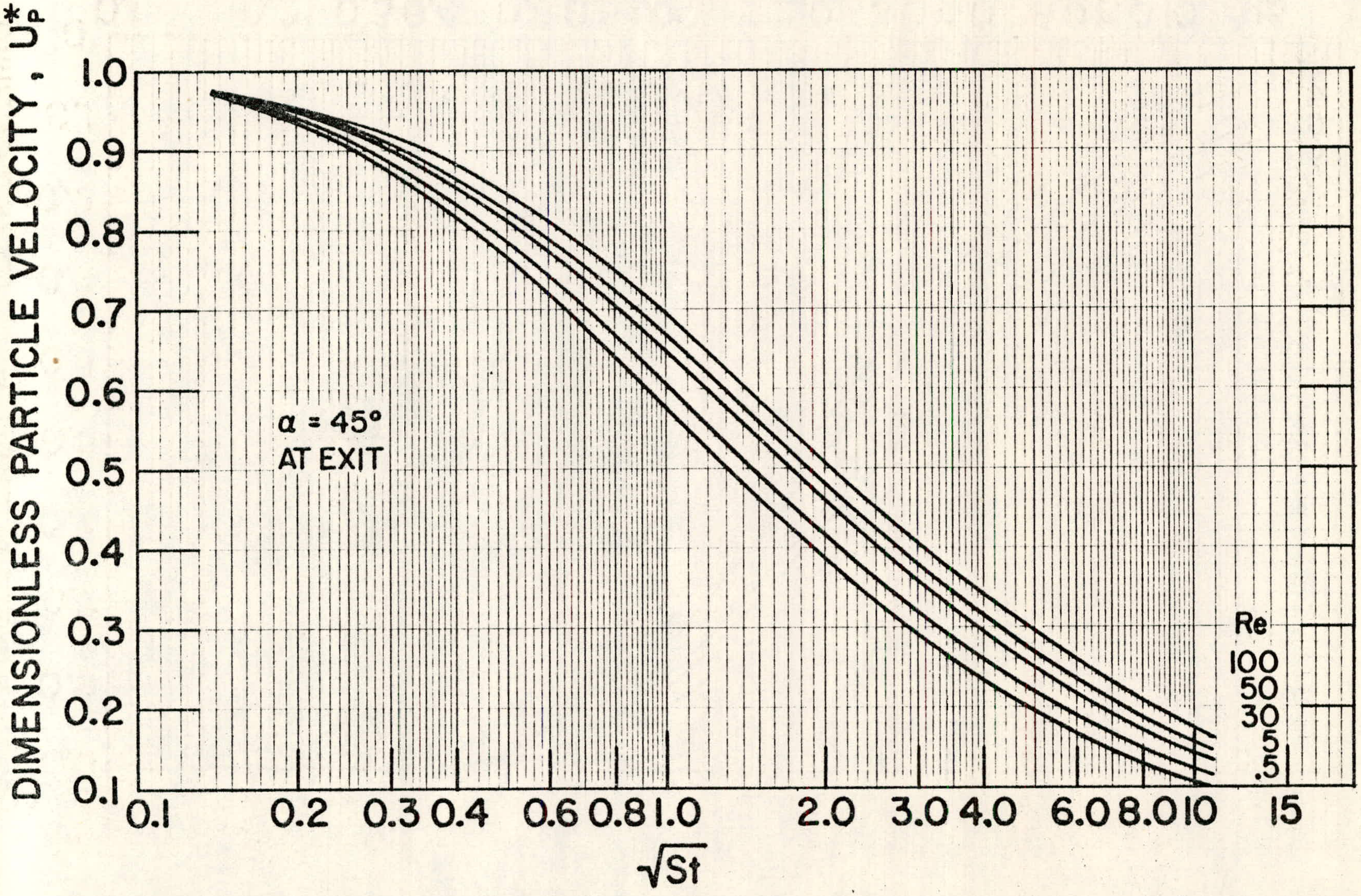

Figure 4.11 Dimensionless particle velocity as a function of St and Re. α = 45°, at the exit.

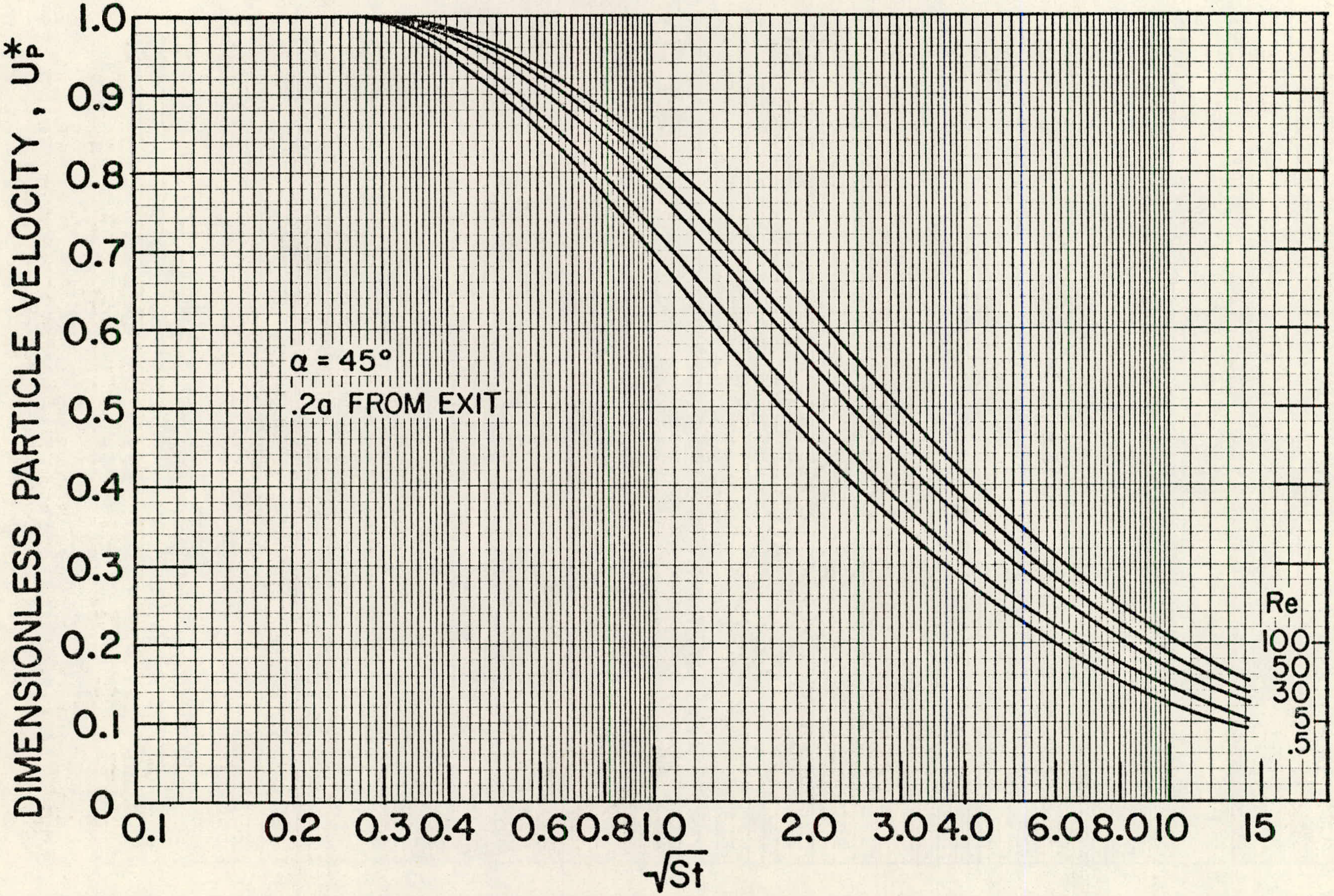

Figure 4.12 Dimensionless particle velocity as a function of St and Re. α = 45°, .2a beyond the exit.

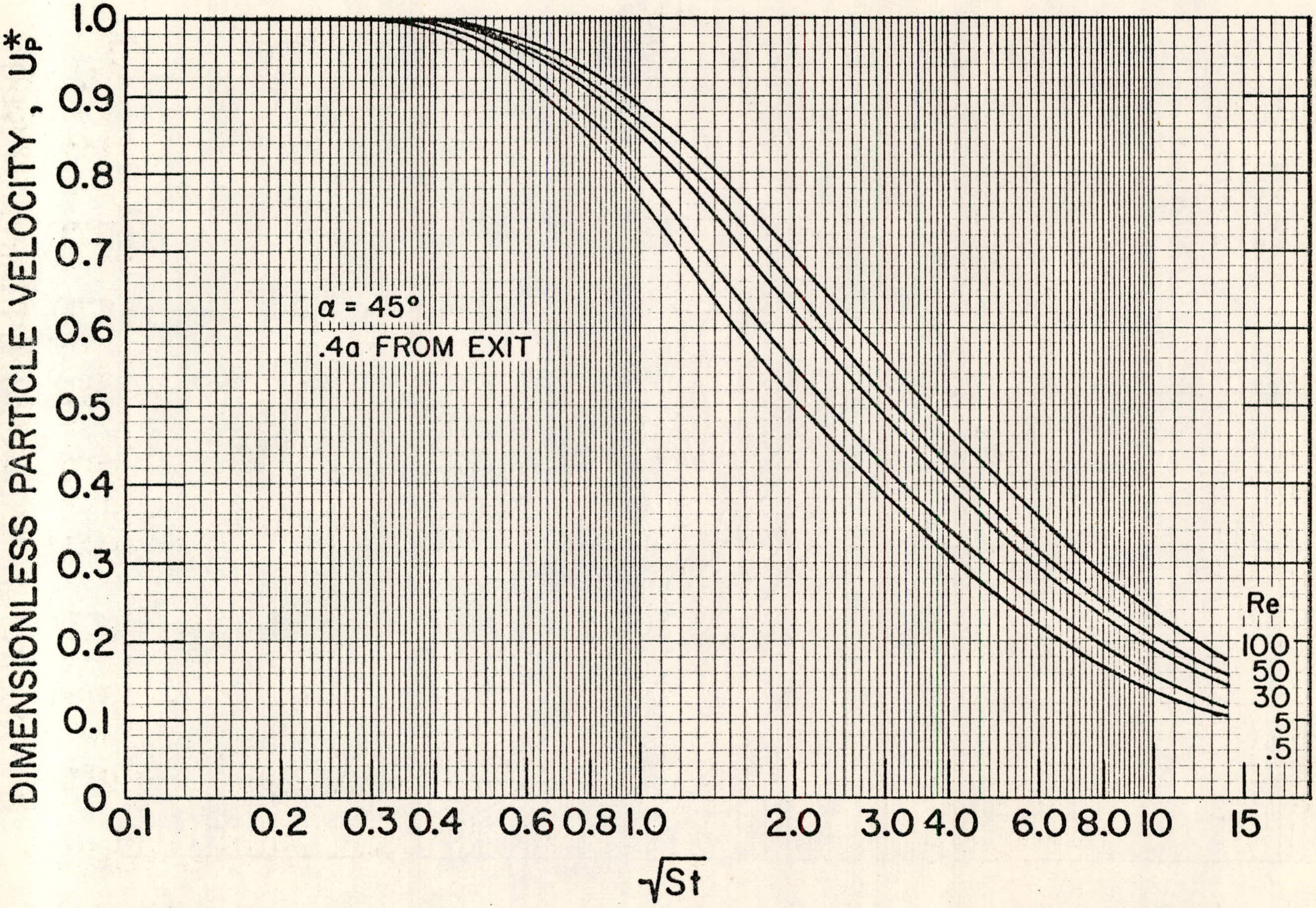

Figure 4.13 Dimensionless particle velocity as a function of St and Re. α = 45°, .4a beyond the exit.

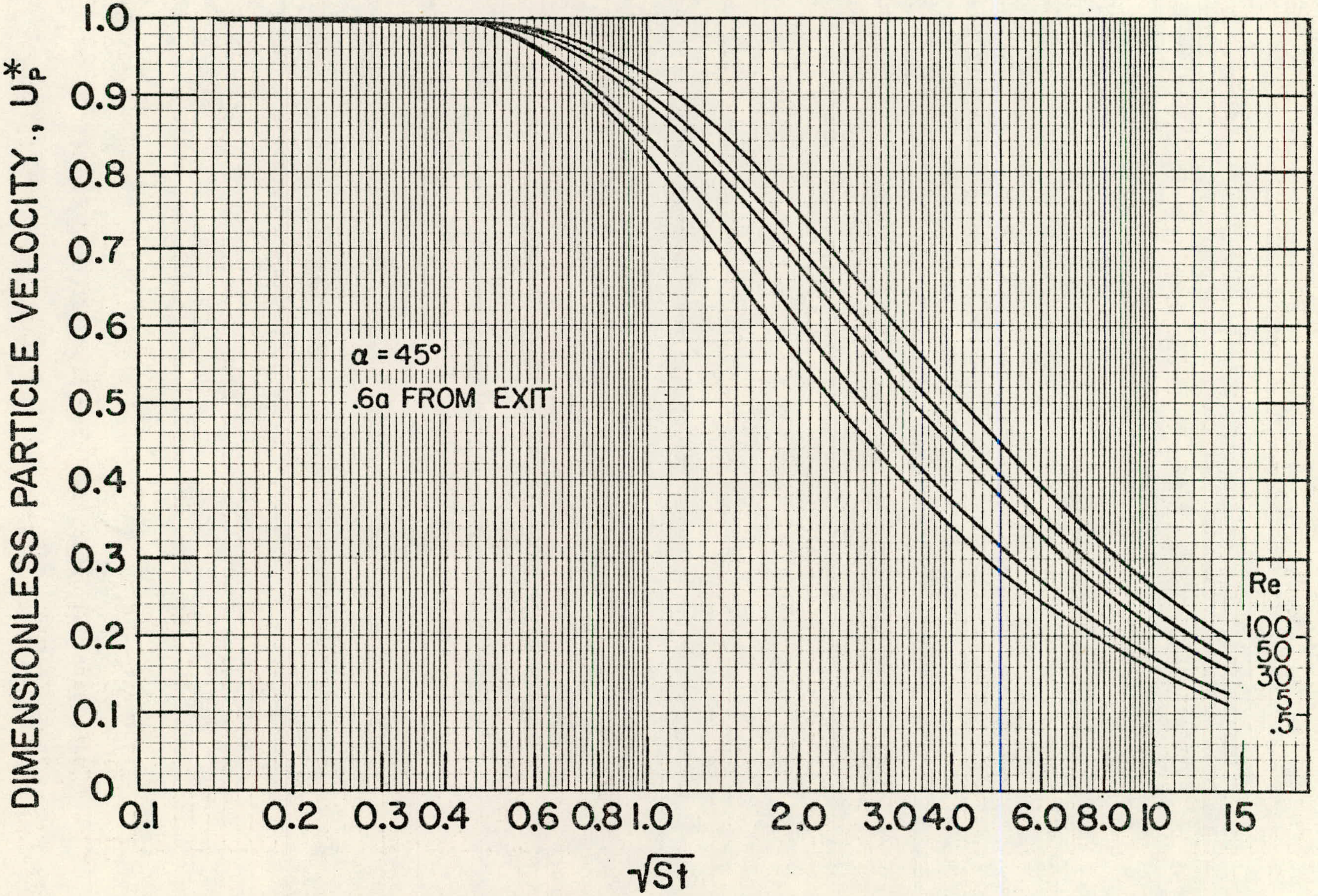

Figure 4.14 Dimensionless particle velocity as a function of St and Re. α = 45°, .6a beyond the exit.

Figure 4.15 shows U_p^* as a function of $\sqrt{St}$ for Stokesian particles at the exit of the nozzle. The figure indicates the effect of varying α even though it is not likely that a real aerosol would be Stokesian throughout the range of St indicated. Clearly, increasing the angle increases the slope of the curve, and the sensitivity of the method.

Figure 4.16 shows the effect of varying the point of measurement for nozzles with $\alpha = 30°$. U_p^* is shown as a function of $\sqrt{St}$ for Stokesian particles at the exit of the nozzle and at distances .2a, .4a and .6a from the exit. The curves are nearly parallel, indicating that the slope does not change very much as the measurement point moves away from the exit. However, the minimum value of St needed to obtain resolution does increase. This implies a decrease in sensitivity as the measurement point moves away from the nozzle, because slope of the U_p^* vs. D_p curve does decrease if St is increased to utilize the full range of U_p^*.

4.5 Construction of Calibration Curves for Ideal Nozzles

Figure 4.17 shows predicted particle velocity as a function of D_p for unit density spheres .01 cm from the exit of an ideal nozzle with $\alpha = 30°$, $a = .05$ cm, and $U_e = 6234$ cm/s. This flow corresponds to $\Delta P = 23.4$ cm of H_2O. First, particle diameters were chosen and C determined from Equation (3.14) or Figure 4.18 (Liu, 1976a). Then St and Re were calculated, and U_p^* found from Figure 4.8. The results are tabulated in Table 4.14, along with particle velocities predicted for the same configuration

4.15

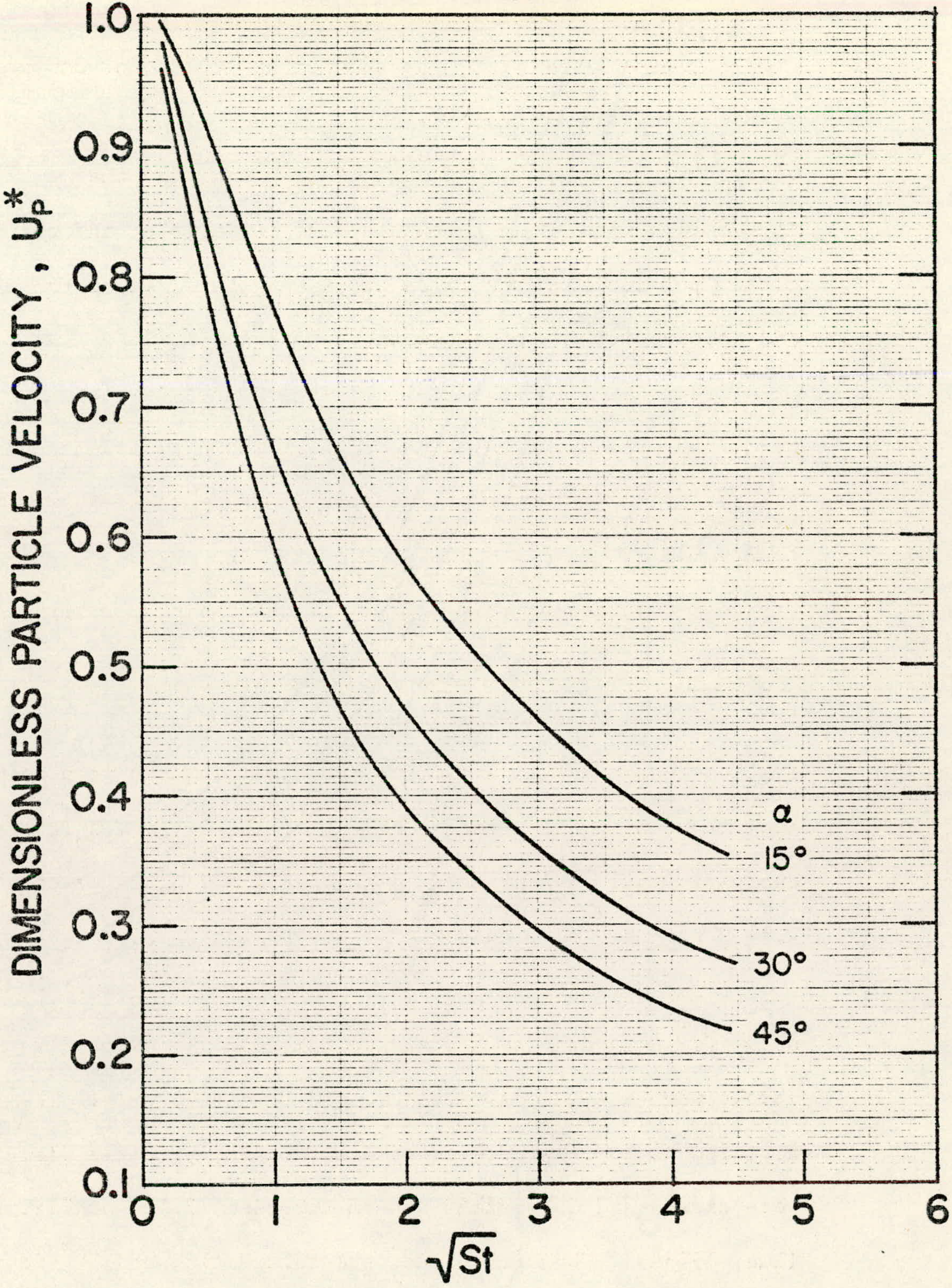

Figure 4.15 Effect of varying α on the velocity of Stokesian particles.

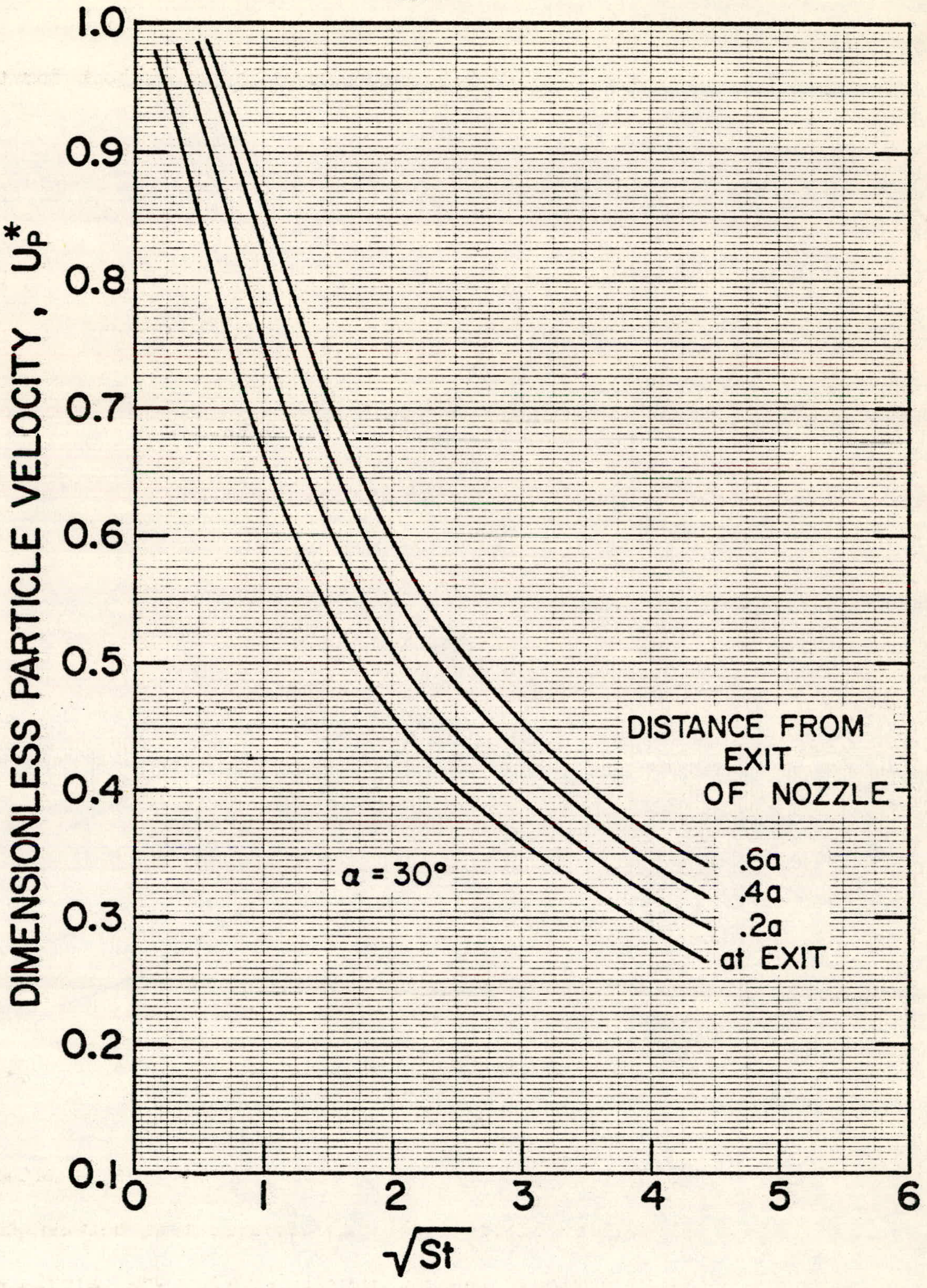

Figure 4.16 Effect of moving the point of measurement on the velocity of Stokesian particles.

Table 4.14 Particle velocities by two methods for the nozzle of Section 4.5

			One-Dimensional Ideal Flow		Boundary Layer Flow	
D µm	St	Re	U_p^*	Re_p	U_p cm/s	U_p^*
.3					6228	1.00
.5	.122	1.97	.985	.03		
.7					5888	.94
1	.428	3.9	.89	.43	5493	.88
1.5	.918	5.9	.78	1.3		
2.	1.58	7.8	.70	2.34		
2.5	2.52	10.0	.63	3.7		
3.	3.50	11.8	.59	4.8		
5.	9.5	19.6	.455	10.7		
6.	1.36	23.6	.40	14.2		
8.	24.0	31.4	.35	20.2		
10.					1922	.31
12.	53.8	47.2	.27	34.0		
15.	83.8	58.9	.24	44.8	1499	.24

using boundary layer flow calculations. These points are also plotted on Figure 4.17, and the agreement between the methods is very good. The boundary layer flow was calculated for Section 4.3 and the centerline velocities are listed in Appendix B.3.2.

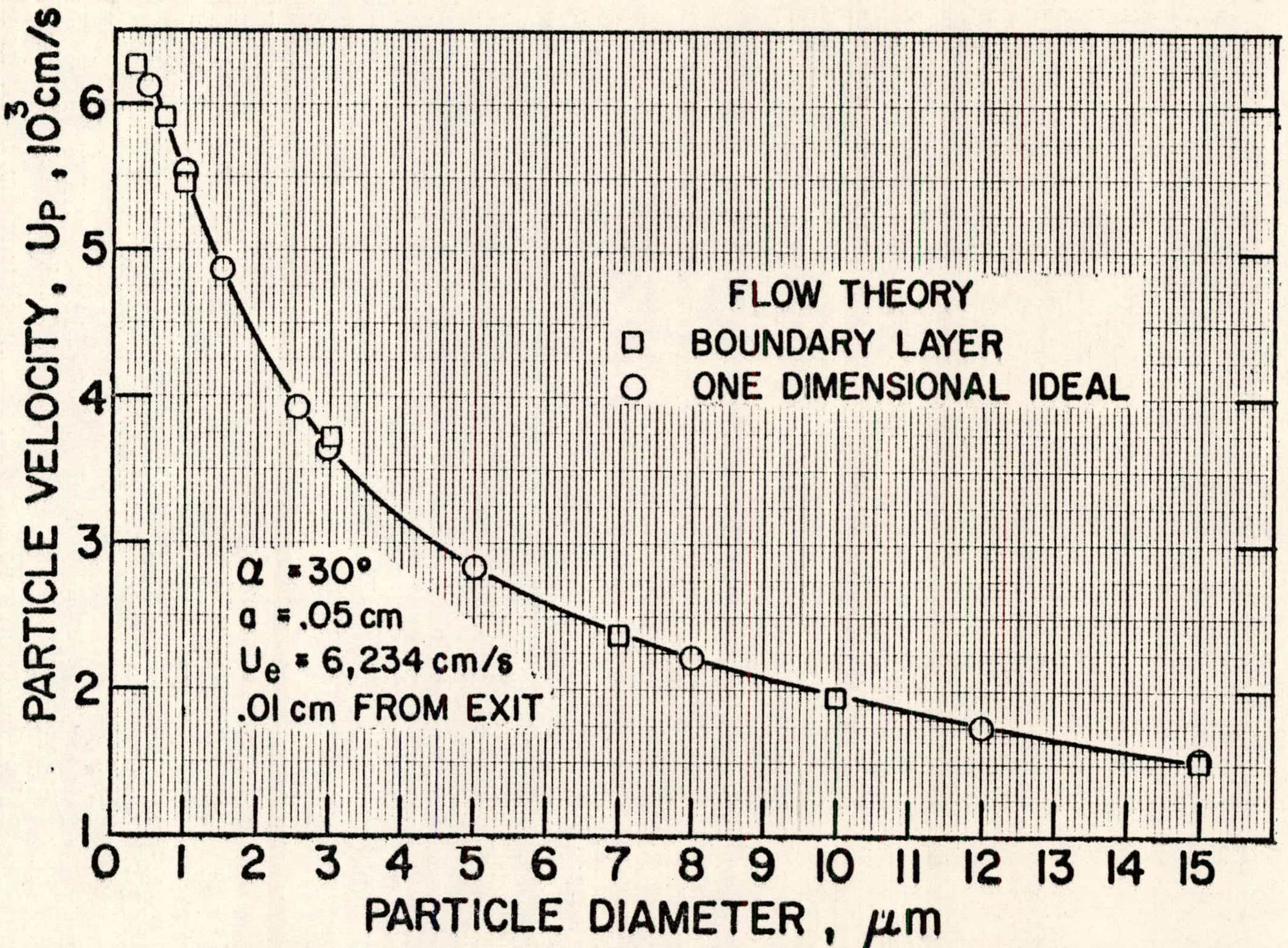

Figure 4.17 Particle velocities calculated using boundary layer and one-dimensional ideal flow calculations.

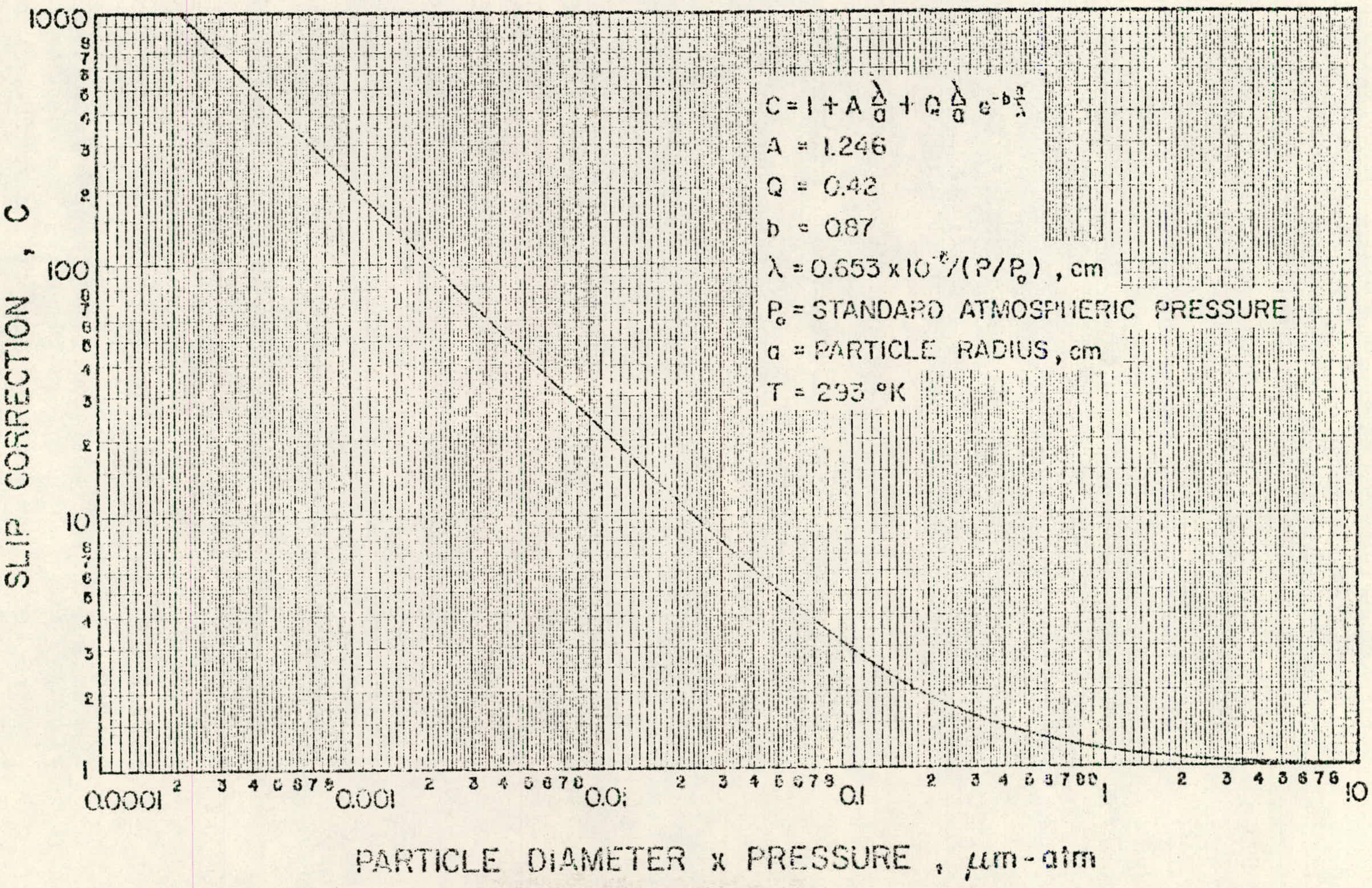

Figure 4.18 Slip correction as a function of $(D_p)(P)$. © B.Y.H. Liu, 1976

4.6 Determination of Aerodynamic Diameter from the Velocity of Particles

The previous section demonstrates that particle diameter can be determined from particle velocity for spherical particles of known density. In the case of uncertain shape and density, an aerodynamic diameter can be assigned to particles based on their velocity.

The aerodynamic diameter determines the impaction and settling behavior of Stokesian particles and is defined as the diameter of a unit density sphere having the same value of St as the particle in question. Equation (4.13) expresses this definition. St is the Stokes number of the particle, D_a is its aerodynamic diameter, and $C(D_a)$ is the corresponding slip correction.

$$\sqrt{C(D_a)}\ D_a = \sqrt{\frac{St\ (18\mu a)}{U_e}} \tag{4.13}$$

Impactors classify particles of different densities and shapes according to D_a. But the dynamics of particles in impactors is generally governed by Stokes' law (Marple and Liu, 1974). It has been shown above, however, that the particles emerging from a nozzle are often ultra-Stokesian and this introduces some uncertainty in the assignment of aerodynamic diameter.

The uncertainty due to uncertain density is illustrated in Figure 4.19. The horizontal coordinate is the aerodynamic diameter and the vertical coordinate is the velocity of spherical particles .01 cm from the exit of the nozzle described in Section 4.5. The curves are drawn for $\rho' = 1\ g/cm^3$ and $\rho' = 3\ g/cm^3$. The points for $\rho' = 1\ g/cm^3$ are taken directly from Table 4.14.

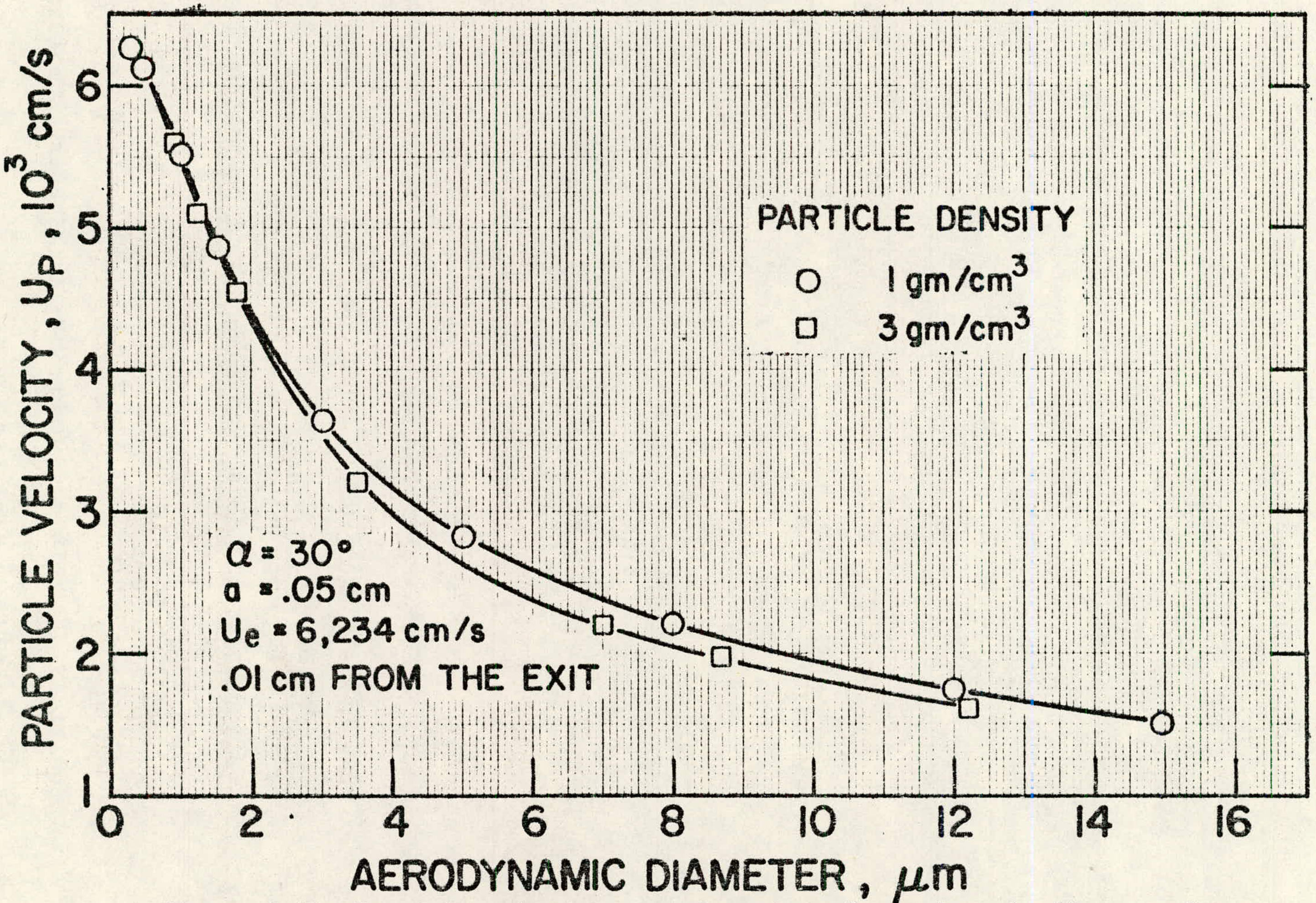

Figure 4.19 Particle velocity as a function of aerodynamic diameter for particles of two densities.

The points for $\rho' = 3$ g/cm^3 are listed in Table 4.15.

Table 4.15 U_p^* for particles with $\rho' = 3$ g/cm^3 in the nozzle described in Section 4.5.

$U_e = 6234$ cm/s

D_p μm	St	Re	U_p^*	Re_p	D_a μm
.5	.368	1.97	.90	.19	.92
.7	.668	2.75	.82	.5	1.27
1.	1.28	3.9	.73	1.05	1.79
1.5	2.76	5.9	.61	2.3	2.65
2.	4.78	7.9	.52	3.8	3.50
4.	18.4	15.7	.36	10.	7.0
5.	28.6	19.6	.32	13.3	8.7
7.	55.4	27.5	.26	20.3	12.2

Figure 4.19 clearly shows that the value of D_a associated with a given U_p depends upon particle density. Analysis of Equations (4.8), (4.11) and (4.12) show why this is true. In Stokes' regime, Equations (4.8) and (4.11) suffice to describe particle motion, and U_p^* is a function of St and x^* alone. This is equivalent, in a given flow, to U_p being a function only of D_a and position. In this case, particle density is irrelevant and D_a is assigned on the basis of U_p alone. In the case where Re_p exceeds .5, U_p^* becomes a function of Re, St and x^*. The addition of Re requires that particle density be specified

in order to relate D_a to U_p.

If the aerosol being studied covers a range of densities, it is necessary to choose a representative or mean value and use it to generate a U_p vs. D_a curve to be used in the analysis of the aerosol. The uncertainty in the values of D_a assigned by this method can be evaluated by looking at curves representing the extremes of the density range. If, for example, the density of an aerosol falls between 1 and 3 g/cm^3 and is analyzed using the nozzle of Figure 4.18, the D_a of a particle with U_p = 2500 cm/s must fall between 5.5 and 6.5 μm.

The spread in D_a associated with a given velocity increases with increasing D_a. Larger values of D_a imply larger values of Re_p which imply a more important role for the ultra-Stokesian term in Equation (4.12). In the next chapter, flow and nozzle parameters will be chosen with this in mind in an effort to keep the uncertainty due to density to an acceptable level.

The importance of non-spherical particle shape also depends upon Re_p. Happel and Brenner (1965) and Fuchs (1964) report that for small Re_p, the drag experienced by a large class of non-spherical particles is proportional to velocity. This implies that the equations describing particle motion can be written in the form of Equations (4.8) and (4.11). In this case, St is not defined by Equation (4.5) but includes terms to account for the shape and orientation of the particle in the flow. These correction factors do not depend upon Re_p, however, and therefore the value of D_a assigned to an irregular particle in Stokes' regime can be used to predict the behavior of the particle in all low Reynolds number situations (assuming the same orientation).

At the values of Re_p experienced in the nozzle, the motion of some non-spherical particles can be described by Equations (4.8) and (4.12). Thus the value of D_a assigned to such particles based on their velocity can be used to predict particle motion, at least at smaller values of Re_p. In such cases, the definition of St includes the same factors for shape and orientation as in Stokes' regime. Hence, the classification of these non-spherical particles by the nozzle is equivalent to that made by an impactor.

Fuchs (p. 42) reports that "for round, cubical and octahedral particles" having Re_p less than about 100, the dependence of C_D on Re_p is the same as that given in Equations (4.11) and (4.12). Particles with "sharper angles and edges", such as tetrahedra and discs, can be described by the same equations as long as Re_p is under 10.

So for many kinds of non-spherical particles, the velocity of particles in the nozzle can be used to make valid assignment of D_a. This ability decreases as Re_p increases.

CHAPTER 5

DESIGN CONSIDERATIONS FOR A PRACTICAL LASER-DOPPLER INSTRUMENT

5.1 Introduction

Techniques developed in the last two chapters are used here to make a design study of a practical instrument for aerodynamic particle size measurement. The instrument will employ an ideal nozzle, as described in the last chapter, and a laser-Doppler velocimeter. The present design study will treat the choice of α, U_e, a, the measuring position, and the fringe spacing in the measuring volume. These variables determine the response of the instrument. Optical, mechanical and electronic components will not be discussed as they are beyond the scope of this investigation.

The instrument is intended for studying atmospheric aerosols and will fit into the aerosol analyzing system which has been in use at the University of Minnesota (Whitby et al., 1975). It will size particles in the .5 μm to 10 μm diameter range, so that it overlaps the largest size range covered by the electrical aerosol analyzer and exceeds the entire range now sized by the modified Royco 220 single particle optical counter (Willeke and Liu, 1976).

This particular objective was chosen because the problems posed by atmospheric studies are well-known in this laboratory and are quite challenging. It must be acknowledged that the optical counter now in use provides useful data, especially at the lower end of the size range where at normal humidities, wet spherical particles dominate atmospheric aerosol. At the upper end where mechanically generated non-spherical dusts become important, the particular virtue of the velocimetric instrument will be better appreciated. This virtue is that it provides a direct measure of aerodynamic particle size independent of optical properties of the aerosol. It will also be seen that the accuracy and resolution expected from the velocimetric instrument are certainly adequate for the study of atmospheric aerosols.

Since the theory has not been tested for all values of α, some of the experimental results have been carried over from the test nozzle and assumed to apply to the proposed nozzle. Hence the performance attributed to the proposed nozzle set-up is somewhat conjectural.

5.2 Characteristics Required of the Nozzle and Measuring Volume

This section presents a list of the characteristics required of the proposed device. Only those properties which are influenced by nozzle and viewing volume geometry and gas velocity are discussed, since these are the variables which can be controlled and investigated using the techniques at hand.

The resolution of the system must be sufficient to allow meaningful classification of aerosols. In the present analyzing system, each decade in particle diameter is divided into four channels. The analysis of an aerosol then consists of measuring the size of particles and recording the number that fall into each channel. The resolution of aerosol sizing instrument must then be small compared to the width of the channels in the range it covers.

The precision of the measurements must be sufficient so that particles are classified repeatably.

Atmospheric aerosols contain particles with a range of density and particle shape. Both factors introduce uncertainty into the assignment of aerodynamic diameter. This uncertainty must be small enough to allow accurate classification of aerosols.

The aerosol sample rate of the nozzle must be large enough so that meaningful statistics can be gathered for large particles which are present in relatively small concentrations in the atmosphere.

The measuring volume must be small enough so that coincidences of particles in the measuring volume are infrequent. Since the laser power must be spread over the entire measuring volume, it is desirable that it be small enough so that a reasonably priced laser can be used.

5.3 The Effects of U_e, a, α, the Measuring Position, and Fringe Spacing in the Measuring Volume

The variables under control in this investigation are α, a, U_e, the position of the measuring volume, and the fringe spacing, d, in the measuring volume. This section discusses the influence of these variables on the properties listed in Section 5.2.

The resolution of the instrument will be a concern only for the smallest particles. For the larger sizes, the resolution will be more than adequate. Resolution equals the sensitivity, defined as the slope of the U_p^* vs. D_a curve, divided into the smallest meaningful change in U_p^* detectable by the instrument. For small particles moving at higher velocities, the σ_g of velocity distributions increases in the test nozzle, and hence, the smallest meaningful change in U_p^* increases. At low velocities, the slope of the calibration curve tends to zero. Both effects tend to degrade resolution. In the present case, the major concern was to gain adequate sensitivity at reasonable values of U_e.

The sensitivity is affected in several ways. Figure 4.15 indicates that increasing α should increase sensitivity, and Figure 4.16 indicates that moving the measuring volume away from the nozzle decreases the sensitivity. Figure 5.1 was plotted from Figure 4.12 to show the effect of D and U_e on sensitivity. The graph shows D_a as a function of U_e for fixed values of U_p^*. By fixing a value of U_e, U_p^* can be found as a function of D_a. The curves represent lines of constant U_p^* for a = .05 and a = .1 cm for an aerosol with $\rho' = 1$ g/cm^3. This plot is of heuristic value and should not be used for serious interpolation as the curves were each generated from only three points. It is clear that for a fixed value of a, the sensitivity for smaller particles increases with increasing U_e, and that the U_p^* vs. D_a curve tends to flatten out for larger particles. Also, for a fixed U_e, a smaller value of a produces more sensitivity.

The uncertainty due to variations in density and particle shape is more important for larger particles where Re_p gets large.

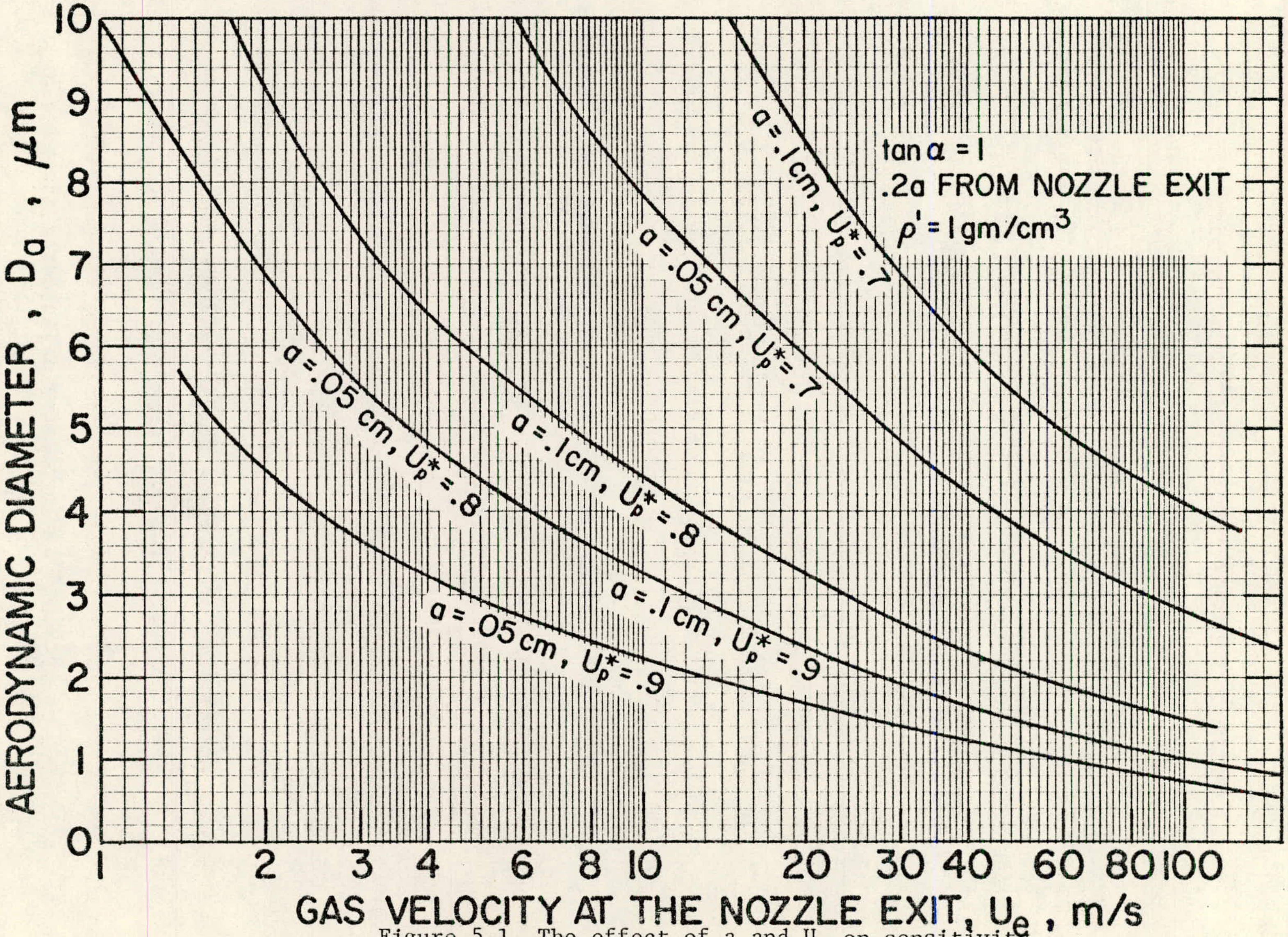

Figure 5.1 The effect of a and U_e on sensitivity.

This uncertainty increases with U_e.

The aerosol sample rate is limited by a and U_e. It determines whether enough large particles to provide good statistics can be analyzed in a convenient period of time. The flow profiles shown in Chapter 3 indicate that the velocity profile in the test nozzle is nearly flat out to about .7 of the radius. Thus, approximately one-half of the flow could carry aerosol without significant variation in particle velocity due to the flow profile. Applying that result to the present case implies that the maximum aerosol sample flow rate in cm^3/s is $\pi\ (.7a)^2\ U_e$.

The size of the measuring volume equals the product of the cross-sectional area of the aerosol sample flow, the fringe spacing and the number of Doppler cycles needed for a frequency determination. Increasing the volume increases the chance of coincidences and decreases the maximum concentrations which can be sampled with the instrument.

The choice of U_e, d and a involves compromise. Sensitivity gained for small particles by increasing U_e implies increased uncertainty for large particles. Sensitivity gained for small particles by decreasing a increases the difficulty of obtaining adequate statistics for large particles which are relatively rare in the atmosphere. Improved counting statistics for large particles obtained by increasing a increases the size of the measuring volume and hence increases the chance of coincidence of smaller particles and increases the laser power requirements.

5.4 U_e, α, a, d and the Position of the Measuring Volume for the Proposed Nozzle

Weighing the compromises listed above, the following choices were made: $\alpha = 45°$, $a = .05$ cm, $U_e = 9500$ cm/s, and $d_f = 10$ μm. The distance from the nozzle exit to the viewing volume was chosen to be .01 cm. Experience gained in the experimental investigations indicates that it would be difficult to get closer to the nozzle. These choices are made principally to obtain sufficient resolution for small-size particles and sufficient aerosol sampling rate for large particles. If minimizing the uncertainty in sizing large, non-spherical aerosols of unknown density is deemed to be very important, a second choice can be made for U_e. In such a case, $U_e = 9500$ cm/s would be used to size particles with D_a less than about 2 μm and $U_e = 1200$ cm/s could be used for sizing particles with D_a between 2 μm and 10 μm. The other parameters remain unchanged; only the gas velocity is altered to change scales.

5.5 Results of Calculations

Table 5.1 gives D_a, St, Re and U_p^* calculated for particles of density 1, 2 and 3 g/cm^3, .01 cm from the exit of the proposed nozzle with $U_e = 9500$ cm/s. Some of these values are plotted in Figures 5.2 and 5.3. Table 5.2 and Figure 5.4 displays the same results for the nozzle with $U_e = 1200$ cm/s. The pressure drop is 54.6 cm of H_2O for the larger flow and 0.87 cm of H_2O for the smaller flow. These results were calculated using the program described in Chapter 4.

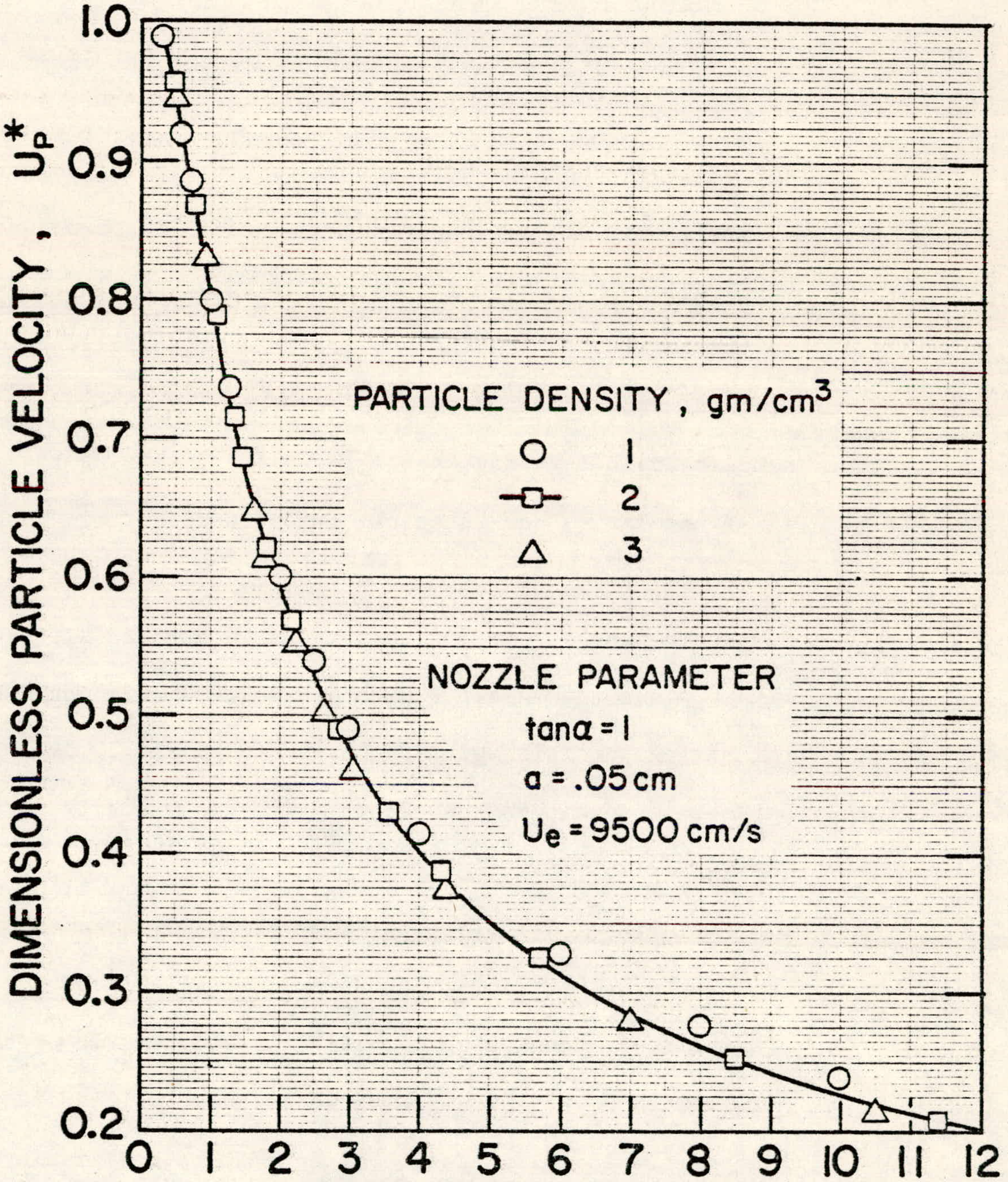

Figure 5.2 Dimensionless particle velocity as a function of aerodynamic diameter, U_e = 9500 cm/s.

5ı2

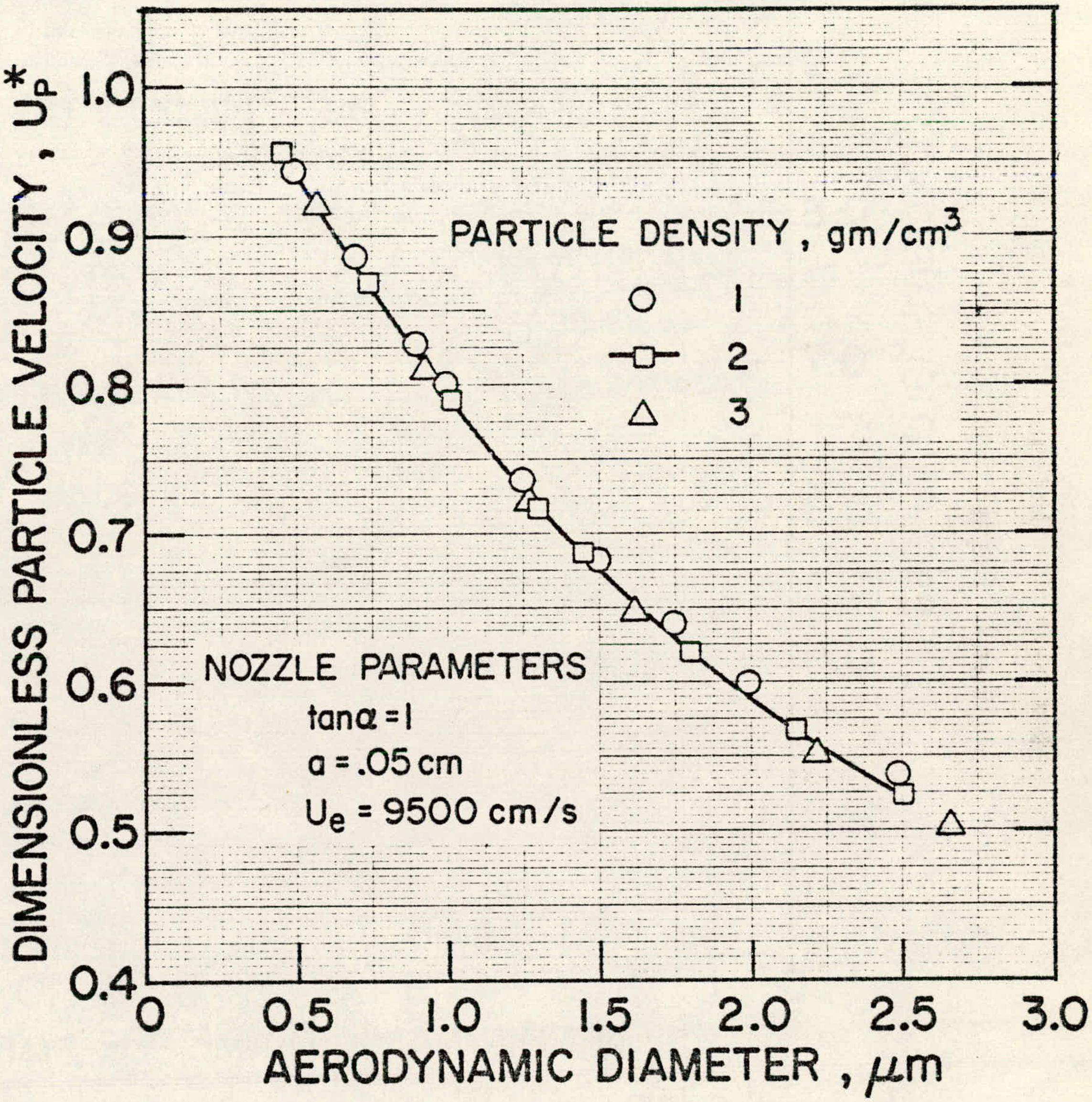

Figure 5.3 Dimensionless particle velocity as a function of aerodynamic diameter, U_e = 9500 cm/s.

5.4

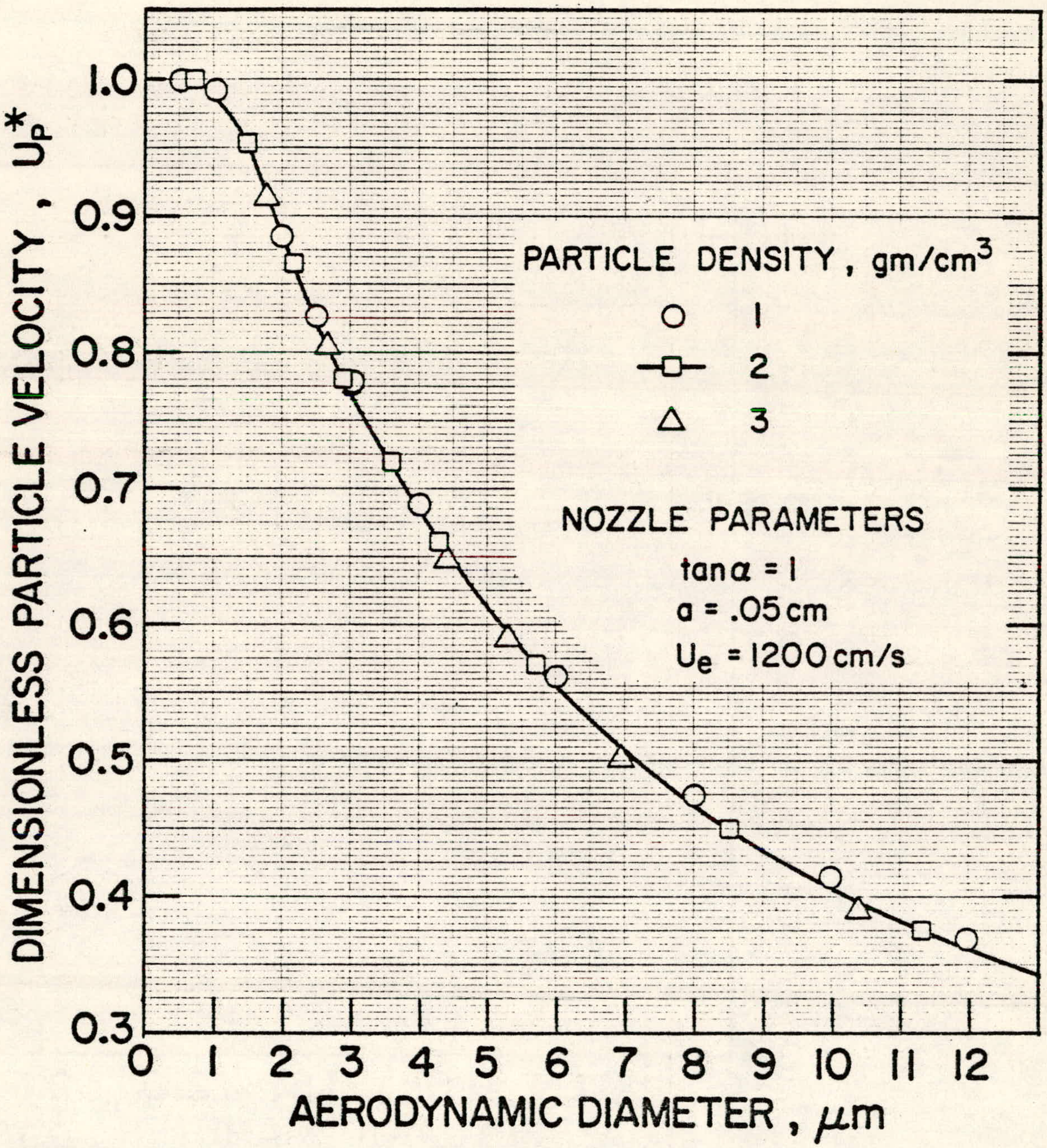

Figure 5.4 Dimensionless particle velocity as a function of aerodynamic diameter, U_e = 1200 cm/s.

Table 5.1 U_p^*, D_a, St and Re for particles in the proposed nozzle, U_e = 9500 cm/s

		ρ' = 1 g/cm^3			ρ' = 2 g/cm^3			ρ' = 3 g/cm^3		
D_p μm	Re	St	U_p^*	D_a μm	St	U_p^*	D_a μm	St	U_p^*	D_a μm
.3	1.80	.080	.992	.3	.158	.957	.452	.238	.920	.57
.5	2.99	.186	.944	.5	.372	.869	.737	.560	.813	.92
.7	4.19	.340	.887	.7	.678	.788	1.02	1.02	.721	1.27
.9	5.39	.536	.829	.9	1.07	.717	1.30	1.61	.647	1.61
1.0	5.99	.652	.800	1.0	1.31	.686	1.45	1.96	.615	1.79
1.25	7.48	.992	.738	1.25	1.98	.620	1.80	2.99	.552	2.22
1.50	8.98	1.40	.685	1.5	2.80	.567	2.15	4.20	.501	2.66
1.75	10.5	1.88	.640	1.75	3.76	.524	2.51	5.64	.460	3.09
2.0	12.0	2.42	.601	2.	4.86	.488	2.86	7.28	.426	3.52
2.5	15.0	3.74	.538	2.5	7.48	.430	3.57	11.2	.374	4.39
3.0	18.0	5.32	.489	3.	10.7	.387	4.28			
4.0	24.0	9.34	.414	4.	18.7	.325	5.69	28.0	.279	6.99
6.0	35.9	20.8	.328	6.0	41.6	.257	8.52	62.2	.214	10.5
8.0	47.9	36.6	.276	8.0	73.4	.208	11.4	110.	.176	13.9
10.0	59.9	57.0	.240	10.	114.	.180	14.2	171.	.151	17.4

Table 5.2 U_p^*, D_a, St and Re for particles in the proposed nozzle, U_e = 1200 cm/s

		$\rho' = 1\ g/cm^3$			$\rho' = 2\ g/cm^3$			$\rho' = 3\ g/cm^3$		
D_p μm	Re	St	U_p^*	D_a μm	St	U_p^*	D_a μm	St	U_p^*	D_a μm
.5	.378	.024	1.00	.5	.048	.999	.737	.071	.995	.92
1.	.76	.082	.991	1.	.164	.954	1.45	.247	.913	1.78
1.5	1.13	.176	.948	1.5	.354	.865	2.15	.530	.803	2.65
2.0	1.51	.306	.886	2.0	.614	.780	2.86	.920	.716	3.52
2.5	1.89	.472	.826	2.5	.944	.719	3.57	1.42	.649	4.39
3.	2.27	.672	.780	3.	1.35	.661	4.28	2.02	.591	5.25
4.	3.03	1.18	.689	4.	3.36	.570	5.69	3.54	.503	6.99
6.	4.54	2.62	.561	6.	5.24	.449	8.52	7.86	3.90	10.4
8.	6.05	4.64	.475	8.	9.26	.374	11.3	1.39	.322	13.9
10.	7.56	7.20	.415	10.	14.4	.322	14.2	21.6	.276	17.4
12.	9.08	10.4	.369	12.	20.8	.284	17.0	31.0	.243	20.8

The three densities were chosen to represent the range of density found in atmospheric aerosol in the size range of interest. Whitby and Cantrell (1975) indicate that the range proposed for this instrument is dominated in the atmosphere by hydroscopic aerosol (accumulation mode) and coarse particles generated mechanically. Under most conditions, the hydroscopic aerosols contain significant amounts of water. Their density is often between 1 and 2 g/cm^3. Much of the aerosol in the coarse range is wind-blown soil, clay, sand, flyash, etc., and a density range of 1 to 3 g/cm^3 will include most of this aerosol. 2 g/cm^3 was taken to be an average and the curves drawn in Figures 5.2 and 5.3 are drawn through the points for $\rho' = 2$ g/cm^3. The other points given are an indication of the range of uncertainty associated with a density ranging from 1 g/cm^3 to 3 g/cm^3.

5.6 Evaluation of the Proposed Nozzle

5.6.1 Resolution and Precision

The resolution of the instrument must be small compared to the width of the channels in the size range it covers. The relevant channel boundaries currently used in the aerosol analyzing system are at .56 μm, 1.0 μm, 1.78 μm, 3.16 μm, 5.62 μm, and 10 μm.

The experience with the test nozzle indicated that resolution is only a problem for submicron particles, and the present discussion will be limited to them. The resolution is limited by the intrinsic dispersion of the instrument. Since there are no experimental results available for the proposed nozzle, the intrinsic dispersion can not be evaluated as was done in Chapter 2 for the test nozzle. However, some experimental results from the test nozzle can be applied in the present case to allow estimates to be made. Let σ_{rs} be the relative standard deviation of the size distribution indicated by the proposed nozzle and σ_{rv} be the relative standard deviation of the corresponding velocity distribution. The two can be related by Equation (2.9) and the calibration curves for the proposed nozzle. In this case, the values of σ_{rv} will be taken from the test nozzle data for the P = 69.1 cm of H_2O case, since the gas velocity approaches the 9500 cm/s flow. Under these conditions and assumptions, the relative standard deviation expected for a size distribution measured for .5 μm PSL with the proposed nozzle is 0.12. This value follows from the assumption of a value of 1.02 for the geometric standard deviation of the velocity distribution. For a 2 μm PSL aerosol, the corresponding values would be $\sigma_{rs} = .03$, based on $\sigma_{rv} = .01$ (i.e., $\sigma_g = 1.01$).

Similar numbers apply to the repeatability. The relative standard deviations of mean velocities from repeated trials in the test nozzle were on the order of 1% or less. So the projected resolution and precision of the proposed system seem adequate to meaningfully and reproducibly classify aerosols in the 0.5 μm to 10 μm range. As D_a increases, the precision and resolution expressed as a percent of the value measured should decrease.

5.6.2 Accuracy in the Case of Unknown Density

In the case of unknown particle density ranging from 1 to 3 g/cm^3, it is possible to assign a value of D_a based on the behavior of aerosol with a density of 2 g/cm^3. The error associated with this assignment increases with D_a and is negligible at the lower end of the diameter ranges for both proposed values of U_e.

The limits of the uncertainty can be estimated by noting the variation in D_a at a given velocity for aerosols with $\rho' = 1$, 2 and 3 g/cm^3. In the case with $U_e = 9500$ cm/s, the maximum uncertainty at 2 μm is on the order of ±.05 μm; at 10 μm, it approaches -1 μm and +.4 μm. In the case of $U_e = 1200$ cm/s, the maximum uncertainty is on the order of -.6 μm and +.2 μm at 11 μm.

5.6.3 Count Statistics and Probability of Coincidence

For $U_e = 9500$ cm/s, the maximum aerosol sample flow rate is 2.2 lpm. For the $U_e = 1200$ cm/s case, the maximum sample flow rate is .28 lpm. Using models developed at the University of Minnesota to indicate typical aerosol number distributions, it is possible to evaluate the counting statistics which result from these flows. A portion of two models is given in Table 5.3 (Whitby and Sverdrup, 1978). Table 5.4 shows concentrations and counts per minute expected in clean background and average urban conditions for size ranges at the upper and lower limit covered by the instrument.

The relative standard deviation in counts registered by a counter sampling random events is given by:

Table 5.3 Number distribution for tri-modal models of atmospheric aerosol

Interval Boundaries D_p, μm	Number in Each Size Interval, Number/cm^3	
	Clean Background	Average Urban
.100		
	161	43200
.178		
	58.0	20900
.316		
	11.6	275
.562		
	1.44	29.7
1.00		
	.264	3.00
1.78		
	.107	.749
3.16		
	.0336	.211
5.62		
	.00634	.0381
10.0		
	.000702	.00404
17.8		

Table 5.4 Concentrations and counts per minute in clean background and average urban conditions

	Diameter Range µm	Clean Background	Urban Average
Typical Concentration Particles/cm^3	.562- 1.	1.4	30.
	5.62 -10.	.006	.04
Counts/Minute U_e = 9500 cm/s	.562- 1.	3100.	66 x 10^3
	5.62 -10.	13.	88
Counts/Minute U_e = 1200 cm/s	.562- 1.	390.	8400.
	5.62 -10.	1.7	11.2

$$\sigma_r = n^{-1/2} \tag{5.1}$$

where n is the number of counts and σ_r, the relative standard deviation. So 100 counts are necessary to obtain a 10% relative standard deviation, and 1000 counts, to obtain a 3% relative standard deviation.

For the U_e = 9500 cm/s case, slightly more than one minute would be required to sample sufficient large particles in an average urban atmosphere to produce a σ_r of 10%. A ten-minute sampling time would be required in a clean background to produce a σ_r of 10% for large particles. Sample times of one minute and ten minutes are reasonable and a σ_r of 10% is acceptable. So U_e = 9500 cm/s provides adequate aerosol sample flow for atmospheric measurements. Count rates provided for large particles in the U_e = 1200 cm/s case are too low to be practical except in the case of extremely polluted atmospheres.

And so the decreased uncertainty in sizing larger particles obtained by reducing the gas velocity is balanced by increased counting uncertainty when sampling real atmospheric aerosols.

The measuring volume must be small enough so that the probability of finding two or more particles in the measuring volume at the same time is small. The result of such coincidences would most likely be the loss of counts, since laser-Doppler frequency counters like the one used in this experiment are often designed to reject signals which have been phase- or frequency-shifted sometime during the count. The frequency counter used in the experiment counted eight fringes. With a 10 μm fringe spacing and allowing the aerosol flow to cover .7 of the nozzle radius, the measuring volume is 3.1×10^{-5} cm^3. The probability of coincidence of particles in the viewing volume can be estimated using the Poisson distribution (Willeke and Liu, 1976). The probability, S_p, that p particles are present at the same time in a volume V is:

$$S_p = \frac{(NV)^p \, e^{-NV}}{p!} \tag{5.2}$$

where N is the number of particles per unit volume. Choosing N as 300 particles/cm^3, which is ten times greater than the concentration expected in an urban atmosphere in the diameter range between .562 μm and 10 μm, Equation (5.2) predicts the following results for the measuring volume given above.

Table 5.5 Probability, S_p, of finding p particles in the measuring volume

p	S_p
0.	.991
1	.00921
2	.0000428

The calculation does not account for the dynamic processes in the measuring volume such as the smaller particles overtaking the larger ones. However, it does give an estimate of the probability of coincidence. Table 5.7 implies that the number of particles passing through with one other particle will be about 1% of the number passing through alone. It is possible that particles in the size range just below the .5 μm boundary might scatter enough light to start the counter. Thus the above calculation is probably too optimistic. Nonetheless, the problem of coincidences should not be a serious one for the proposed set-up.

5.7 Conclusion

In this chapter, a design study of an instrument for aerodynamic particle sizing of atmospheric aerosols has been done. A nozzle geometry, two flow rates, a measuring position and fringe spacing have been proposed and studied. Using the higher flow rate, the σ_{gs} for the size distribution indicated for a .5 μm PSL aerosol is expected to be about 1.12; the maximum uncertainty due to density ranging from 1 to 3 g/cm^3 should occur at 10 μm and should be +.4 μm and -1 μm;

the sample flow rate is adequate to provide 100 counts in ten minutes in the 5 to 10 μm range in a clean background, and the measuring volume is small enough to avoid serious coincidence problems in a polluted urban atmosphere.

However, the Re_p experienced by 10 μm particles is on the order of 50, and thus exceeds the limit discussed in Chapter 4 for measuring the aerodynamic size of disc-like particles. However, for more gently-rounded particles, the aerodynamic sizes remain valid.

To improve the aerodynamic sizing of irregular particles and to reduce the uncertainty due to density, a second flow rate was proposed. In this case, the largest particle Reynolds number is 10 and the maximum uncertainty due to density variation is reduced to -.6 μm and +.2 μm at 10 μm. However, the aerosol sample flow rate is only .28 lpm, which is too small for routine atmospheric studies. Unfortunately, it seems unlikely that all of this can be accomplished with 5 mw of laser power, since in the experimental study, 5 mw of laser power spread over a viewing volume .07 cm in diameter was insufficient to size submicron aerosols.

CHAPTER 6

SUMMARY AND CONCLUSIONS

The object of this thesis was to study a means of measuring aerodynamic particle diameter in the range from .5 μm to 10 μm employing a nozzle and a laser-Doppler velocimeter.

It was shown experimentally that particles accelerated along the center streamline in a converging nozzle leave the nozzle with a velocity which depends upon particle size and flow rate. It was also demonstrated that the particle velocity can be measured with a high degree of repeatability using a laser-Doppler velocimeter, and that the velocity distributions measured for nearly monodisperse test aerosols are usually quite narrow. These results indicated that the method has promise and suggested broader studies aimed at enabling an intelligent choice of nozzle geometry and flow rate.

Theoretical studies involved predicting the flow in the nozzle and calculating the resulting particle velocity from the equation of particle motion. The theory was first tested by calculating the particle velocities expected under the conditions observed in the experiments. The theory treats only incompressible flows. The agreement between theory and experiment was found to be very good.

Using the validated theory, it was possible to investigate the effect on particle velocity of nozzle size and shape, flow rate, particle diameter and density, and position of the point of measurement. The use of dimensionless variables gave added generality to the calculations. It was learned that aerodynamic diameter is the principal factor in determining the velocity of a particle in a given nozzle and flow. But the particle density also plays a role. In terms of the dimensionless variables, Stokes number, St, determines the dimensionless particle velocity in a given nozzle as long as the particle Reynolds number, Re_p, is small. Aerodynamic diameter can be determined from St. However, at larger values of Re_p, a Reynolds number based on particle diameter, Re, becomes increasingly important, and both Re and St are needed to determine dimensionless particle velocity. In this case, particle density as well as aerodynamic diameter affect the particle velocity. But by judicious choice of flow conditions, it is possible to minimize the role of Re, and hence, particle density, in determining the velocity of the particle near the nozzle exit. Thus, particle velocity can be a good measure of St, and hence, aerodynamic diameter.

It was also determined that increasing the cone angle and moving the point of measurement closer to the nozzle increased the slope of the dimensionless velocity vs. aerodynamic diameter curve for smaller particles. Similarly, increasing the flow rate increases this slope, as does decreasing the nozzle exit diameter.

Using the results of the theoretical analysis, a nozzle geometry, measuring point and flow rate were chosen for the study of atmospheric aerosols. The intent was to provide adequate resolution for submicron particles, minimize the effect of particle density for larger particles, and provide adequate sample flows to allow collection of meaningful data over the entire range. The nozzle has not been tested experimentally.

It is possible to conclude that under proper conditions, the aerodynamic diameter of a particle can be determined with acceptable uncertainty from its velocity as it emerges from a nozzle. The laser-Doppler velocimeter provides a means of determining this velocity.

In order to produce a practical instrument, additional work needs to be done. An efficient sampling inlet is needed, a compact, cost-effective electronics package to provide reliable frequency counting and data analysis must be developed, and an optical system allowing the use of a reasonably-priced, reasonably-sized laser is necessary.

BIBLIOGRAPHY

Adrian, R. J., and Goldstein, R. J. (1971), "Analysis of a Laser-Doppler Anemometer", Journal of Physics E: Scientific Instruments 4:505-511.

Agarwal, J. (1975), Personal communication.

Berglund, R. N., and Liu, B. Y. H. (1973), "Generation of Monodisperse Aerosol Standards", Environ. Sci. Technol. 7:147-153.

Chabay, I., and Bright, D. S. (1977), "Measurement of the Size Distribution of Liquid and Solid Aerosols by Doppler Shift Spectroscopy", to be published in J. Colloid Interface Sci. as part of proceedings of ACS Symposium on Light Scattering, New Orleans, March, 1977.

Dahneke, B. (1973), "Aerosol Beam Spectrometry", Nature: Physical Science 244:54-55.

Dahneke, B. (1974), "Aerosol Beam Device and Method", U. S. Patent No. 3854321.

Dahneke, B. and Flachsbart, H. (1972), "An Aerosol Beam Spectrometer", J. Aerosol Sci. 3:345-349.

Durst, F., Melling, A., and White Daw, J. H. (1976), Principles and Practice of Laser-Doppler Anemometry, Academic Press, New York.

Friedlander, S. K. (1977), Smoke, Dust and Haze: Fundamentals of Aerosol Behavior, John Wiley and Sons, New York.

Frisch, M., and Hotchkiss, R. L. (1965), Runge-Kutta differential equation solver with variable integration step and automatic error control, University Computer Center, University of Minnesota, Minneapolis, MN.

Fuchs, N. A. (1964), The Mechanics of Aerosols, Pergamon Press, Oxford.

Gebhart, J., Heyden, J., Roth, C., and Stahlhofen, W. (1976), "Optical Size Spectrometry Below and Above the Wavelength of Light - A Comparison", in Fine Particles: Aerosol Generation, Measurement, Sampling, and Analysis (B. Y. H. Liu, ed.), Academic Press, New York.

Gollub, J. P., Chabay, I., and Flygare, W. H. (1974), "Laser Heterodyne Study of Water Droplet Growth", J. Chemical Phys. 61:2139-2144.

Gosman, A. D., Pun, W. M., Runchal, A. K., Spalding, D. B., and Wolfshtein, M. (1969), Heat and Mass Transfer in Recirculating Flows, Academic Press, New York.

Happel, J., and Brenner, H. (1965), Low Reynolds Number Hydrodynamics, Prentice Hall, Englewood Cliffs, NJ.

Hornbeck, R. W. (1963), "Laminar Flow in the Entrance Region of a Pipe", Appl. Sci. Res. Sect. A 13:224-232.

Kirsch, K. J., and Mazumder, M. K. (1975), "Aerosol Size Spectrum Analysis using Relaxation Time Measurement", Appl. Phys. Letters 26:193-195.

Knollenberg, R. G., and Luer, R. (1976), "Open Cavity Laser 'Active' Scattering Particle Spectrometry from 0.05 to 5 Microns", in Fine Particles: Aerosol Generation, Measurement, Sampling, and Analysis (B. Y. H. Liu, ed.), Academic Press, New York.

Landau, L. D., and Lifshitz, E. M. (1959), Fluid Mechanics, Pergamon Press, London.

Liu, B. Y. H. (1976), "Standardization and Calibration of Aerosol Instruments", in Fine Particles: Aerosol Generation, Measurement, Sampling, and Analysis (B. Y. H. Liu, ed.), Academic Press, New York.

Liu, B. Y. H. (1976a), Lecture notes.

Liu, B. Y. H., Marple, V. A., Whitby, K. T., and Barsic, N. J. (1974), "Size Distribution Measurement of Airborne Coal Dust by Optical Particle Counters", Am. Ind. Hyg. Assoc. J. 8:443-451.

Marple, V. A., and Liu, B. Y. H. (1974), "Characteristics of Laminar Jet Impactors", Environ. Sci. Technol. 8:648-654.

Marple, V. A., and Rubow, K. L. (1976), "Aerodynamic Particle Size Calibration of Optical Particle Counters", J. Aerosol Sci. 7:425-433.

Patankar, S. V., and Spalding, B. D. (1970), Heat and Mass Transfer in Boundary Layers, 2nd Edition, Intertext Books, London.

Raabe, O. G. (1976), "Aerosol Aerodynamic Size Conventions for Inertial Sampler Calibration", J. Air Pollut. Control Assoc. 26:856-860.

Schlichting, H. (1968), Boundary-Layer Theory, 6th Edition, McGraw-Hill, New York.

Schwartz, M. H., and Andres, R. P. (1976), "Theoretical Basis of the Time of Flight Aerosol Spectrometer: A Method for Monitoring the Size Distribution of Submicron Aerosol Particles", J. Aerosol Sci. 7:281-296.

Skow, M. M., and Hotchkiss, R. L. (1963), "Aitken's Method Interpolation", University Computer Center, University of Minnesota, Minneapolis, MN.

Sparrow, E. M., Baliga, B. R., and Patankar, S. V. (1977), "Heat Transfer and Fluid Flow Analysis of Interrupted-Wall Channels, with Application of Heat Exchangers", J. Heat Transfer, 99 Series C:4-11.

Stöber, W. (1976), "Design, Performance, and Applications of Spiral Duct Aerosol Centrifuges", in Fine Particles: Aerosol Generation, Measurement, Sampling, and Analysis (B. Y. H. Liu, ed.), Academic Press, New York.

Task Group on Lung Dynamics of International Commission on Radiological Protection (1966), "Deposition and Retention Models for Internal Dosimetry of Human Respiratory Tract", Health Physics 12:173-207.

Thermo-Systems, Inc., Instruction Manual, 900 Series Laser Optics, P. O. Box 3394, St. Paul, MN 55165.

Thermo-Systems, Inc., Laser Anemometer Systems from Thermo-Systems, Inc., P. O. Box 3394, St. Paul, MN 55165.

Weast, R. C. (Ed.) (1976), Handbook of Chemistry and Physics, 57th Edition, CRC Press, Cleveland.

Whitby, K. T., Clark, W. E., Marple, V. A., Sverdrup, G. M., Sem, G. J., Willeke, K., Liu, B. Y. H., and Pui, D. Y. H. (1975), "Characterization of California Aerosols - I. Size Distributions of Freeway Aerosols", Atmos. Environ. 9:463-482.

Whitby, K. T., and Cantrell, B. K. (1975), "Atmospheric Aerosols - Characteristics and Measurement", Institute of Electrical and Electronics Engineers, Inc., International Conference on Environmental Sensing and Assessment, Las Vegas, NV, September, 1975.

Whitby, K. T., and Sverdrup, G. M. (1978), "California Aerosols: Their Physical and Chemical Characteristics", Hutchinson Memorial Volume on the ACHEX studies in California, to be published as Advances in Environmental Sciences and Technology, early 1978.

Whitby, K. T., and Willeke, K. (1976), "Single Particle Optical Counters: Principles and Field Use", presented at Aerosol Measurement Workshop, University of Florida, Gainesville, FL, March, 1976.

Willeke, K., and Liu, B. Y. H. (1976), "Single Particle Optical Counter: Principle and Application", in Fine Particles: Aerosol Generation, Measurement, Sampling, and Analysis (B. Y. H. Liu, ed.), Academic Press, New York.

Yanta, W. (1973), "Measurements of Aerosol-Size Distributions with a Laser-Doppler Velocimeter", presented at AIAA 6th Fluid and Plasma Dynamics Meeting, Palm Springs, CA, July, 1973.

APPENDIX A

DERIVATION OF A FINITE DIFFERENCE EQUATION FOR THE CALCULATION OF FLUID FLOW IN A NOZZLE USING THE BOUNDARY LAYER APPROXIMATION

A.1 Introduction

This Appendix expands the discussion found in Section 3.2.2. In that section, the general principles of the boundary layer calculation of fluid velocity in the nozzle are presented. In this appendix, more detail is discussed concerning the finite difference equations.

Patankar and Spalding (1970) derive a partial differential equation (PDE) which describes the transfer of mass, momentum and stagnation enthalpy in a boundary layer. They transform that equation to a finite difference equation (FDE) and present a computer program which solves the FDE in axisymmetric or plane geometries with free or fixed boundaries. Program BNDARL, used in this study, is very similar to that described by Patankar and Spalding but differs in some ways. The treatment of the equation near the boundaries and the velocity profile used to calculate the radial positions are simplified in BNDARL. In addition, the treatment of the pressure gradient in confined flows has been modified in BNDARL. This last modification is discussed in Sparrow et al. (1977) and will not be dealt with here.

The object of this appendix is to illustrate the derivation of an FDE from a PDE, that is, to show how to get from Equation (3.7) to Equation (3.8); to show how the equations are treated near the boundaries and how the radial positions of the nodes are calculated. However, the full generality of BNDARL will not be illustrated here. In scope and utility, it is very similar to the program described by Patankar and Spalding. In this discussion, only the velocity equation will be considered, and the simplifications implied by the geometry and boundary conditions of the present problem will be made. Thus, the equations derived here do not appear as statements in Program BNDARL, but the method shown here illustrates that used by Patankar and Baliga (see Sparrow et al., 1977) in writing the program. This discussion is based on information supplied by Baliga in personal communications.

A.2 The Partial Differential Equation

Equation (3.7) is a particular example of the PDE treated in BNDARL. The general equation is:

$$\frac{1}{(\Psi_E-\Psi_I)}\frac{\partial}{\partial x}[(\Psi_E-\Psi_I)\Phi] + \frac{\partial}{\partial\omega}[(a+b\omega)\Phi] = \frac{\partial}{\partial\omega}\left(e\frac{\partial\Phi}{\partial\omega}\right) + d \qquad (A.1)$$

Ψ and ω are defined in Equations (3.6). Φ is either fluid velocity, mass or stagnation enthalpy. The transfer coefficients are included in e, and the mass flux across the interior and exterior boundaries are included in a and b. The source term is given by d. In the case of Equation (3.7),

$$d = -\frac{1}{\rho u}\frac{dP}{dx} \qquad (A.2)$$

$$e = \frac{r^2\rho u\mu}{(\Psi_E-\Psi_I)^2} \qquad (A.3)$$

The problem solved in this investigation is the flow in a nozzle; therefore, the interior boundary is the center streamline and the exterior boundary of the calculation is the wall. Thus, a and b vanish and $(\Psi_E-\Psi_I)$ is a constant for a given flow. The first term in Equation (A.1) is streamwise convection; the second vanishes in this case and is ω-direction convection; the third term is the ω-direction diffusion term. Patankar and Spalding give the definitions of e and d when Φ is mass or stagnation enthalpy, and discuss a and b for cases where fluid is entrained at a free boundary or mass crosses the boundaries.

In the present case, Equation (A.1) reduces to:

$$\frac{\partial u}{\partial x} - \frac{\partial}{\partial \omega}\left(\frac{r^2\rho u\mu}{(\Psi_E-\Psi_I)^2}\frac{\partial u}{\partial \omega}\right) + \frac{1}{\rho u}\frac{dP}{dx} = 0 \qquad (A.4)$$

where u is the fluid velocity parallel to the center streamline and r is the distance from that streamline.

A.3 The Grid

It is explained in Chapter 3 that this equation is solved in x-ω space. For flow in the nozzle, x corresponds to distance along the axis and ω varies from 0 on the center streamline to 1 on the wall. The nodes shown in Figure 3.1 correspond to the points in (x-ω) space for which values of u will be obtained. After obtaining values of u, values of the radial coordinate r will also be obtained for each (x-ω) pair. Of course, the ω=1 points are fixed on the walls of the nozzle and ω=0 points are fixed on the axis. The calculation of values of r at the (x,ω) nodes allows the distribution of the values of stream function in (x,r) space. Figure A.1a shows two lines of nodes stretching from the center streamline to the wall, and indicates the boundaries of the control volumes. At the boundaries, the first control volume extends from the boundary to between the second and third nodes. Typical control volumes at the boundaries and between them are indicated by the shading. The node at the wall is indicated by M3 and its neighbor is M2. The half-integers refer to the boundaries of the control volumes.

The solution starts at an initial value of x and sweeps downstream to subsequent values in a once-through marching procedure. Therefore, one interval in x suffices to illustrate the equations. The values of r and u are known then for all nodes at $x-\Delta x$ and are sought for the nodes at x. Quantities at $x-\Delta x$ are indicated with a U subscript; those at x, with a D.

A.4 The Finite Difference Equation

Each term in Equation (A.4) is integrated over a control volume from $x-\Delta x$ to x, and from $\omega_{i-\frac{1}{2}}$ to $\omega_{i+\frac{1}{2}}$. The integral of the first term, indicated by (1), is evaluated assuming a velocity profile of the type indicated in Figure A.1b. The width of the interior control volume in the ω-direction is taken to be $(\omega_{i+1}-\omega_{i-1})/2$. Thus,

$$(1) = (u_{iD}-u_{iU})\,\frac{(\omega_{i+1}-\omega_{i-1})}{2} \qquad \text{(A.5)}$$

The integral of the second term in Equation (A.4) is indicated by (2). The ω-derivative in this form is evaluated in terms of

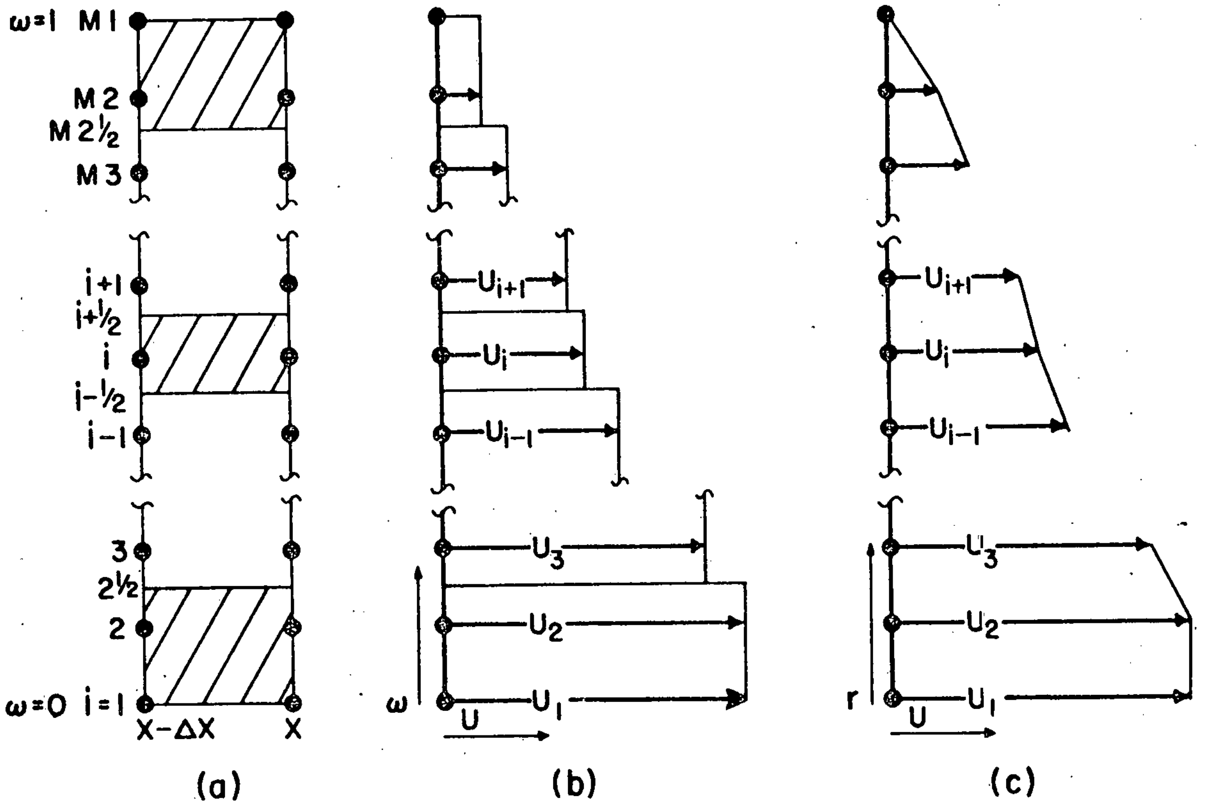

Figure A.1 Nodes, control volumes, and profiles for the finite different equation.

downstream values of u. This is referred to as a fully implicit treatment and is discussed by Patankar and Spalding, who relate it to the stability of the method. Thus, the x-integration reduces to a multiplication by Δx, and the ω integration produces:

$$(2) = \Delta x \int_{i-\frac{1}{2}}^{i+\frac{1}{2}} \frac{\partial}{\partial\omega}\left(e\,\frac{\partial u}{\partial\omega}\right) \partial\omega = \Delta x\left[e\,\frac{\partial u}{\partial\omega}\bigg|_{i+\frac{1}{2}} - e\,\frac{\partial u}{\partial\omega}\bigg|_{i-\frac{1}{2}}\right]_D \qquad (A.6)$$

Equations (3.6) allow the transformation from derivatives in ω to derivatives in r, where

$$\frac{\partial}{\partial\omega} = \frac{(\Psi_E-\Psi_I)}{\rho u r}\,\frac{\partial}{\partial r} \qquad (A.7)$$

Introducing the definition of e and transforming to derivatives in r, (2) becomes:

$$(2) = \frac{\mu\Delta x}{(\Psi_E-\Psi_I)}\left[\left(r\,\frac{\partial u}{\partial r}\right)_{i+\frac{1}{2}} - \left(r\,\frac{\partial u}{\partial r}\right)_{i-\frac{1}{2}}\right]_D \qquad (A.8)$$

In this case, μ is constant and is taken out of the parenthesis. A linear profile with radius is assumed between adjacent nodes for u, as is indicated in Figure A.1c. Therefore, (2) becomes:

$$(2) = \frac{\mu\Delta x}{(\Psi_E-\Psi_I)}\left[\left(\frac{r_{i+\frac{1}{2}}}{r_{i+1}-r_i}\right)_U (u_{i+1}-u_i)_D - \left(\frac{r_{i-\frac{1}{2}}}{r_i-r_{i-1}}\right)_U (u_i-u_{i-1})_D\right] \qquad (A.9)$$

Note that only the velocities are now evaluated at x. The values of r_D depend upon the values of u_D, so it is necessary to approximate r_D by r_U in order to maintain the linearity of the final equation.

The integral of the third term is also converted from an integral over ω to one over r. The derivative, dP/dx, is left explicitly in the equation as a reminder that is must be supplied, since Equation (A.4) does not provide sufficient information to determine the pressure gradient.

$$(3) = \Delta x \left[\int_{i-\frac{1}{2}}^{i+\frac{1}{2}} \frac{1}{\rho u} \frac{dP}{dx} d\omega \right]_D = \frac{\Delta x}{(\Psi_E - \Psi_I)} \left[\int_{i-\frac{1}{2}}^{i+\frac{1}{2}} \frac{dP}{dx} rdr \right]_D$$

$$= \frac{\Delta x}{(\Psi_E - \Psi_I)} \left(\frac{dP}{dx} \right)_D \left(\frac{r_{i+\frac{1}{2}}{}^2 - r_{i-\frac{1}{2}}{}^2}{2} \right)_U \qquad (A.10)$$

Again the coefficients of dP/dx are evaluated in terms of upstream values, and dP/dx is evaluated downstream. Gathering Equations (A.5), (A.9), and (A.10) allows the double integral of Equation (A.4) to be written in finite difference form:

$$a_i u_i = b_i u_{i+1} + c_i u_{i-1} + d_i + e_i \frac{dP}{dx} \qquad (3.8)$$

where

$$a_i = \left(\frac{\omega_{i+1} - \omega_{i-1}}{2} \right) + \frac{\Delta x}{(\Psi_E - \Psi_I)} \left[\frac{r_{i+\frac{1}{2}}}{r_{i+\frac{1}{2}} - r_i} + \frac{r_{i-\frac{1}{2}}}{r_i - r_{i-1}} \right]$$

$$b_i = \frac{\Delta x}{(\Psi_E - \Psi_I)} \left[\frac{r_{i+\frac{1}{2}}}{r_{i+1} - r_i} \right]$$

$$c_i = \frac{\Delta x}{(\Psi_E - \Psi_I)} \left[\frac{r_{i-\frac{1}{2}}}{r_i - r_{i-1}} \right]$$

$$d_i = u_i \left(\frac{\omega_{i+1} - \omega_{i-1}}{2} \right)$$

$$e_i = - \frac{\Delta x}{(\Psi_E - \Psi_I)} \left(\frac{r_{i+\frac{1}{2}}^{\;2} - r_{i-\frac{1}{2}}^{\;2}}{2} \right) \qquad \text{(A.11)}$$

It must be remembered that all the terms in the coefficients, a_i, b_i, c_i, d_i, and e_i, are evaluated at the upstream position, and hence, are known when the calculations for the u_i, u_{i-1}, and u_{i+1} are done for the downstream position.

Equation (3.8), with the definitions in Equations (A.11), applies for i=3 through i=M3. The equations for i=2 and i=M2 differ slightly since these control volumes are adjacent to the boundaries. Figure A.1 illustrates some of the differences. For i=2, the term $r_{i-\frac{1}{2}}$ is replaced by zero, since the lower boundary of that control volume is at r=0. For i=M2, $r_{i+\frac{1}{2}}$ and r_{i+1} are set equal to r_{M1}. This means that the cross-stream derivatives are calculated from one side at the wall.

The values of u at i=1 and i=M1 are determined by the boundary conditions. In the nozzle, $u_{M1}=0$. The derivative of u at the center streamline also vanishes, and this condition is enforced by setting $u_1=u_2$.

Thus, there are as many linear equations as there are nodes, and provided that a value of dP/dt can be supplied, it is possible to solve for the u_i at x given the u_i and r_i at $x-\Delta x$.

As is indicated in Section 3.2.2, the information on dP/dx is provided by an iterative scheme involving Equations (3.8) and (3.10) and described by Sparrow et al.

A.5 Calculations of the Radial Positions of the Nodes

Once values of u are obtained for each node at a given x, it is necessary to determine the radial position of each node. And the positions of the interfaces between control volumes must be determined. Equations (3.6) imply that:

$$\int_0^{\omega} \frac{(\Psi_E-\Psi_I)}{\rho u}\, d\omega = \int_0^{r} r\,dr \qquad \text{(A.12)}$$

So to assign a value of r to each node, the integrals in Equation (A.12) are evaluated using a velocity profile like that shown in Figure A.1b. The left-hand side of Equation (A.12) becomes a summation, and the right-hand side equals $r^2/2$. In order to follow the profile indicated in Figure A.1b, the value of $\rho_{i-1}u_{i-1}$ changes to $\rho_i u_i$ halfway between the i-1 and i nodes.

$$\frac{r_i^{\,2}}{2} = \frac{(\Psi_E-\Psi_I)}{\rho}\left[\frac{\omega_2-\omega_1}{u_2} + \sum_3^{i}\frac{\omega_i-\omega_{i-1}}{2}\left(\frac{1}{u_i}+\frac{1}{u_{i-1}}\right)\right] \qquad \text{(A.13)}$$

where the density of the fluid is treated as a constant, as is the current case.

The values of r at the interfaces, $r_{i+\frac{1}{2}}$ or $r_{i-\frac{1}{2}}$, is determined by formula similar to (A.13), except that all the terms have the form $\left(\frac{\omega_i-\omega_{i-1}}{u_i}\right)$.

Having found the values of u_i, r_i, $r_{i+\frac{1}{2}}$ for each node at x, it is now possible to continue the calculation to x+Δx by forming Equation (3.8), etc., etc.

APPENDIX B

PROGRAM BNDARL FOR THE BOUNDARY-LAYER CALCULATIONS

B.1 Glossary of User Modified Terms

All dimensioned variables were expressed in cgs units.

Term	Statement Number	Significance
P	290	Sets initial pressure
M1	300	Index of last node point (maximum = 200)
M2, M3	300	M1-1, M1-2, respectively
IPLAX	310	Determines geometry IPLAX = 1 implies plane IPLAX = 2 implies axisymmetric
CSALFA	310	Cosine of the angle between inner boundary and axis of symmetry
R(1)	310	Radial position of first node point (for example, in coaxial flows)
KIN, KEX	310	KIN applies to the internal boundary KEX applies to the external boundary 1 implies wall; 2 implies free boundary; 3 implies axis of symmetry
RMI, RME	320	Product of radius and mass flux through internal and external boundaries
YM1	320	Initial radius of external surface
NL	330	Number of points given to determine nozzle outline
XX, YY	330	Points given to determine nozzle outline

Term	Statement Number	Significance
NFT	360	Number of equations (2 is minimum value. See 2100)
DELTAZ	360	Initial downstream step size (.00004 in this case)
INCRE1	360	Intervals at which detailed (PRINT 1) output is desired
INCRE2	360	Intervals at which brief (PRINT 2) output is desired
US	360	Mean velocity at inlet to nozzle (distribution calculated at statement 4180)
ISKIP	360	Index determines number of radial nodes to be skipped in printing of output (PRINT 1)
ISOLVE	370	Index determines whether equation is to be solved 1 implies solve, 2 implies do not solve (1,2 input in this case)
IPRIT	380	Index determines whether variable is to be printed 1 implies print (1,2 input in this case)
TITLE	390	Title of variables printed-out
OMEGA(J)	4060	Determines spacing of ω coordinates
RHO(J)	4170	Density of fluid
U(J)	4180	Initial velocity distribution
AMUU	4200	Viscosity
PEI	4210	Initial value of $\int \rho u r dr$
DXMULT	4220	Multiplies downstream step size on successive steps
DXMAX	4360	Sets maximum downstream step size

B.2 Listing of Program BNDARL

```
00100 PROGRAM BNDARL(INPUT,OUTPUT,F703,TAPE1=F703)
00110C
00120C     THIS IS THE MAIN PROGRAM
00130C
00140C
00150C      THIS IS THE COMMON BLOCK
00160C
00170 COMMON/COMA/OMEGA(200),TWOMD(200),CVWID(200),OMAV(200),COMAV(200)
00180+,M1,M2,M3,KIN,KEX,TITLE(6),IPRIT(6),X,RCVF(200),YCVF(200),AMUU
00190 COMMON/COMB/R(200),Y(200),RHO(200),PEI,IPLAX,CSALFA,F(200,6)
00200 COMMON/COMC/RADTYD(200),ALD2(200),RMI,RME,PCVWID(200),DELTAX,
00210+RCVWID(200),NF,NFT,YM1,PCORR,DPDX,ISKIP,P,V1(200),DELTAZ,US
00220 COMMON/COMD/ISOLVE(6),GAM(200),AJP(200),AJM(200),ACON(200),AP(200)
00230 COMMON/COME/INCRE1,INCRE2,XOUT,N,ITER,LSTOP,IPRT1,IPRT2,NITF
00240 COMMON/COMF/XOC(200),VOC(200),NOP,PO(200)
00250 COMMON/COMG/NL,XX(11),YY(11)
00260 DIMENSION U(200)
00270 EQUIVALENCE (U(1),F(1,1))
00280C
00290 DATA P,DPDX,PCORR/1.015E6,0.,0./
00300 DATA M1,M2,M3/91,90,89/
00310 DATA IPLAX,CSALFA,R(1),KIN,KEX/2,1.0,0.0,3,1/
00320 DATA RMI,RME,YM1/0.0,0.0,0.527/
00330 DATA NL,XX,YY/11,0.,1.58,1.661,1.67,1.677,1.684,1.691,1.701,
00340+1.706,1.712,1.77,.527,.0922,.067,.0644,.0625,.0606,.0589,
00350+.0566,.0559,.0552,.053/
00360 READ,NFT,DELTAZ,INCRE1,INCRE2,US,ISKIP
00370 READ,(ISOLVE(NF),NF=1,NFT)
00380 READ,(IPRIT(NF),NF=1,NFT)
00390 READ5,(TITLE(NF),NF=1,NFT)
00400 5 FORMAT(6A11)
00410 NOP=0
00420 CALL GRID
00430 CALL SETUP1
00440 CALL START
00450 CALL BOUND
00460 10 CALL SETUP2
00470 CALL OUTPUT
00480 IF(LSTOP.EQ.1)GOTO800
00490 CALL PRINT1
00500 CALL PRINT2
00510 WRITE(1,801)NOP
00520 801 FORMAT(I4)
00530 803 FORMAT(3(E13.6))
00540 DO 804 I=1,NOP
00550 804 WRITE(1,803)XOC(I),VOC(I),PO(I)
00560 STOP
00570 800 CONTINUE
00580 CALL XANDDX
00590 CALL BOUND
00600 CALL SETUP3
00610 ITER=ITER+1
00620 IF(X.GE.XX(NL))LSTOP=5
00630 GOTO10
00640 END
00650C
00660C    SUBROUTINE   SETUP
00670C
00680 SUBROUTINE SETUP
```

```
00690 COMMON/COMA/OMEGA(200),TWOMD(200),CVWID(200),OMAV(200),COMAV(200)
00700+,M1,M2,M3,KIN,KEX,TITLE(6),IPRIT(6),X,RCVF(200),YCVF(200),AMUU
00710 COMMON/COMB/R(200),Y(200),RHO(200),PEI,IPLAX,CSALFA,F(200,6)
00720 COMMON/COMC/RADTYD(200),ALD2(200),RMI,RME,PCVWID(200),DELTAX,
00730+RCVWID(200),NF,NFT,YM1,PCORR,DPDX,ISKIP,P,V1(200),DELTAZ,US
00740 COMMON/COMD/ISOLVE(6),GAM(200),AJP(200),AJM(200),ACON(200),AP(200)
00750 COMMON/COME/INCRE1,INCRE2,XOUT,N,ITER,LSTOP,IPRT1,IPRT2,NITF
00760 DIMENSION U(200)
00770 EQUIVALENCE (U(1),F(1,1))
00780 DIMENSION TDMA1(200),TDMA2(200)
00790C
00800C     SUBROUTINE SETUP1: COMPUTES ONCE FOR ALL QUANTITIES
00810C
00820 ENTRY SETUP1
00830 DO 10 I=3,M2
00840 TWOMD(I)=(OMEGA(I)-OMEGA(I-1))/2.
00850 OMAV(I)=(OMEGA(I)+OMEGA(I-1))/2.
00860 COMAV(I)=1.-OMAV(I)
00870 10 CVWID(I)=(OMEGA(I+1)-OMEGA(I-1))/2.
00880 TWOMD(2)=OMEGA(2)-OMEGA(1)
00890 TWOMD(M1)=OMEGA(M1)-OMEGA(M2)
00900 CVWID(2)=(OMEGA(3)+OMEGA(2))/2.-OMEGA(1)
00910 CVWID(M2)=OMEGA(M1)-(OMEGA(M2)+OMEGA(M3))/2.
00920 OMAV(2)=OMEGA(1)
00930 COMAV(2)=1.-OMAV(2)
00940 OMAV(M1)=OMEGA(M1)
00950 COMAV(M1)=1.-OMAV(M1)
00960 Y(1)=0.0
00970 RCVF(1)=R(1)
00980 GO TO(20,40)IPLAX
00990 20 DO 30 I=1,M1
01000 RCVF(I)=1.
01010 30 R(I)=1.
01020 GOTO35
01030 40 YM1=R(1)*YM1+YM1*YM1*CSALFA/2.
01040 35 RETURN
01050C
01060C    SUBROUTINE SETUP2: COMPUTES Y'S AND R'S
01070C
01080C
01090 ENTRY SETUP2
01100C
01110C    CALCULATION OF Y'S FOR PLANE GEOMETRY
01120C
01130 IF((ITER.LE.0).OR.((KIN.EQ.2).OR.(KEX.EQ.2)))GOTO41
01140 NIT=0
01150 560 CONTINUE
01160 SUM1=0.0
01170 SUM2=0.0
01180 DO 42 J=2,M2
01190 SJ=CVWID(J)/RHO(J)/U(J)
01200 V2=SJ*V1(J)/U(J)
01210 SUM1=SUM1+SJ
01220 42 SUM2=SUM2+V2
01230 PCORR=(SUM1-YM1/PEI)/SUM2
01240 DPDX=PCORR+DPDX
01250 FAMX=0.0
01260 DO 520 J=2,M2
01270 FACTOR=V1(J)*PCORR/U(J)
01280 FAMX=AMAX1(FAMX,ABS(FACTOR))
01290 520 U(J)=U(J)*(1.0+FACTOR)
01300 IF(NIT.GT.NITF)GOTO530
01310 IF(FAMX.LT.0.000001)GOTO570
01320 NIT=NIT+1
01330 GOTO560
01340 530 PRINT580,X,FAMX
```

```
580 FORMAT(/1X,*AT X=*,1PE12.5,2X,*NIT=NITF;FMAX =*,1PE12.5)
570 CONTINUE
P=P+DPDX*DELTAX
GOTO(48,48,47)KIN
47 F(1,1)=F(2,1)
48 IF(KEX.EQ.3)F(M1,1)=F(M2,1)
41 YCVF(2)=0.0
45 Y(2)=TWOMD(2)*PEI/(RHO(2)*U(2))
DO 50 I=3,M2
YCVF(I)=YCVF(I-1)+CVWID(I-1)/RHO(I-1)/U(I-1)*PEI
50 Y(I)=Y(I-1)+PEI*TWOMD(I)*(1./(RHO(I-1)*U(I-1))+1./(RHO(I)
+*U(I)))
YCVF(M1)=YCVF(M2)+CVWID(M2)/RHO(M2)/U(M2)*PEI
Y(M1)=Y(M2)+TWOMD(M1)*PEI/(RHO(M2)*U(M2))
GOTO(120,60)IPLAX
C
C    Y'S AND R'S FOR AXISYMMETRICAL GEOMETRY
C
60 IF(CSALFA.EQ.0.)GOTO100
C    CSALFA NE ZERO
COSD2=.5*CSALFA
IF(R(1).NE.0.)GOTO80
C
C             R(1)=0.
C
DO 70 I=2,M1
Y(I)=SQRT(Y(I)/COSD2)
YCVF(I)=SQRT(YCVF(I)/COSD2)
RCVF(I)=YCVF(I)*CSALFA
70 R(I)=Y(I)*CSALFA
GOTO120
C
C     R(1) NE ZERO
C
80 R1D2=.5*R(1)
R1D2SQ=R1D2*R1D2
DO 90 I=2,M1
Y(I)=Y(I)/(R1D2+SQRT(R1D2SQ+Y(I)*COSD2))
YCVF(I)=YCVF(I)/(R1D2+SQRT(R1D2SQ+YCVF(I)*COSD2))
RCVF(I)=R(1)+YCVF(I)*CSALFA
90 R(I)=R(1)+Y(I)*CSALFA
GOTO120
C
C        CSALFA EQ ZERO
C
100 DO 110 I=2,M1
Y(I)=Y(I)/R(1)
YCVF(I)=YCVF(I)/R(1)
RCVF(I)=R(1)
110 R(I)=R(1)
120 RETURN
C
C  SUBROUTINE SETUP3: COMPUTES RADTYD'S,RCVWID'S,PCVWID'S,ALD2'S
C
ENTRY SETUP3
DO 130 I=3,M3
RADTYD(I)=RCVF(I)/(Y(I)-Y(I-1))/2.
ALD2(I)=(COMAV(I)*RMI+OMAV(I)*RME)/2.
RCVWID(I)=(RCVF(I+1)+RCVF(I))*(YCVF(I+1)-YCVF(I))/2.
130 PCVWID(I)=PEI/DELTAX*CVWID(I)
RADTYD(2)=RCVF(2)/Y(2)
RADTYD(M2)=RCVF(M2)/(Y(M2)-Y(M3))/2.
RADTYD(M1)=RCVF(M1)/(Y(M1)-Y(M2))
ALD2(2)=(COMAV(2)*RMI+OMAV(2)*RME)/2.
ALD2(M2)=(COMAV(M2)*RMI+OMAV(M2)*RME)/2.
ALD2(M1)=(COMAV(M1)*RMI+OMAV(M1)*RME)/2.
```

```
RCVWID(2)=(RCVF(3)+RCVF(2))*(YCVF(3)-YCVF(2))/2.
RCVWID(M2)=(RCVF(M1)+RCVF(M2))*(YCVF(M1)-YCVF(M2))/2.
PCVWID(2)=PEI/DELTAX*CVWID(2)
PCVWID(M2)=PEI/DELTAX*CVWID(M2)
V1(1)=0.0
V1(M1)=0.0
C
C     ALGORITHM TO COMPUTE THE NEW F'S
C
DO 140 NF1=2,NFT
NF=NF1
145 CONTINUE
GOTO(150,144)ISOLVE(NF)
C
C   COMPUTATION OF THE COEFFICIENTS IN THE F.D.E'S
C
150 CALL GAMMA
CALL SOURCE
GOTO(170,160,160)KIN
160 GAM(1)=0.0
170 GOTO(190,180,180)KEX
180 GAM(M1)=0.0
190 TJP=GAM(1)*RADTYD(2)
TJP=AMAX1(TJP,ABS(ALD2(2)))
DO 200 J=2,M3
TJM=TJP
TJP=(GAM(J)+GAM(J+1))*RADTYD(J+1)
TJP=AMAX1(TJP,ABS(ALD2(J+1)))
AJP(J)=TJP-ALD2(J+1)
AJM(J)=TJM+ALD2(J)
ACON(J)=PCVWID(J)*F(J,NF)+ACON(J)*RCVWID(J)
200 AP(J)=AJP(J)+AJM(J)+PCVWID(J)-AP(J)*RCVWID(J)
TJM=TJP
TJP=GAM(M1)*RADTYD(M1)
TJP=AMAX1(TJP,ABS(ALD2(M1)))
AJP(M2)=TJP-ALD2(M1)
AJM(M2)=TJM+ALD2(M2)
ACON(M2)=PCVWID(M2)*F(M2,NF)+ACON(M2)*RCVWID(M2)
AP(M2)=AJP(M2)+AJM(M2)+PCVWID(M2)-AP(M2)*RCVWID(M2)
C
C     THE EQUATION SOLVING SEQUENCE
C
C    CALCULATION OF THE TDMA COEFFICIENTS
C
TDMA1(1)=0.0
TDMA2(1)=F(1,NF)
DO 210 J=2,M2
DENOM=AP(J)-AJM(J)*TDMA1(J-1)
TDMA1(J)=AJP(J)/DENOM
IF((KIN.EQ.2).OR.(KEX.EQ.2))GOTO210
IF(NF.EQ.1)V1(J)=(AJM(J)*V1(J-1)-RCVWID(J))/DENOM
210 TDMA2(J)=(AJM(J)*TDMA2(J-1)+ACON(J))/DENOM
C
C     COMPUTATION OF THE NEW F'S
410 DO 220 I=2,M2
J=M1+1-I
IF((KIN.EQ.2).OR.(KEX.EQ.2))GOTO220
IF(NF.EQ.1)V1(J)=TDMA1(J)*V1(J+1)+V1(J)
220 F(J,NF)=TDMA1(J)*F(J+1,NF)+TDMA2(J)
IF((KIN.EQ.2).OR.(KEX.EQ.2))GOTO144
IF(KIN.NE.3)GOTO240
F(1,NF)=F(2,NF)
240 IF(KEX.NE.3)GOTO250
F(M1,NF)=F(M2,NF)
250 CONTINUE
144 IF(NF.NE.NFT.OR.NF.EQ.1)GOTO140
```

```
 NF=1
 GOTO145
 140 CONTINUE
 RETURN
 END
C
C      SUBROUTINE GAMMA: COMPUTES THE EXCHANGE COEFFICIENTS
 SUBROUTINE GAMMA
C
C      THIS IS THE COMMON BLOCK
C
 COMMON/COMA/OMEGA(200),TWOMD(200),CVWID(200),OMAV(200),COMAV(200)
+,M1,M2,M3,KIN,KEX,TITLE(6),IPRIT(6),X,RCVF(200),YCVF(200),AMUU
 COMMON/COMB/R(200),Y(200),RHO(200),PEI,IFLAX,CSALFA,F(200,6)
 COMMON/COMC/RADTYD(200),ALD2(200),RMI,RME,PCVWID(200),DELTAX,
+RCVWID(200),NF,NFT,YM1,PCORR,DPDX,ISKIP,P,V1(200),DELTAZ,US
 COMMON/COMD/ISOLVE(6),GAM(200),AJP(200),AJM(200),ACON(200),AP(200)
 COMMON/COME/INCRE1,INCRE2,XOUT,N,ITER,LSTOP,IPRT1,IPRT2,NITF
 DIMENSION U(200)
 EQUIVALENCE (U(1),F(1,1))
C
 DO 10 J=1,M1
 GAM(J)=AMUU
 10 CONTINUE
 RETURN
 END
C
C     SUBROUTINE SOURCE: COMPUTES THE SOURCE TERMS
 SUBROUTINE SOURCE
C
C      THIS IS THE COMMON BLOCK
C
 COMMON/COMA/OMEGA(200),TWOMD(200),CVWID(200),OMAV(200),COMAV(200)
+,M1,M2,M3,KIN,KEX,TITLE(6),IPRIT(6),X,RCVF(200),YCVF(200),AMUU
 COMMON/COMB/R(200),Y(200),RHO(200),PEI,IFLAX,CSALFA,F(200,6)
 COMMON/COMC/RADTYD(200),ALD2(200),RMI,RME,PCVWID(200),DELTAX,
+RCVWID(200),NF,NFT,YM1,PCORR,DPDX,ISKIP,P,V1(200),DELTAZ,US
 COMMON/COMD/ISOLVE(6),GAM(200),AJP(200),AJM(200),ACON(200),AP(200)
 COMMON/COME/INCRE1,INCRE2,XOUT,N,ITER,LSTOP,IPRT1,IPRT2,NITF
 DIMENSION U(200)
 EQUIVALENCE (U(1),F(1,1))
C
 DO 10 J=2,M2
 GOTO(20,30)NF
 20 ACON(J)=-DPDX
 GOTO10
 30 ACON(J)=0.0
 10 AP(J)=0.0
 RETURN
 END
C
C
C    THIS IS THE PRINTING ALGORITHM
C
 SUBROUTINE PRINT
C
C      THIS IS THE COMMON BLOCK
C
 COMMON/COMA/OMEGA(200),TWOMD(200),CVWID(200),OMAV(200),COMAV(200)
+,M1,M2,M3,KIN,KEX,TITLE(6),IPRIT(6),X,RCVF(200),YCVF(200),AMUU
 COMMON/COMB/R(200),Y(200),RHO(200),PEI,IFLAX,CSALFA,F(200,6)
 COMMON/COMC/RADTYD(200),ALD2(200),RMI,RME,PCVWID(200),DELTAX,
+RCVWID(200),NF,NFT,YM1,PCORR,DPDX,ISKIP,P,V1(200),DELTAZ,US
 COMMON/COMD/ISOLVE(6),GAM(200),AJP(200),AJM(200),ACON(200),AP(200)
 COMMON/COME/INCRE1,INCRE2,XOUT,N,ITER,LSTOP,IPRT1,IPRT2,NITF
 COMMON/COMF/XOC(200),VOC(200),NOP,PO(200)
```

```
03330 DIMENSION U(200),I(6)
03340 EQUIVALENCE (U(1),F(1,1))
03350 ENTRY PRINT1
03360 PRINT5,ITER
03370 5 FORMAT(//*---------RESULTS OF STEP # *,I6,* ------*)
03380 PRINT10,X,R(1)
03390 10 FORMAT(///*  RESULTS AT X=*,1PE12.5,5X,*R(1) =*,1PE12.5)
03400 PRINT15,DPDX,PCORR,P
03410 15 FORMAT(/* DPDX=*,1PE12.5,5X,*PCORR =*,1PE12.5,*  P=*,1PE12.5,/)
03420 JOUT=5
03430 KOUT=1
03440 I(1)=1
03450 12 IF(I(1).LT.M1)GO TO 20
03460 KOUT=2
03470 I(1)=M1
03480 JOUT=1
03490 GO TO 23
03500 20 DO 21 J=2,5
03510 I(J)=I(J-1)+ISKIP
03520 IF(I(J).LT.M1)GO TO 21
03530 I(J)=M1
03540 KOUT=2
03550 JOUT=J
03560 GO TO 23
03570 21 CONTINUE
03580 23 PRINT 40,(Y(I(J)),J=1,JOUT)
03590 IF(ITER.GT.0)GO TO 25
03600 PRINT 30, (OMEGA(I(J)),J=1,JOUT)
03610  25 CONTINUE
03620 DO 60 NF=1,NFT
03630 GO TO(70,60) IPRIT(NF)
03640 70 PRINT 80, TITLE(NF),(F(I(J),NF),J=1,JOUT)
03650 60 CONTINUE
03660 PRINT 85
03670 85 FORMAT(/)
03680 I(1)=I(5)+ISKIP
03690 GO TO (12,90) KOUT
03700 30 FORMAT(1X,*  OMEGA(J) *,1P5E12.4)
03710 40 FORMAT(1X,*  Y(J)     *,1P5E12.4)
03720 80 FORMAT(1X,A11,1P5E12.4)
03730 90 RETURN
03740 ENTRY PRINT2
03750 PRINT100,ITER,X,U(1),DPDX,PCORR,P
03760 NOP=NOP+1
03770  XOC(NOP)=X
03780 VOC(NOP)=U(1)
03790 PO(NOP)=P
03800 100 FORMAT(1X,I6,1P5E12.4)
03810 RETURN
03820 END
03830C:::::::::::::::::::::::::::::::::::::::::::::::::::::::::::::::::
03840C  SUBROUTINE JOB GIVES GRID DETAILS,INITIAL VALUES OF THE
03850C DEPENDENT VARIABLES, BOUNDARY VALUES, OUTPUT FORMAT,ETC.
03860C:::::::::::::::::::::::::::::::::::::::::::::::::::::::::::::::::::::
03870C
03880 SUBROUTINE JOB
03890C
03900C      THIS IS THE COMMON BLOCK
03910C
03920 COMMON/COMA/OMEGA(200),TWOMD(200),CVWID(200),OMAV(200),COMAV(200)
03930+,M1,M2,M3,KIN,KEX,TITLE(6),IPRIT(6),X,RCVF(200),YCVF(200),AMUU
03940 COMMON/COMB/R(200),Y(200),RHO(200),PEI,IPLAX,CSALFA,F(200,6)
03950 COMMON/COMC/RADTYD(200),ALD2(200),RMI,RME,PCVWID(200),DELTAX,
03960+RCVWID(200),NF,NFT,YM1,PCORR,DPDX,ISKIP,P,V1(200),DELTAZ,US
03970 COMMON/COMD/ISOLVE(6),GAM(200),AJP(200),AJM(200),ACON(200),AP(200)
03980 COMMON/COME/INCRE1,INCRE2,XOUT,N,ITER,LSTOP,IPRT1,IPRT2,NITF
```

```
03990 COMMON/COMG/NL,XX(11),YY(11)
04000 DIMENSION U(200)
04010 EQUIVALENCE (U(1),F(1,1))
04020C
04030 ENTRY GRID
04040 OMEGA(1)=0.0
04050 DO 10 J=2,M1
04060 10 OMEGA(J)=(FLOAT(J-1)/FLOAT(M1-1))
04070 RETURN
04080 ENTRY START
04090 LSTOP=1
04100 ITER=0
04110 IPRT1=0
04120 IPRT2=0
04130 X=0.0
04140 NIT=0
04150 NITF=10
04160 DO 110 J=1,M1
04170 RHO(J)=.001185
04180 U(J)=2.*US*SQRT(1.-OMEGA(J))
04190 110 F(J,2)=0.0
04200 AMUU=188.E-6
04210 PEI=US*1.646E-4
04220 DXMULT=1.5
04230 DELTAX=DELTAZ
04240 RETURN
04250 ENTRY OUTPUT
04260 IF(IPRT2.GT.ITER)GOTO210
04270 CALL PRINT2
04280 IPRT2=IPRT2+INCRE2
04290 210 IF(IPRT1.GT.ITER)GOTO220
04300 CALL PRINT1
04310 IPRT1=IPRT1+INCRE1
04320 220 CONTINUE
04330 RETURN
04340 ENTRY XANDDX
04350 IF(ITER.EQ.0)GOTO300
04360 DXMAX=.010*Y(M1)
04370 DELTAX=DELTAX*DXMULT
04380 IF(DELTAX.GT.DXMAX)DELTAX=DXMAX
04390 300 X=X+DELTAX
04400 IF(X.GT.XX(NL))X=XX(NL)
04410 DO 301 J=1,NL
04420 301 IF(X.GE.XX(J))IL=J
04430 IF(IL.NE.NL)GOTO302
04440 YM1=YY(NL)
04450 GOTO 303
04460 302 YM1=YY(IL)+(X-XX(IL))*((YY(IL+1)-YY(IL))/(XX(IL+1)
04470+-XX(IL)))
04480 303 CONTINUE
04490 YM1=R(1)*YM1+YM1*YM1*CSALFA/2.
04500 RETURN
04510 ENTRY BOUND
04520 F(M1,1)=0.0
04530 F(1,2)=1.0
04540 RETURN
04550 END
READY.
```

B.3 Results of the Boundary Layer Calculation - P and U_g in the Test Nozzle

ΔP= 2.54 cm of H_2O

Position	Gas Velocity	Pressure
0	.360000E+02	.101500E+07
.129689E+00	.366778E+02	.101500E+07
.271349E+00	.391208E+02	.101500E+07
.401769E+00	.428023E+02	.101500E+07
.521841E+00	.477393E+02	.101500E+07
.632386E+00	.540093E+02	.101500E+07
.734159E+00	.617359E+02	.101500E+07
.827857E+00	.710887E+02	.101500E+07
.914121E+00	.822852E+02	.101500E+07
.993539E+00	.955955E+02	.101500E+07
.106666E+01	.111349E+03	.101499E+07
.113397E+01	.129940E+03	.101499E+07
.119595E+01	.151842E+03	.101499E+07
.125300E+01	.177614E+03	.101498E+07
.130553E+01	.207921E+03	.101498E+07
.135390E+01	.243545E+03	.101497E+07
.139842E+01	.285411E+03	.101495E+07
.143941E+01	.334609E+03	.101493E+07
.147715E+01	.392422E+03	.101491E+07
.151190E+01	.460363E+03	.101488E+07
.154388E+01	.540212E+03	.101483E+07
.157333E+01	.634066E+03	.101476E+07
.160037E+01	.754085E+03	.101466E+07
.162500E+01	.903132E+03	.101452E+07
.164743E+01	.108274E+04	.101431E+07
.166787E+01	.129424E+04	.101401E+07
.168661E+01	.152007E+04	.101364E+07
.170401E+01	.173813E+04	.101322E+07
.172062E+01	.185462E+04	.101297E+07
.173699E+01	.192420E+04	.101281E+07
.175318E+01	.198828E+04	.101266E+07
.176918E+01	.205008E+04	.101252E+07
.177000E+01	.205388E+04	.101251E+07

ΔP=7.62 cm of H_2O

Position	Gas Velocity	Pressure
0	.646000E+02	.101500E+07
.129689E+00	.655538E+02	.101500E+07
.271349E+00	.694261E+02	.101500E+07
.401769E+00	.754006E+02	.101500E+07
.521841E+00	.835395E+02	.101500E+07
.632386E+00	.939958E+02	.101500E+07
.734159E+00	.106997E+03	.101500E+07
.827857E+00	.122845E+03	.101499E+07
.914121E+00	.141925E+03	.101499E+07
.993539E+00	.164713E+03	.101499E+07
.106666E+01	.191786E+03	.101498E+07
.113397E+01	.223838E+03	.101497E+07
.119595E+01	.261700E+03	.101496E+07
.125300E+01	.306356E+03	.101495E+07
.130553E+01	.358974E+03	.101493E+07
.135390E+01	.420934E+03	.101490E+07
.139842E+01	.493867E+03	.101486E+07
.143941E+01	.579695E+03	.101480E+07
.147715E+01	.680686E+03	.101473E+07
.151190E+01	.799512E+03	.101462E+07
.154388E+01	.939324E+03	.101448E+07
.157333E+01	.110383E+04	.101428E+07
.160037E+01	.131532E+04	.101398E+07
.162500E+01	.157785E+04	.101353E+07
.164743E+01	.189428E+04	.101288E+07
.166787E+01	.226660E+04	.101197E+07
.168661E+01	.266286E+04	.101081E+07
.170401E+01	.304254E+04	.100953E+07
.172062E+01	.323468E+04	.100882E+07
.173699E+01	.334625E+04	.100838E+07
.175318E+01	.345003E+04	.100797E+07
.176918E+01	.355085E+04	.100755E+07
.177000E+01	.355692E+04	.100752E+07

ΔP=12.7 cm of H_2O

Position	Gas Velocity	Pressure
0	.844000E+02	.101500E+07
.129689E+00	.855160E+02	.101500E+07
.271349E+00	.903278E+02	.101500E+07
.401769E+00	.978334E+02	.101500E+07
.521841E+00	.108128E+03	.101500E+07
.632386E+00	.121416E+03	.101500E+07
.734159E+00	.137998E+03	.101499E+07
.827857E+00	.158266E+03	.101499E+07
.914121E+00	.182721E+03	.101498E+07
.993539E+00	.211978E+03	.101498E+07
.106666E+01	.246787E+03	.101497E+07
.113397E+01	.288048E+03	.101495E+07
.119595E+01	.336836E+03	.101494E+07
.125300E+01	.394429E+03	.101491E+07
.130553E+01	.462342E+03	.101488E+07
.135390E+01	.542365E+03	.101483E+07
.139842E+01	.636615E+03	.101476E+07
.143941E+01	.747589E+03	.101467E+07
.147715E+01	.878231E+03	.101455E+07
.151190E+01	.103202E+04	.101437E+07
.154388E+01	.121303E+04	.101413E+07
.157333E+01	.142611E+04	.101380E+07
.160037E+01	.170061E+04	.101329E+07
.162500E+01	.204127E+04	.101254E+07
.164743E+01	.245189E+04	.101145E+07
.166787E+01	.293487E+04	.100992E+07
.168661E+01	.344829E+04	.100798E+07
.170401E+01	.393864E+04	.100584E+07
.172062E+01	.418104E+04	.100467E+07
.173699E+01	.432033E+04	.100397E+07
.175318E+01	.445053E+04	.100329E+07
.176918E+01	.457744E+04	.100262E+07
.177000E+01	.458500E+04	.100258E+07

ΔP=25.4 cm of H_2O

Position	Gas Velocity	Pressure
0	.121400E+03	.101500E+07
.129689E+00	.122784E+03	.101500E+07
.271349E+00	.129289E+03	.101500E+07
.401769E+00	.139588E+03	.101500E+07
.521841E+00	.153837E+03	.101499E+07
.632386E+00	.172340E+03	.101499E+07
.734159E+00	.195526E+03	.101499E+07
.827857E+00	.223961E+03	.101498E+07
.914121E+00	.258357E+03	.101497E+07
.993539E+00	.299595E+03	.101496E+07
.106666E+01	.348739E+03	.101494E+07
.113397E+01	.407075E+03	.101491E+07
.119595E+01	.476133E+03	.101487E+07
.125300E+01	.557737E+03	.101482E+07
.130553E+01	.654047E+03	.101476E+07
.135390E+01	.767620E+03	.101466E+07
.139842E+01	.901475E+03	.101453E+07
.143941E+01	.105918E+04	.101435E+07
.147715E+01	.124494E+04	.101409E+07
.151190E+01	.146373E+04	.101374E+07
.154388E+01	.172138E+04	.101326E+07
.157333E+01	.202481E+04	.101259E+07
.160037E+01	.241668E+04	.101156E+07
.162500E+01	.290281E+04	.101003E+07
.164743E+01	.348882E+04	.100782E+07
.166787E+01	.417778E+04	.100470E+07
.168661E+01	.490909E+04	.100077E+07
.170401E+01	.560479E+04	.996446E+06
.172062E+01	.593833E+04	.994167E+06
.173699E+01	.612777E+04	.992814E+06
.175318E+01	.630609E+04	.991501E+06
.176918E+01	.648065E+04	.990179E+06
.177000E+01	.649089E+04	.990100E+06

ΔP=69.1cm of H_2O

Position	Gas Velocity	Pressure
0	.204000E+03	.101500E+07
.129689E+00	.205889E+03	.101500E+07
.271349E+00	.216015E+03	.101500E+07
.401769E+00	.232374E+03	.101499E+07
.521841E+00	.255263E+03	.101499E+07
.632386E+00	.285202E+03	.101498E+07
.734159E+00	.322913E+03	.101496E+07
.827857E+00	.369340E+03	.101494E+07
.914121E+00	.425671E+03	.101492E+07
.993539E+00	.493368E+03	.101488E+07
.106666E+01	.574203E+03	.101483E+07
.113397E+01	.670311E+03	.101476E+07
.119595E+01	.784240E+03	.101466E+07
.125300E+01	.919023E+03	.101452E+07
.130553E+01	.107825E+04	.101434E+07
.135390E+01	.126619E+04	.101408E+07
.139842E+01	.148787E+04	.101372E+07
.143941E+01	.174924E+04	.101322E+07
.147715E+01	.205731E+04	.101252E+07
.151190E+01	.242036E+04	.101156E+07
.154388E+01	.284816E+04	.101023E+07
.157333E+01	.335222E+04	.100838E+07
.160037E+01	.400519E+04	.100555E+07
.162500E+01	.481471E+04	.100133E+07
.164743E+01	.579067E+04	.995214E+06
.166787E+01	.693741E+04	.986592E+06
.168661E+01	.815252E+04	.975757E+06
.170401E+01	.930287E+04	.963886E+06
.172062E+01	.983231E+04	.957890E+06
.173699E+01	.101290E+05	.954383E+06
.175318E+01	.104116E+05	.950946E+06
.176918E+01	.106897E+05	.947470E+06
.177000E+01	.107057E+05	.947267E+06

ΔP=276cm of H_2O

Position	Gas Velocity	Pressure
0	.415400E+03	.101500E+07
.129689E+00	.418343E+03	.101500E+07
.271349E+00	.437288E+03	.101499E+07
.401769E+00	.468682E+03	.101497E+07
.521841E+00	.513173E+03	.101494E+07
.632386E+00	.571828E+03	.101491E+07
.734159E+00	.646116E+03	.101485E+07
.827857E+00	.737944E+03	.101478E+07
.914121E+00	.849707E+03	.101467E+07
.993539E+00	.984348E+03	.101453E+07
.106666E+01	.114544E+04	.101432E+07
.113397E+01	.133729E+04	.101404E+07
.119595E+01	.156502E+04	.101365E+07
.125300E+01	.183476E+04	.101311E+07
.130553E+01	.215375E+04	.101236E+07
.135390E+01	.253060E+04	.101131E+07
.139842E+01	.297546E+04	.100987E+07
.143941E+01	.350035E+04	.100786E+07
.147715E+01	.411944E+04	.100507E+07
.151190E+01	.484947E+04	.100120E+07
.154388E+01	.571021E+04	.995832E+06
.157333E+01	.672494E+04	.988376E+06
.160037E+01	.804377E+04	.976870E+06
.162500E+01	.967734E+04	.959771E+06
.164743E+01	.116471E+05	.934961E+06
.166787E+01	.139600E+05	.899974E+06
.168661E+01	.164063E+05	.856079E+06
.170401E+01	.187103E+05	.808246E+06
.172062E+01	.197199E+05	.785283E+06
.173699E+01	.202759E+05	.772113E+06
.175318E+01	.208160E+05	.758968E+06
.176918E+01	.213520E+05	.745583E+06
.177000E+01	.213818E+05	.744828E+06

B.4 Results of the Boundary Layer Calculation – P and U_g in Conical Nozzles

	Position	Gas Velocity	Pressure
α=30° ΔP=2.68 cm of H_2O	0	.330600E+02	.101500E+07
	.130045E+00	.352771E+02	.101500E+07
	.261209E+00	.426909E+02	.101500E+07
	.371456E+00	.553777E+02	.101500E+07
	.464122E+00	.746294E+02	.101500E+07
	.542011E+00	.102574E+03	.101499E+07
	.607479E+00	.142402E+03	.101499E+07
	.662506E+00	.198738E+03	.101498E+07
	.708759E+00	.278170E+03	.101495E+07
	.747635E+00	.390038E+03	.101491E+07
	.780312E+00	.547546E+03	.101482E+07
	.807778E+00	.769337E+03	.101465E+07
	.830864E+00	.108174E+04	.101431E+07
	.850269E+00	.152191E+04	.101364E+07
	.866000E+00	.211499E+04	.101237E+07
α=30° ΔP=23.4 cm of H_2O	0	.100000E+03	.101500E+07
	.130045E+00	.105327E+03	.101500E+07
	.261209E+00	.125247E+03	.101500E+07
	.371456E+00	.160572E+03	.101499E+07
	.464122E+00	.215196E+03	.101498E+07
	.542011E+00	.295408E+03	.101495E+07
	.607479E+00	.410621E+03	.101491E+07
	.662506E+00	.574485E+03	.101481E+07
	.708759E+00	.806510E+03	.101462E+07
	.747635E+00	.113441E+04	.101425E+07
	.780312E+00	.159742E+04	.101350E+07
	.807778E+00	.225107E+04	.101202E+07
	.830864E+00	.317386E+04	.100907E+07
	.850269E+00	.447676E+04	.100320E+07
	.866000E+00	.623429E+04	.992109E+06
α=30° ΔP=204 cm of H_2O	0	.300000E+03	.101500E+07
	.130045E+00	.313574E+03	.101499E+07
	.261209E+00	.369191E+03	.101497E+07
	.371456E+00	.470195E+03	.101492E+07
	.464122E+00	.628173E+03	.101482E+07
	.542011E+00	.861732E+03	.101461E+07
	.607479E+00	.119872E+04	.101421E+07
	.662506E+00	.167954E+04	.101339E+07
	.708759E+00	.236203E+04	.101176E+07
	.747635E+00	.332846E+04	.100852E+07
	.780312E+00	.469545E+04	.100206E+07
	.807778E+00	.662816E+04	.989171E+06
	.830864E+00	.936030E+04	.963438E+06
	.850269E+00	.132225E+05	.912058E+06
	.866000E+00	.184361E+05	.814823E+06

	Position	Gas Velocity	Pressure
	0	.330600E+02	.101500E+07
	.786560E-01	.352187E+02	.101500E+07
	.164485E+00	.439316E+02	.101500E+07
	.234684E+00	.598660E+02	.101500E+07
	.292101E+00	.853543E+02	.101500E+07
	.339063E+00	.124318E+03	.101499E+07
α=45°	.377473E+00	.182875E+03	.101498E+07
ΔP=2.60 cm of H_2O	.408889E+00	.270304E+03	.101496E+07
	.434584E+00	.400532E+03	.101491E+07
	.455601E+00	.594369E+03	.101479E+07
	.472790E+00	.882876E+03	.101454E+07
	.486849E+00	.131239E+04	.101399E+07
	.498349E+00	.195202E+04	.101277E+07
	.500000E+00	.208611E+04	.101245E+07
	0	.100000E+03	.101500E+07
	.786560E-01	.105393E+03	.101500E+07
	.164485E+00	.129524E+03	.101500E+07
	.234684E+00	.174977E+03	.101499E+07
	.292101E+00	.248725E+03	.101497E+07
	.339063E+00	.362407E+03	.101493E+07
α=45°	.377473E+00	.534189E+03	.101484E+07
ΔP=22.8 cm of H_2O	.408889E+00	.791678E+03	.101464E+07
	.434584E+00	.117638E+04	.101419E+07
	.455601E+00	.175045E+04	.101321E+07
	.472790E+00	.260677E+04	.101102E+07
	.486849E+00	.388408E+04	.100616E+07
	.498349E+00	.578956E+04	.995344E+06
	.500000E+00	.618185E+04	.992587E+06
	0	.300000E+03	.101500E+07
	.786560E-01	.314246E+03	.101499E+07
	.164485E+00	.382956E+03	.101497E+07
	.234684E+00	.514814E+03	.101490E+07
	.292101E+00	.730558E+03	.101474E+07
	.339063E+00	.106474E+04	.101439E+07
α=45°	.377473E+00	.157131E+04	.101360E+07
ΔP=201. cm of H_2O	.408889E+00	.233235E+04	.101186E+07
	.434584E+00	.347143E+04	.100798E+07
	.455601E+00	.517371E+04	.999349E+06
	.472790E+00	.771620E+04	.980126E+06
	.486849E+00	.115129E+05	.937301E+06
	.498349E+00	.171827E+05	.841868E+06
	.500000E+00	.183395E+05	.817750E+06

APPENDIX C

PROGRAM PARVEL FOR CALCULATION OF PARTICLE VELOCITIES

C.1 Glossary of User Modified Terms

All dimensioned variables were expressed in cgs units.

Term	Statement Number	Significance
VIS	135	Fluid viscosity
D	135	Fluid density
EPS, ETA	135	Error criteria for subroutine RK
DIS	136	Distance from nozzle exit to measurement point
DP	150	Particle diameter
RHO	150	Particle density
NPRINT	150	Index controlling printing 0 implies print particle velocity for each step; 1 implies print only last 5 steps
M	180	Number of positions for which gas velocity and pressure are given in file called in 140
X(I), V(I), P(I)	240	Position, gas velocity and pressure; read from file called in 140

C.2 Listing of Program PARVEL

```
00100 PROGRAM PARVEL(INPUT,OUTPUT,TAPE1)
00110 DIMENSION TEMP(4),VP(200),P(200)
00120 COMMON/A/ J,VIS,V(200),C(200),D,DP,PM,RE(200),X(200),M
00130 EXTERNAL DERIV
00135 DATA VIS,D,EPS,ETA/188.E-6,.001185,1.E-5,1.E-5/
00136 DATA DIS/145.E-4/
00140 CALL GETPF(5HTAPE1,4HF701,0,0)
00150 READ, DP,RHO,NPRINT
00160 PM=.524*RHO*DP**3
00170 REWIND 1
00180 READ(1,12)M
00190 12 FORMAT(I4)
00200 3 FORMAT(3HDP=,E10.3,5X,4HRHO=,E10.3,5X,2HM=,I4,5X,6HVEXIT=,E10.3)
00210 2 FORMAT(10H*POSITION*,2X,10H*PART VEL*,1X,12H*DVP/DX(I-1),1X,
00220+10H*STEP SIZ*,2X,10H*RE(DP)   *,2X,10H*SLIP COR*)
00230 DO 20 I=1,M
00240 READ(1,13)X(I),V(I),P(I)
00250 13FORMAT(3(E13.6))
00260 20 C(I)=1.+16.5/(DP*P(I))+5.5*EXP(-.065*DP*P(I))/(DP*P(I))
00270 PRINT3,DP,RHO,M,V(M)
00280 PRINT 2
00282 X(M+1)=X(M)+DIS
00284 V(M+1)=V(M)
00286 C(M+1)=C(M)
00288 P(M+1)=P(M)
00290 DO 200 J=1,M
00300 XI=X(J)
00310 XF=X(J+1)
00360 Y=V(1)
00370 IF(J.EQ.1) GO TO 22
00380 Y=VP(J)
```

```
00390 22 CONTINUE
00400 N=1
00410 ID=1
00420  IF(J.GT.1)ID=-1
00430 CALL RK(XI,XF,Y,F,DERIV,N,EPS,ETA,ID,TEMP,DX)
00440 VP(J+1)=Y
00450 RE(J+1)=(V(J+1)-VP(J+1))*DP*D/VIS
00460 IF(NPRINT.EQ.0)GO TO 18
00470 IF(J.LT.M-5)GO TO 200
00480 18CONTINUE
00490 PRINT 1, XF,Y,F,DX,RE(J+1),C(J+1)
00500 1 FORMAT(E14.7,5(E11.4,1X))
00510 200 CONTINUE
00520 STOP
00530 END
00540 SUBROUTINE DERIV(XI,Y,F)
00550 DIMENSION FXV(3),XA(3)
00560 COMMON/A/ J,VIS,V(200),C(200),D,DP,PM,RE(200),X(200),M
00565 IF(J.GE.M)GO TO 1000
00570 DO 180 K=1,3
00580 L=J-2+K
00590 IF(J.EQ.1)L=J-1+K
00610 FXV(K)=V(L)
00640 180 XA(K)=X(L)
00650 Z=XI
00670 YV=AITKENF(Z,FXV,XA,2)
00672 1000 YVIS=VIS
00674 IF(J.GE.M) YV=V(M)
00680 YC=C(J)
00690 YD=D
00700 F=9.42*YVIS*DP*(YV-Y)/(PM*Y*YC)
00710 IF(J.EQ.1)GO TO 10
00720 IF (RE(J).LT..5)GO TO 10
```

```
00730 F=F+1.57*(DP**1.67)*(YD**.667)*(YVIS**.333)*((YV-Y)**1.67)
00740+/(YC*FM*Y)
00750 10 CONTINUE
00760 RETURN
00770 END
READY.
```

APPENDIX D

PROGRAM CONOPT FOR CALCULATION OF PARTICLE VELOCITIES IN IDEAL NOZZLES

D.1 Glossary of User Modified Terms

Term	Statement Number	Significance
EPS, ETA	140	Error parameters for subroutine RK
TANA	150	Tangent of the half-angle of the cone
REDP(J)	160	Values of Re [see Equation (4.6)] for which dimensionless particle velocity is to be solved
ST(J)	170	Values of St [see Equation (4.5)] for which dimensionless particle velocity is to be solved
NR; NS	180	Number of values of Re and St, respectively

D.2 Listing of Program CONOPT

```
PROGRAM CONOPT(INPUT,OUTPUT)
DIMENSION TEMP(4),X(35),DPV(20,20,4),PRE(20,20,4)
COMMON /A/ST(20),REDP(20),TANA,OL,K,L
EXTERNAL DERIV
DATA EPS,ETA/1.E-5,1.E-5/
DATA TANA/.268/
DATA(REDP(J),J=1,3)/10.,30.,100./
DATA(ST(J),J=1,6)/5.,12.,20.,50.,120.,200./
DATA NR,NS/3,6/
OL=10./TANA
X(1)=0.
X(2)=OL
X(3)=OL+.2
X(4)=OL+.4
X(5)=OL+.6
PRINT 5,TANA
5 FORMAT(*TANGENT ALFA=*,F8.5)
DO 200 K=1,NR
DO 200 L=1,NS
RE=0.
DO 200 J=1,4
XI=X(J)
XF=X(J+1)
N=1
ID=1
IF(J.GT.1)ID=-1
Y=.00826
IF(J.NE.1)Y=VP
CALL RK(XI,XF,Y,F,DERIV,N,EPS,ETA,ID,TEMP,DX)
VP=Y
XX=X(J+1)
IF(X(J+1).GE.OL)XX=OL
PRE(K,L,J)=REDP(K)*(1./((11.-XX*TANA)**2)-VP)
```

```
00450 DPV(K,L,J)=Y
00460 2 FORMAT(3X,I2,2X,E9.3,5X,E9.3,5X,F8.5)
00470 200CONTINUE
00480 DO800 J=1,4
00490 JJ=J-1
00500 PRINT 31,JJ
00510 31 FORMAT(//,*DIMENSIONLESS PARTICLE VELOCITY AND PARTICLE RE(PRE)
00520+AT  ,*,I1,*DAIMETER FROM EXIT*)
00530 PRINT33
00540 33FORMAT (23X,*---REDP---*)
00550 PRINT 32,(REDP(L),L=1,NR)
00560 PRINT 39
00570 39 FORMAT(13X,*========================================================
00580+==========*)
00590 32 FORMAT(4X,3HST,4X,1H*,6(E9.3,2X),)
00600 DO 800 L=1,NS
00610  PRINT 34, ST(L),(DPV(K,L,J),K=1,NR)
00620 800 PRINT 38,(PRE(K,L,J),K=1,NR)
00630 34 FORMAT(/,1X,E9.3,1X,1H*,6(F8.5,3X))
00640 38 FORMAT(4X,5H(PRE),2X,6(1H(,E9.3,1H)))
00650 STOP
00660 END
00670 SUBROUTINE DERIV(XI,Y,F)
00680 COMMON /A/ST(20),REDP(20),TANA,OL,K,L
00690 XX=XI
00700 IF(XI.GE.OL)XX=OL
00710 VG=1./((11.-XX*TANA)**2)
00720 F=(VG-Y)/(ST(L)*Y)
00730 IF(REDP(K)*(VG-Y).LT..5)GO TO 10
00740 F=F+(REDP(K)**.6667)*((VG-Y)**1.6667)/(6.*ST(L)*Y)
00750 10CONTINUE
00760 RETURN
00770 END
```

APPENDIX E

MEASURED VELOCITY DISTRIBUTIONS FOR REPRESENTATIVE TRIALS

Trial 53A
n=2

Channel 60

```
000064 000000 000000 000000 000000 000000 000000 000000 000000 000000
000000 000000 000000 000000 000000 000000 000000 000000 000000 000000
000000 000000 000000 000000 000000 000000 000000 000000 000000 000000
000000 000000 000000 000000 000000 000000 000000 000000 000000 000000
000000 000000 000000 000000 000000 000000 000000 000000 000000 000000
000000 000000 000000 000000 [000001 000003 000005 000060 000131 000384
000418 000459 000246 000050 000044 000013 000024 000017 000006 000009
000028 000011 000007 000005 000005 000002 000002 000002 000002 000003
000034 000001 000001] 000001 000000 000000 000000 000000 000000 000000
```

Trial 52H
n=4

Channel 120

```
000054 000000 000000 000000 000000 000000 000000 000000 000000 000000
000000 000000 000000 000000 000000 000000 000000 000000 000000 000000
000000 000000 000000 000000 000000 000000 000000 000000 000000 000000
000000 000000 000000 000000 000000 000000 000000 000000 000000 000000
000000 000000 000000 000000 000000 000000 000000 000000 000000 000000
000000 000000 000000 000000 000000 000000 000000 000000 000000 000000
000000 000000 000000 000000 000000 000000 000000 000000 000000 000000
000000 000000 000000 000000 000000 000000 000000 000000 000000 000000
000000 000000 000000 000000 000000 000000 000000 000000 000000 000000
000000 000000 000000 000000 000000 000000 000000 000000 000000 000000
000000 000000 000000 000000 000000 000000 000000 000000 000000 000000
000000 000000 000000 000000 000000 000000 000000 000000 000000 000023
[001407 015486 013458 003102 000230 000033] 000018 000021 000012 000009
000024 [000171 001212 003699 003763 000387 000044 000015] 000014 000107
000348 000298 000046 000008 000004 000004 000017 000081 000051 000017
000002 000006 000010 000004 000002 000001 000002 000001 000001 000002
000000 000001 000000 000000 000000 000000 000000 00000
```

```
               000185 000000 000000 000000 000000 000000 000000 000000 000000 000000
               000000 000000 000000 000000 000000 000000 000000 000000 000000 000000
               000000 000000 000000 000000 000000 000000 000000 000000 000000 000000
               000000 000000 000000 000000 000000 000000 000000 000000 000000 000000
               000000 000000 000000 000000 000000 000000 000000 000000 000000 000000
               000000 000000 000000 000000 000000 000000 000000 000000 000000 000000
               000000 000000 000000 000000 000000 000000 000000 000000 000000 000000
Trial 64E      000000 000000 000000 000000 000000 000000 000000 000000 000000 000000
n=6            000004 000005 000004 000006 000005 000006 000005 000004 000001 000001
               000002 000001 000002 000000 000000 000001 000000 000000 000000 000000
               000000 000000 000000 000000 000000 000000 000000 000000 000000 000000
               000000 000000 000000 000000 000000 000000 000000 000000 000000 000000
               000000 000000 000000 000000 000000 000000 000009[000717 008178 007194
    Channel 130000268 000016]000005[000018 000888 001639 001104 000974 000351]000003
               000099 000512 000186 000015 000020 000077 000051 000030 000019 000002
               000003 000018 000007 000000 000000 000001 000001 000001 000001 000000
               000000 000000 000000 000000 000000 000000 000000 000000 000000 000000
               000000 000000 000000 000000 000000 000000 000000 000000 000000 000000
               000000 000000 000000 000000 000000 0P
```

128CHANNELS SUPPRESSED

```
                     000000 000000 000000 000000 000000 000000 000000 000000 000000 000000
                     000000 000000 000000 000000 000000 000000 000000 000000 000000 000000
                     000000 000000 000000 000000 000000 000000 000000 000000 000000 000000
                     000000 000000 000000 000000 000000 000000 000000 000000 000000 000000
Trial 62S            000000 000000 000000 000000 000000 000000 000000 000001 000000 000001
n=6                  000000 000001 000010 000109 000279 001857 001472 000200 000005 000003
        Channel 188  000000 000000 000000 000000 000000 000000 000000 000000 000000 000000
                     000000 000007 000000 000013 000042 000076 000164 000121 000220 000011
                     000005 000000 000000 000000 000000 000000 000002 000008 000005 000022
                     000024 000018 000006 000000 000001 000000 000000 000000 000001 000002
                     000002 000001 000002 000000 000000 000000 000000 000001 000000 000000
                     000000 000000 000001 000000 000000 000000 000000 000000 000000 000000
                     000000 000000 000000 000000 000000 000000 000000 000000
```

```
                     000071 000000 000000 000000 000000 000000 000000 000000 000000 000000
                     000000 000000 000000 000000 000000 000000 000000 000000 000000 000000
                     000000 000000 000000 000000 000000 000000 000000 000000 000000 000000
                     000000 000000 000000 000000 000000 000000 000000 000000 000000 000000
                     000000 000000 000000 000000 000000 000000 000000 000000 000000 000000
Trial 49J            000000 000000 000000 000000 000000 000000 000000 000000 000000 000000
n=5                  000000 000000 000000 000000 000000 000000 000000 000000 000000 000000
                     000000 000000 000000 000000 000000 000000 000000 000001 000000 000000
                     000000 000000 000000 000000 000000 000000 000000 000000 000000 000000
         Channel 90  000000 000000 000000 000002 000060 000084 000578 006601 029252 081816
                     004941 000221 000032 000029 000029 000039 000025 000039 000083 000448
                     000799 001448 000564 000025 000000 000000 000000 000000 000001 000001
                     000000 000000 000000 000000 000000 000000 000000 000000 000000 000000
                     000000 000000 000000 000000 000000 000000 000000 000000 000000 000000
                     000000 000000 000000 000000 000000 000000 000000 000000 000000 000000M
```

```
                           000069 000000 000000 000000 000000 000000 000000 000000 000000 000000
                           000000 000000 000000 000000 000000 000000 000000 000000 000000 000000
Trial 52C                  000000 000000 000000 000000 000000 000000 000000 000000 000000 000000
n=4                        000000 000000 000000 000000 000000 000000 000000 000000 000000 000000
                           000000 000000 000000 000000 000000 000002 000000 000000 000001 000019
             Channel 50    002054 017845 039224 012603 000687 001356 002848 003357 001412 000466
                           000589 000572 000511 000131 000069 000020 000006 000008 000001 000000
                           000000 000001 000001 000000 000000 000000 000000 000000 000000 000000
                           000000 000000 000000 000000 000001 000001 000000 000000 000000 000000
                           000000 000000 000000 000000 000000 000000 000000 000000 000000 000000
                           000000 000000
```

```
                           000040 000000 000000 000000 000000 000000 000000 000000 000000 000000
                           000000 000000 000000 000000 000000 000000 000000 000000 000000 000000
                           000000 000000 000000 000000 000000 000000 000000 000000 000000 000000
                           000000 000000 000000 000000 000000 000000 000000 000000 000000 000000
Trial 49A                  000000 000000 000000 000000 000000 000000 000000 000000 000000 000000
n=4                        000000 000000 000000 000000 000000 000000 000000 000000 000000 000000
                           000000 000000 000000 000000 000000 000000 000000 000000 000000 000000
                           000000 000000 000000 000000 000000 000006 000102 000569 000962 002133
             Channel 80    003920 002960 000969 000199 000159 000119 000222 000145 000018 000022
                           000013 000005 000000 000002 000000 000000 000000 000002 000000 000000
                           000000 000000 000000 000000 000000 000000 000000 000000 000000 000000
                           000000 000000 000000 000000 000000 000000 000000 000000 000000 000000
                           000000 000000 000000 000000 000000 000000 000000 000000 000000 000000
                           000000 000001 000000 0000
```

```
                 000251 000000 000000 000000 000000 000000 000000 000000 000000 000000
                 000000 000000 000000 000000 000000 000000 000000 000000 000000 000000
                 000000 000000 000000 000000 000000 000000 000000 000000 000000 000000
                 0 00000 000000 000000 000000 000000 000000 000000 000000 000000 000000
                 0 00000 000000 000000 000000 000000 000000 000000 000000 000000 000000
                 0 00000 000000 000000 000000 000000 000000 000000 000000 000000 000000
Trial 66AD       000000 000000 000000 000000 000000 000000 000000 000000 000000 000000
n=4              0 00000 000000 000000 000000 000000 000000 000000 000000 000000 000000
                 0 00000 000000 000000 000000 000000 000000 000000 000000 000000 000000
                 000000 000000 000000 000000 000000 000000 000000 000000 000000 000000
                 000000 000000 000000 000000 000000 000000 000000 000000 000000 000000
                 000000 000000 000000 000000 000000 000000 000000 000000 000000 000000
                 000000 000000 000000 000000 000000 000000 000000 000000 000000 000000
                 000000 000000 000000 000000 000000 000000 000000 000000 000000 000000
                 000000 000000 000000 000000 000000 000000 000000 000000 000000 000000
                 000000 000000 000000 000000 000000 000000 000000 000000 000000 000000
                 0 00000 000000 000000 000000 000000 000000 000000 000000 000000 000000
                 0 00000 000000 000000 000000 000000 000000 000000 000000 000000 000000
                 0 00000 000000 000000 000000 000000 000000 000000 000000 000000 000000
                 000000 000000 000000 000000 000000 000000 000000 000000 000000 000000
                 0 00002 000000 000000 000000 000000 000000 000000 000002 000000 000005
Channel 210     |0 00031 000138 000603 001309 001894 001487 000560 000195 000081 000039]
                 0 00014 000005 000006 000001 000000 000000 000000 000000 000000 000000
                 000000 000000 000000 000000 000000 000002 000000 000000 000000 000000
                 000000 000000 000000 000000 000000 000000 00
```

Trial 53D
n=2

Channel 170

```
000059 000000 000000 000000 000000 000000 000000 000000 000000 000000
000000 000000 000000 000000 000000 000000 000000 000000 000000 000000
000000 000000 000000 000000 000000 000000 000000 000000 000000 000000
000000 000000 000000 000000 000000 000000 000000 000000 000000 000000
000000 000000 000000 000000 000000 000000 000000 000200 000000 000000
000000 000000 000000 000000 000000 000000 000000 000000 000000 000000
000000 000000 000000 000000 000000 000000 000000 000000 000000 000000
000000 000000 000000 000000 000000 000000 000000 000000 000000 000000
000000 000000 000000 000000 000000 000000 000000 000000 000000 000000
000000 000000 000000 000000 000000 000000 000000 000000 000000 000000
000000 000000 000000 000000 000002 000000 000000 000000 000000 000000
000000 000000 000000 000000 000003 000000 000000 000000 000000 000000
000000 000000 000000 000000 000000 000001 000002 000002 000000 000001
000001 000001 000000 000002 000000 000000 000005 000006 000000 000005
000004 000002 000002 000033 000002 000005 000001 000002 000003 000001
000001 000003 000000 000001 000002 000002 000002 000005 000004 000004
000009 000027 000049 000160 000406 000624 000987 001630 002052 002012
001921 001147 000935 000668 000348 000227 000186 000170 000097 000083
000075 000042 000036 000017 000018 000022 000006 000011 000001 000001
000003 000003 000002 000002 000001 000002 000002 000002 000003 000001
000001 000000 000000 000000 000000 000001 000001 000000 000002 000000
000000 000001 000000 000002 000001 000001 000001
```